

Modeling, Robust Control, and Experimental Validation of a
Supercavitating Vehicle

A THESIS
SUBMITTED TO THE FACULTY OF THE GRADUATE SCHOOL
OF THE UNIVERSITY OF MINNESOTA
BY

David Escobar Sanabria

IN PARTIAL FULFILLMENT OF THE REQUIREMENTS
FOR THE DEGREE OF
DOCTOR OF PHILOSOPHY

Roger E.A. Arndt and Gary J. Balas, advisers
Peter J. Seiler, co-adviser

June 2015

© David Escobar Sanabria 2015

Acknowledgments

I would like to thank all the people that made my Ph.D. an enriching experience. I am thankful with my advisers from the National University of Colombia, Ernesto Cordoba and Jaime Ivan Ordonez. Ernesto gave me the opportunity of working in his laboratory and encouraged me to pursue a graduate degree. Jaime Ivan has been an example of excellence and opened possibilities for me to pursue my graduated studies in the United States.

Through Jaime Ivan, I met my advisor and mentor for graduate school, Gary Balas. During his visit to Colombia, I asked Gary if he could help me find support for my graduate education. A few months later, I joined his group at the University of Minnesota. Gary's opportunity changed my life and I will be always grateful to him. Sadly, Gary is not with us today. His approach to address difficulties in life, leadership, and professional legacy will be always with me.

Alongside Gary, I started working at the St. Anthony Falls Laboratory (SAFL). There, I met my advisor Roger Arndt. I am thankful that he has been a source of motivation for my research and a support for all my initiatives. I would like to thank Peter Seiler for his outstanding teaching, inspiring ideas, and wise academic and professional advice. I am thankful with Demoz Gebre for his role in my graduate education and academic support. I am grateful with William Garrard and Jiarong Hong for being part of my Ph.D. committee.

I want to thank Devin Vollmer for the extra hours building our experimental infrastructure and his excellent work that has been key to complete this dissertation. I am grateful to my colleagues from the controls and SAFL laboratories for the discussions, collaboration, and friendship: Rohit, Abhijit, Hamid, Arnar, Austin, Ellison, Seung Jae Lee, Arda, Claudia, Andrei, Paul, Will, Janos, Raghu, Harald, Tamas, Julian, Bela, and Jennifer.

I have immense gratitude for all who have been part of my life during these years: Christian, Luis, Sandy, Madhan, Tomas, Ardalan, Elizabeth, Jake, Andres, Carlos, Juan Jose, Helmer, Varinia, Carola, Claudia, and many others not mentioned here. I greatly thank Brooke for her love, for supporting me during the long hours of work, and for dreaming with me.

Finally, I want to acknowledge the financial support for this research by the U.S. Office of Naval Research.

This work is dedicated to the memory of my advisor and friend, Gary J. Balas

and

to my family, Myriam, Humberto, Francisco, and Lucia.

Abstract

This dissertation considers the mathematical modeling, control under uncertainty, and experimental validation of an underwater supercavitating vehicle. By traveling inside a gas cavity, a supercavitating vehicle reduces hydrodynamic drag, increases speed, and minimizes power consumption. The attainable speed and power efficiency make these vehicles attractive for undersea exploration, high-speed transportation, and defense. However, the benefits of traveling inside a cavity come with difficulties in controlling the vehicle dynamics. The main challenge is the nonlinear force that arises when the back-end of the vehicle pierces the cavity. This force, referred to as planing, leads to oscillatory motion and instability. Control technologies that are robust to planing and suited for practical implementation need to be developed. To enable these technologies, a low-order vehicle model that accounts for inaccuracy in the characterization of planing is required. Additionally, an experimental method to evaluate possible pitfalls in the models and controllers is necessary before undersea testing.

The major contribution of this dissertation is a unified framework for mathematical modeling, robust control synthesis, and experimental validation of a supercavitating vehicle. First, we introduce affordable experimental methods for mathematical modeling and controller testing under planing and realistic flow conditions. Then, using experimental observations and physical principles, we create a low-order nonlinear model of the longitudinal vehicle motion. This model quantifies the planing uncertainty and is suitable for robust controller synthesis. Next, based on the vehicle model, we develop automated tools for synthesizing controllers that deliver a certificate of performance in the face of nonlinear and uncertain planing forces. We demonstrate theoretically and experimentally that the proposed controllers ensure higher performance when the uncertain planing dynamics are considered. Finally, we discuss future directions in supercavitating vehicle control.

Contents

List of Figures	ix
Nomenclature	xii
Chapter 1 Introduction	1
1.1 Vehicle	1
1.2 Challenges and Contributions	2
1.2.1 Vehicle Modeling	2
1.2.2 Robust Control	3
1.2.3 Experimental Validation	4
Chapter 2 Preliminaries	5
2.1 Vector Notation and Transformations	5
2.1.1 Position Vectors	5
2.1.2 Velocity Vectors	7
2.2 Supercavitation	8
2.2.1 Mechanisms	8
2.2.2 Blockage	8

2.2.3	Gravity	9
2.3	General Equations of Motion	10
2.4	Stability	11
2.5	Performance	13
Chapter 3	Experimental Methods	14
3.1	Related Work	14
3.2	High-Speed Water Tunnel	15
3.3	Scale Test Vehicle	15
3.4	Oscillating Foil	16
3.5	Modeling Methods	16
3.5.1	Cavitator and Fin Forces	17
3.5.2	Planing Forces	17
3.5.3	Supercavity	18
3.6	Control Validation Methods	19
Chapter 4	Vehicle Modeling	24
4.1	Related Work	24
4.2	Problem Formulation	25
4.3	Coordinate Frames and Angles	26
4.4	Forces	27
4.4.1	Thrust	27
4.4.2	Gravitational	27
4.4.3	Cavitator	28

4.4.4	Fins	28
4.4.5	Planing	31
4.5	Supercavity	34
4.5.1	1-DOF Test Vehicle	34
4.5.2	3-DOF Undersea Vehicle	35
4.5.3	Effect of Cavitator Attack Angle	36
4.5.4	Time Dependent Model	38
4.5.5	Experimental Validation	40
4.5.6	Vehicle Immersion	42
4.6	Vehicle Dynamics	42
4.6.1	Unconstrained 3-DOF Vehicle	43
4.6.2	Experimental 1-DOF Vehicle	44
4.7	Flow Disturbances	46
4.8	Simplified Dynamic Model	46
4.8.1	Unconstrained 3-DOF Vehicle	46
4.8.2	Experimental 1-DOF Vehicle	50
4.8.3	Supercavity Delay	52
4.9	Uncertainty	53
4.9.1	3-DOF Uncertain Dynamics	56
4.9.2	1-DOF Uncertain Dynamics	57
4.10	Actuator Dynamics	58
4.11	Model Identification 1-DOF	59
4.11.1	Experiments	61

4.11.2 Results	62
Chapter 5 Control Synthesis and Validation	65
5.1 Related Work	65
5.2 Problem Formulation	66
5.2.1 Synthesis	66
5.2.2 Experimental Validation	67
5.3 Model	67
5.4 Stability	70
5.5 Performance	71
5.6 Control Synthesis	72
5.6.1 Conditions for the Existence of a Controller	73
5.6.2 Controller Reconstruction	76
5.7 Local Control Synthesis	77
5.8 Remarks on the Synthesis Tools	78
5.9 Control Design for 1-DOF Test Vehicle	79
5.9.1 H_∞ Controller	81
5.9.2 Sector Constrained-SC-Controller	81
5.10 Experimental Validation	84
Chapter 6 Conclusions and Future Directions	89
6.1 Concluding Remarks	89
6.2 Research Directions	90
Bibliography	92

Appendix A	Mathematical Tools	96
A.1	Linear Matrix Inequalities	96
A.2	Semidefinite Programming	97
A.3	Matrix Variables	97
A.4	Schur Complement	98
A.5	S-Procedure	98
Appendix B	Image Segmentation	100
B.1	Definitions	100
B.2	Method	100
B.3	Planing Computation	102

List of Figures

1.1	Experimental scale vehicle at the St. Falls Laboratory, University of Minnesota	2
2.1	Schematic of coordinate frames on the plane	6
3.1	Scale test vehicle	15
3.2	Picture of fins used in experiments	16
3.3	Architecture of experimental platform for modeling	17
3.4	Image of the vehicle with parameters to describe the planing forces . . .	18
3.5	Architecture of experimental platform for control assessment	20
3.6	Rotatable scale vehicle during control experiment	21
3.7	Photograph of the test vehicle from the bottom view. Lateral planing induced by the rotary shaft	22
3.8	Photograph of the test vehicle from the bottom view. Lateral planing induced by the fin	22
3.9	Oscillations due to planing during experiment	23
4.1	Illustration of frames and angles used for vehicle modeling	26
4.2	Photograph of the fins with different cavitator sizes from the bottom view of the tunnel	29

4.3	Fin drag coefficient and data	30
4.4	Fin lift coefficient and data	30
4.5	Image of vehicle back-end with parameters used to describe the planing forces	31
4.6	Coefficient of planing force along the body's axial axis	33
4.7	Coefficient of planing force along the body's normal axis	33
4.8	Supercavity and parameters for semi-elliptical models	35
4.9	Parameters of supercavity not subject to blockage	36
4.10	Function to describe the supercavity displacement as a result of a nonzero cavitator attack angle	37
4.11	Schematic of supercavity dynamic model	39
4.12	Comparison of supercavity dynamic model with photographs	41
4.13	Actual and idealized planing immersion	42
4.14	Schematic of full nonlinear dynamics	45
4.15	Schematics of vehicle dynamics described with a dead-zone	49
4.16	Comparison of full and simplified nonlinear models	50
4.17	Schematic of dead-zone with variable slope	54
4.18	Schematic of nonlinear element for 1-DOF test vehicle	56
4.19	Schematic of the 1-DOF and 3-DOF uncertain vehicle dynamics	58
4.20	Schematic of unknown dynamics for system identification	60
4.21	Bode plots of systems from identification, normalized with respect to the gain at zero frequency	62
4.22	Linear dynamics from identification and nonlinear dynamics from experiment	64

5.1	Uncertain system abstraction for control	66
5.2	Closed-loop generalized plant with nonlinear element Φ	68
5.3	Schematic of dead-zone with variable slope and constraint on z	78
5.4	Schematic of generalized plant for control synthesis	80
5.5	Nyquist plot of open-loop and closed-loop systems	82
5.6	Experiment with H_∞ and sector-constrained controllers	83
5.7	Experiment with H_∞ and sector-constrained controllers	84
5.8	Experiment with H_∞ and sector-constrained controllers	85
5.9	Pictures of steady state responses for H_∞ and sector constrained controllers	86
5.10	Experiments with H_∞ and sector-constrained controllers	87
5.11	Experiment with sector-constrained controller and agile maneuver	88
B.1	Outcome of image segmentation algorithm	102

Nomenclature

Abbreviations and Acronyms

<i>LTI</i>	Linear Time Invariant
<i>LPV</i>	Linear Parameter Varying
<i>SDP</i>	Semidefinite Programming
<i>DAQC²</i>	Data Acquisition and Control Computer
<i>c.p.</i>	Center of pressure
<i>c.g.</i>	Center of gravity

List of Symbols

\mathbb{R}	Set of real numbers
\mathbb{R}^n	Set of real vectors of dimension n
$M \succ 0$	Indicates that a matrix M is positive definite
$M \succeq 0$	Indicates that a matrix M is positive semidefinite
\mathbb{S}_+^n	Set of symmetric positive semidefinite matrices of dimension n by n
\mathbb{S}_{++}^n	Set of symmetric positive definite matrices of dimension n by n
\mathbf{x}	A vector
$\dot{\mathbf{x}}$	Time derivative of vector \mathbf{x}
$\ \cdot\ $	Norm of \cdot
t	Time (s)
g	Gravitational acceleration (m/s^2)
ρ	Fluid density (Kg/m^3)
σ	Cavitation number
p_c	Pressure inside the supercavity (Pa)
p_∞	Pressure outside the supercavity (Pa)
$\mathbf{V}_{C/f}$	Velocity of the cavitator relative to the fluid (m/s)

D_s	Maximum diameter of supercavity sections (m)
D_t	Diameter of tunnel section (m)
α	Vehicle angle of attack (rad)
q	Pitch rate, (rad/s)
θ	Pitch angle (rad)
${}^{\mathbf{B}}\mathbf{V}_{\mathbf{B}}$	Vehicle inertial velocity expressed in the body frame (m/s)
u	Axial vehicle velocity in the body frame (m/s)
w	Normal vehicle velocity in the body frame (m/s)
$\{A\}$	Coordinate frame A
${}^{\mathbf{E}}\mathbf{P}_{\mathbf{B}}$	Position of $\{B\}$ with respect to the inertial frame $\{E\}$ (m)
${}^{\mathbf{E}}T_{\mathbf{B}}$	Homogeneous transformation from $\{B\}$ to $\{E\}$
${}^{\mathbf{B}}\mathbf{V}_{\mathbf{C}}$	Cavitator velocity vector with respect to body frame (m/s)
α_c	Cavitator angle of attack (rad)
δ_c	Cavitator deflection with respect to body frame (rad)
δ_{cr}	Cavitator deflection command (rad)
D_c	Cavitator diameter (m)
A_c	Cavitator area (m^2)
C_{DC}	Cavitator drag coefficient
${}^{\mathbf{B}}\mathbf{V}_{\mathbf{F}}$	Fin velocity vector with respect to body frame (m/s)
α_f	Fin angle of attack (rad)
δ_f	Fin deflection with respect to body frame (rad)
δ_{fr}	Fin deflection command (rad)
AR	Fin aspect ratio
b_f	Fin immersion into the fluid (m)
\bar{b}_f	Fin span (m)
c_f	Fin chord (m)
Θ_0	Initial condition of pitch angle (rad)
U_0	Initial condition of axial velocity (m/s)
δ_{c0}	Trim condition for cavitator deflection (rad)
δ_{f0}	Trim condition for fin deflection (rad)
h	Planing immersion (m)
α_p	Planing angle (rad)
c_h	Correction factor to determine planing immersion
z	Relative position between the supercavity and vehicle body at the back-end (m)
λ	Immersion as the relative position between the cavity and vehicle (m)
l_c	Distance from the cavitator c.p. to the vehicle body frame (m)

l_f	Distance from the fin c.p. to the vehicle body frame (m)
l_p	Distance from the planing c.p. to the vehicle body frame (m)
L	Distance from the cavitator to the vehicle back-end (m)
a_j	Supercavity major axis of trace j (m)
b_j	Supercavity minor axis of trace j (m)
κ_j	Coefficient of supercavity displacement due to attack angle
ϵ	Distance between supercavity and vehicle body at the back-end (m)
\mathbf{d}	Vector of generalized disturbances
\mathbf{e}	Vector of generalized errors
\mathbf{u}	Vector of controller outputs
\mathbf{y}	Vector of controller inputs

Chapter 1

Introduction

Supercavitation is a developed form of cavitation in which a large gas cavity is created behind an object that moves with respect to a fluid. This phenomenon has been applied to increase the attainable speeds and decrease the power consumption of marine vehicles. An underwater vehicle surrounded by a gas cavity, referred to as supercavity, exhibits a decrease of contact area with the fluid, a reduction of skin friction drag, and ultimately an increase of speed. The attainable speeds and power efficiency of a supercavitating vehicle open new possibilities for high-speed transportation, ocean exploration, and defense. An example of a technology enabled by supercavitation is the Ghost transport vessel [13]. It travels above the water surface driven by two underwater supercavitating torpedoes to increase speed, save energy, and eliminate bouncing.

The attainable speed and power efficiency make supercavitating vehicles very attractive; however, the speed comes along with challenges in the physical modeling, control, and validation. **The major aim of this dissertation is to develop a unified framework for modeling, robust control, and experimental validation of a supercavitating vehicle.**

1.1 Vehicle

We consider a vehicle that has been widely studied in previous research efforts. It consists of a cylindrical body, a sharp disk cavitator located at the vehicle front-end, and two lateral fins at the back-end. At the cavitator edges, the flow separates and the supercavity develops. The fins provide damping and stabilization to the vehicle.

Steering the vehicle is possible by rotating the cavitator and fins. A scale vehicle with the architecture studied in this thesis is shown in Figure 1.1.

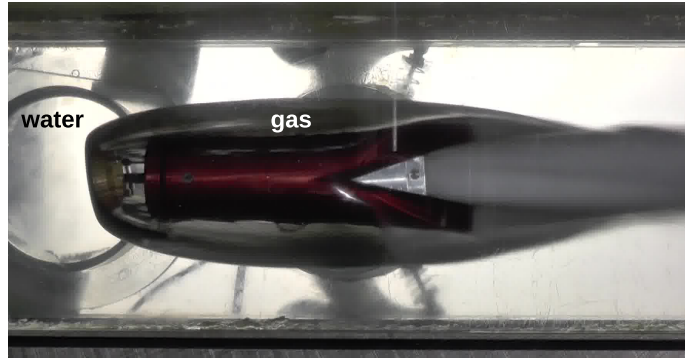


Figure 1.1: Experimental scale vehicle at the St. Falls Laboratory, University of Minnesota

1.2 Challenges and Contributions

This dissertation contributes to the existing literature with a mathematical model of a supercavitating vehicle in the longitudinal plane suited for control design under uncertainty, a robust control synthesis method, and an experimental methodology to validate control technologies.

1.2.1 Vehicle Modeling

Understanding the dynamics of the supercavitating vehicle is key to developing robust and high-performance control algorithms. Constructing automated control synthesis tools, requires a mathematical model of low dimension that captures the major dynamics of the vehicle and supercavity.

Supercavitating vessels exhibit complex dynamics not common in other underwater and aerial vehicles. When the vehicle is fully enveloped by the supercavity, only the cavitator and fins are wetted. These wetted regions together with gravity and propulsion generate the forces that drive the vehicle motion. When the vehicle back-end pierces the supercavity and immerses into the fluid, a large slapping force is suddenly created. This force is referred to as *planing*. The lift forces and pitching moments due to planing may be comparable or larger than the forces and moments generated at the control surfaces. These forces and moments may result in oscillatory motion and instability.

Characterizing planing within a mathematical model is challenging. The planing forces depend on how immersed the vehicle is into the fluid. In turn, the planing immersion is a function of the relative position of the vehicle body and supercavity. Therefore, modeling the supercavity dynamics is required to quantifying the planing forces. A first challenge in modeling the supercavity is its dependence on the vehicle states, control inputs, and flow characteristics. Another key difficulty is to characterize the supercavity interaction with the vehicle body and fluid in the planing region.

The first contribution of this dissertation is to develop a low-dimensional model of a supercavitating vehicle by integrating experimental observations and physical principles. Specifically, we integrate models that describe the vehicle hydrodynamic forces with a model of the supercavity kinematics. The vehicle dynamic models are in analytical form, with parameters that can be extracted from small scale experiments. Based upon these models, we construct an abstraction of the vehicle uncertain dynamics suitable for automated control synthesis and analysis. This abstraction characterizes the uncertainty due to the complex interaction between the supercavity and vehicle in the planing region. Another important feature is that the proposed models are able to describe the dynamics of both a vessel traveling undersea and a small scale vehicle used for experimental validation. These uncertainty models are described in Chapter 4.

1.2.2 Robust Control

The main objectives of the control algorithms of a supercavitating vehicle are to track desired trajectories, guarantee stability in the face of planing forces, and respect the actuator limits. In general, control algorithms are designed using mathematical models. These models, according to the physical system, are inaccurate to a certain level. In a supercavitating vehicle, particularly, the levels of model uncertainty are significant due to the complex interaction between supercavity and vehicle body. Therefore, robustness is a must when designing controllers for these vehicles. On the other hand, control algorithms should track the desired trajectories quickly and accurately. Thus an ideal control algorithm should provide an optimal balance between robustness and performance.

The second contribution of this dissertation is to develop control strategies and synthesis tools that guarantee stability and performance of a supercavitating vehicle in the face of nonlinear and uncertain planing forces. These

control strategies are suited to track commands and minimize actuation, do not rely on real-time measurements of planing, and are validated experimentally. In our control approach, planing immersion is not needed by the controller. Therefore, additional sensors are not needed to measure the immersion. Furthermore, the proposed output feedback controller is a linear time invariant (LTI) system whose simple form facilitates its formal validation and implementation. Our control designs also assume actuation bandwidths according to the limitations of real hardware. The robust control synthesis tools and design for the supercavitating vehicle are presented in Chapter 5.

1.2.3 Experimental Validation

Validating control schemes for a supercavitating vehicle in realistic flow conditions is beneficial because the complex vehicle dynamics may not be fully described with a computational model. However, there is a lack of affordable small-scale experimental methods in the open literature to meaningfully validate control strategies for a supercavitating vehicle.

The third contribution of this dissertation is an affordable experimental method for the dynamic validation of models and controllers of a supercavitating vehicle. We propose a dynamic test method, in which a scale supercavitating vehicle is free to rotate in a high speed water tunnel. This vehicle achieves planing naturally and exhibits oscillatory motion and instability, as desired to challenge control technologies. Testing control algorithms with such a vehicle provides insight into their strengths and drawbacks. In addition, the small scale experiments we introduce could elucidate possible pitfalls in the mathematical vehicle model and control algorithms, before undersea testing. Chapter 3 presents a description of the test-bed. In Chapter 5 we use the experimental system to demonstrate that our robust control scheme meets the desired performance in practice.

Chapter 2

Preliminaries

In this chapter, we present an overview of topics that are key to develop the rest of the thesis. Specifically, we describe the vector notation to characterize the vehicle and supercavity motion, supercavitation, the generalized equations of motion of a supercavitating vehicle, and basic concepts about stability and control performance.

2.1 Vector Notation and Transformations

In this section, we present representations and transformations for vectors in the plane. The notation is useful to track vectors with respect to multiple coordinate frames and to construct a mathematical model of a supercavitating vehicle. In addition, a homogeneous transformation is presented that help us create a computational model of the supercavity dynamics.

2.1.1 Position Vectors

A vector representing the position of a coordinate frame $\{B\}$ with respect to another coordinate frame $\{A\}$ is denoted as ${}^A\mathbf{P}_B$. Similarly, the position of a point f expressed in frame $\{A\}$ is denoted as ${}^A\mathbf{P}_f$. The origin of position vectors is needed to fully describe the position of a point. In contrast, velocity vectors are free vectors that only need a description of direction and magnitude. Position coordinates are like in the aerospace notation: ${}^A\mathbf{P}_f = \begin{bmatrix} A_{x_f} \\ A_{z_f} \end{bmatrix}$, with angles positive from A_{z_f} to A_{x_f} .

Consider the frames $\{A\}$ and $\{B\}$ depicted in Figure 2.1. We assume these frames

move and rotate in space. The origin of $\{B\}$ with respect to $\{A\}$ is ${}^A\mathbf{P}_B$. Frame $\{A\}$ is rotated by an angle α_{BA} with respect to frame $\{B\}$. A point f expressed in the frame $\{B\}$ is denoted as ${}^B\mathbf{P}_f$. The same point, with respect to frame $\{A\}$, given ${}^A\mathbf{P}_B$ and γ_{BA} is:

$${}^A\mathbf{P}_f = {}^A\mathbf{P}_B + {}^A_B R {}^B\mathbf{P}_f \quad (2.1)$$

${}^A_B R$ is a rotation transformation defined as:

$${}^A_B R = \begin{bmatrix} \cos(\gamma_{BA}) & -\sin(\gamma_{BA}) \\ \sin(\gamma_{BA}) & \cos(\gamma_{BA}) \end{bmatrix} \quad (2.2)$$

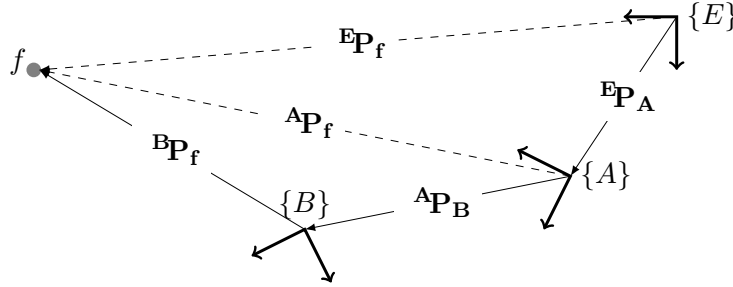


Figure 2.1: Schematic of coordinate frames on the plane

The simultaneous rotation and translation operations are merged as:

$$\begin{aligned} \begin{bmatrix} {}^A\mathbf{P}_f \\ 1 \end{bmatrix} &= \begin{bmatrix} {}^A_B R & {}^A\mathbf{P}_B \\ 0 & 1 \end{bmatrix} \begin{bmatrix} {}^B\mathbf{P}_f \\ 1 \end{bmatrix} \\ &= {}^A_B T {}^B\hat{\mathbf{P}}_f, \end{aligned} \quad (2.3)$$

where ${}^A_B T$ is a homogeneous transformation that brings the description of a point from coordinate frame $\{A\}$ to coordinate frame $\{B\}$. Homogeneous transformations are convenient to represent rotations and translations with a unique linear operator. These transformations are used in the field of robotics to conveniently study the kinematics and dynamics of robot arms [7]. Notice that we are now dealing with extended position vectors of the form: ${}^A\hat{\mathbf{P}}_f = \begin{bmatrix} {}^A\mathbf{P}_f \\ 1 \end{bmatrix}$.

Homogeneous transformations are especially helpful when a chain of coordinate frames are used to represent a position vector. For example, to express the coordinates of point f from Figure 2.1 with respect to a frame $\{E\}$ given ${}^E\mathbf{P}_A$, ${}^E_A R$, ${}^A\mathbf{P}_B$, ${}^A_B R$, and ${}^B\mathbf{P}_f$

we have:

$${}^E\hat{\mathbf{P}}_f = {}^E T_A {}^A T_B {}^B\hat{\mathbf{P}}_f \quad (2.4)$$

A notation that help us specify a homogeneous transformation based on the rotation angle γ_{BA} and relative position between frames ${}^A\mathbf{P}_B$ is:

$${}^A T_B = {}^A T_B(\gamma_{BA}, {}^A\mathbf{P}_B)$$

2.1.2 Velocity Vectors

The derivative of a position vector ${}^B\mathbf{P}_f$ with respect to time and relative to frame $\{B\}$ is given by:

$${}^B\mathbf{V}_{f/B} = \frac{d {}^B\mathbf{P}_f(t)}{dt} = \lim_{\Delta t \rightarrow 0} \frac{{}^B\mathbf{P}_f(t + \Delta t) - {}^B\mathbf{P}_f(t)}{\Delta t} \quad (2.5)$$

The velocity of f relative to frame $\{B\}$ but expressed with respect to a frame $\{A\}$ is:

$${}^A\mathbf{V}_{f/B} = {}^A R_B {}^B\mathbf{V}_{f/B} \quad (2.6)$$

When the velocity of f relative to $\{B\}$ is expressed with respect to the inertial frame $\{E\}$, we use the following notation ${}^E\mathbf{V}_{f/B} = \mathbf{V}_{f/B}$. The velocity of f relative to the inertial frame and expressed with respect to the inertial frames is denoted as ${}^E\mathbf{V}_{f/E} = \mathbf{V}_f$. Additionally, the velocity of a frame $\{B\}$ relative to the inertial frame $\{E\}$ but expressed with respect to frame $\{B\}$ is ${}^B\mathbf{V}_{B/E} = {}^B\mathbf{V}_B = {}^B R_E {}^E\mathbf{V}_B$. Note that ${}^B\mathbf{V}_B$ is not the velocity of frame $\{B\}$ relative to frame $\{B\}$ which is zero.

A position vector with respect to a frame $\{B\}$ that is moving and rotating with respect to frame $\{A\}$ is given by ${}^A\mathbf{P}_f = {}^A\mathbf{P}_B + {}^A R_B {}^B\mathbf{P}_f$. The velocity of point f with respect to $\{A\}$ is given by:

$${}^A\mathbf{V}_{f/A} = {}^A\mathbf{V}_{B/A} + {}^A R_B {}^B\mathbf{V}_{f/B} + {}^A\boldsymbol{\Omega}_B \times {}^A R_B {}^B\mathbf{P}_f, \quad (2.7)$$

${}^A\mathbf{V}_{B/A}$ is the velocity of $\{B\}$ relative to $\{A\}$ and described in $\{A\}$. ${}^A\boldsymbol{\Omega}_B$ is the angular velocities of frame $\{B\}$ with respect to frame $\{A\}$. Symbol \times denotes the cross product. In the planar case considered in this thesis ${}^A\boldsymbol{\Omega}_B = \Omega_y$ is a scalar.

2.2 Supercavitation

We focus on supercavitation with application to an underwater vehicle for which a supercavity is formed at its nose, where a flat disk cavitator is located. The cavitation number, defined as:

$$\sigma \stackrel{\text{def}}{=} \frac{2(p_\infty - p_c)}{\rho |\mathbf{V}_{\mathbf{C}/\mathbf{f}}|^2}, \quad (2.8)$$

is a parameter that describes supercavitation. p_∞ is the pressure outside the supercavity, p_c is the pressure inside the supercavity, ρ is the fluid density, and $|\mathbf{V}_{\mathbf{C}/\mathbf{f}}|$ is the relative speed between the cavitator center of pressure (c.p) and the fluid.

2.2.1 Mechanisms

Decreasing σ increases the likelihood of supercavitation. The cavitation number can be lowered and supercavitation achieved by either increasing $|\mathbf{V}_{\mathbf{C}/\mathbf{f}}|$ or by decreasing the difference $p_\infty - p_c$. In open waters, supercavitation is achieved when $\sigma < 0.1$ approximately. We illustrate the conditions in which supercavitation is possible with the following example. A vehicle traveling 5 m under the sea surface with a temperature of 15 C, requires a speed $|\mathbf{V}_{\mathbf{C}/\mathbf{f}}| > 31$ m/s to sustain supercavitation with $\sigma < 0.1$. As the vehicle descends, the hydrostatic pressure p_∞ increases and a higher speed is needed to sustain $\sigma < 0.1$ and supercavitation.

Injecting air behind the cavitator increases p_c and allows for the formation of ventilated supercavities at low speeds. *Ventilated supercavitation* is used to form supercavities until reaching natural supercavitation at higher speeds. A differentiation is often made between the ventilated cavitation number σ_c and the vaporous cavitation number σ . The former refers to ventilated supercavitation in which p_c is greater than the vapor pressure; the later refers to natural supercavitation in which p_c is the vapor pressure.

The cavitation number plays an important role in the vehicle physics. As σ decreases, the supercavity length and diameter increase. In addition, the forces at the planing regions, fins, and cavitator are influenced by the cavitation number.

2.2.2 Blockage

Supercavitation experiments are typically conducted in high-speed water tunnels in which the presence of walls has significant effects on the cavitation number and super-

cavity dimension. The effect of the tunnel walls on supercavitation is referred to as blockage. This phenomenon sets a lower limit on the achievable cavitation number. An useful inequality to identify the attainable values of σ given the tunnel and supercavity dimensions is given by [22]:

$$\left(\frac{D_s}{D_t}\right)^2 < 1 - \frac{1}{\sqrt{(1 + \sigma)}}, \quad (2.9)$$

where D_s is the diameter of the largest section of the supercavity and D_t is the diameter of the tunnel. The expression suggests that there is a lower bound on σ that depends on the dimension of the supercavity with respect to the tunnel.

Blockage decreases the supercavity diameter and also elongates the supercavity axially. Moreover, blockage affects the supercavity symmetry. When the supercavity is positioned closer to one of the tunnel walls than to the other, the supercavity tends to deform asymmetrically.

2.2.3 Gravity

Gravity influences the shape of a supercavity. At high speeds the supercavity appears symmetric with respect to the cavitator velocity vector. The effect of gravity becomes noticeable at low speeds. Gravity bends the supercavity upwards, yielding an asymmetric supercavity shape. The magnitude of the Froude number

$$F_r = \frac{|\mathbf{V}_{C/f}|}{\sqrt{gD_c}} \quad (2.10)$$

indicates how large is the effect of gravity on the supercavity. When $F_r \rightarrow \infty$, the effect of gravity on the supercavity becomes negligible and the supercavity becomes symmetric.

2.3 General Equations of Motion

The motion of a supercavitating vehicle, whose body is assumed rigid, can be described by the Newton-Euler equations [4]:

$$m \frac{d \mathbf{B}V_B}{dt} = \mathbf{B}F_c + \mathbf{B}F_f + \mathbf{B}F_p + \mathbf{B}F_g + \mathbf{B}F_\tau \quad (2.11)$$

$$\frac{d \mathbf{B}H_B}{dt} = m(\mathbf{B}\Omega_B \times \mathbf{B}P_G) \times \mathbf{B}V_B + \mathbf{B}M_c + \mathbf{B}M_f + \mathbf{B}M_p + \mathbf{B}M_g + \mathbf{B}M_\tau, \quad (2.12)$$

$\mathbf{B}V_B$ and $\mathbf{B}H_B$ are the velocity and angular momentum of a frame $\{B\}$ attached to the body and expressed with respect to frame $\{B\}$. $\mathbf{B}P_G$ is the position of the center of mass G with respect to frame $\{B\}$. m is the vehicle mass. $\mathbf{B}F_c$, $\mathbf{B}F_f$, $\mathbf{B}F_p$, $\mathbf{B}F_g$, and $\mathbf{B}F_\tau$ are the forces applied by the cavitator, fins, planing, gravity, and thrust, respectively. $\mathbf{B}M_c$, $\mathbf{B}M_f$, $\mathbf{B}M_p$, $\mathbf{B}M_g$, and $\mathbf{B}M_\tau$ are the moments about the origin of frame $\{B\}$ by the cavitator, fins, planing, gravity, and thrust, respectively. When $\{B\}$ coincides with the center of mass, $\mathbf{B}M_g = 0$.

A general form that describes the vehicle equations of motion and actuators attached to the control surfaces is:

$$\dot{\mathbf{x}}_{ol}(t) = f_{ol}(\mathbf{x}_{ol}(t), \mathbf{u}(t)) \quad (2.13)$$

$$\mathbf{y}(t) = h_{ol}(\mathbf{x}_{ol}(t), \mathbf{u}(t)) \quad (2.14)$$

$\mathbf{x}_{ol}(t) \in \mathbb{R}^{n_{ol}}$ is the state vector that includes the vehicle velocities, angles, inertial position as well as the actuator states. $\dot{\mathbf{x}}_{ol}(t)$ is the state derivative with respect to time. $f_{ol} : \mathbb{R}^{n_{ol}} \mapsto \mathbb{R}^{n_{ol}}$ is a nonlinear function that does not depend on time explicitly. $\mathbf{u}(t) \in \mathbb{R}^{n_u}$ is the input vector that includes the cavitator and fin commands. $\mathbf{y}(t) \in \mathbb{R}^{n_y}$ is the output vector that includes the system measurements such as the vehicle velocity, Euler angles, angular rates, and attack angle. This mathematical abstraction is suited to introduce concepts of stability and performance in the proceeding sections.

A control system implemented in discrete time onto an onboard embedded computer is employed to drive the vehicle motion. A continuous time representation of the controller typically takes the general form:

$$\dot{\mathbf{x}}_K(t) = f_K(\mathbf{x}_K(t), \mathbf{y}(t)) \quad (2.15)$$

$$\mathbf{u}(t) = h_K(\mathbf{x}(t), \mathbf{y}(t)), \quad (2.16)$$

$\mathbf{x}_K(t) \in \mathbb{R}^{n_K}$ is the controller state vector. $f_K : \mathbb{R}^{n_K} \mapsto \mathbb{R}^{n_K}$ is a nonlinear or linear function that we assume does not depend on time explicitly. A general form of the closed-loop system that includes the body dynamics, actuation, and controller is given by:

$$\dot{\mathbf{x}}(t) = f(\mathbf{x}(t), \mathbf{d}(t)) \quad (2.17)$$

$$\mathbf{e}(t) = h(\mathbf{x}(t), \mathbf{d}(t)) \quad (2.18)$$

$\mathbf{x}(t) = \begin{bmatrix} \mathbf{x}_{ol}(t) \\ \mathbf{x}_K(t) \end{bmatrix} \in \mathbb{R}^n$ is the state vector of the closed-loop vehicle dynamics with $n = n_{ol} + n_K$. $f : \mathbb{R}^n \mapsto \mathbb{R}^n$ is a nonlinear time invariant function. $\mathbf{e}(t) \in \mathbb{R}^{n_e}$ is the generalized error vector that includes signals to be minimized by the closed-loop system; for example, the tracking error and actuation commands. $\mathbf{d}(t) \in \mathbb{R}^{n_d}$ is the generalized disturbance vector. It includes the flow perturbations and commands for desired vehicle states.

2.4 Stability

The stability of the vehicle closed-loop dynamics is studied in this thesis using the theory proposed by Aleksandr Lyapunov [24]. We focus on the time-invariant nonlinear system described by Equations 2.17 and 2.18. In particular we study the stability of an equilibrium point $\mathbf{x}_e = 0$ for which $\mathbf{d} = 0$ and:

$$\dot{\mathbf{x}}(t) = f(\mathbf{x}_e, 0) = 0 \quad (2.19)$$

Without loss of generality, we consider the case in which $\mathbf{x}_e = 0$. Note that when $\mathbf{x}_e \neq 0$, a change of variable $\mathbf{z}(t) = \mathbf{x}(t) - \mathbf{x}_e$ results in a system $\dot{\mathbf{z}}(t) = f(\mathbf{z}(t) + \mathbf{x}_e, 0) = g(\mathbf{z}(t), 0)$ for which $g(0, 0) = 0$. Definitions of stability for the equilibrium point $\mathbf{x}_e = 0$ of the system described by Equations 2.17 and 2.18 are as follows.

Definition 1. $\mathbf{x}_e = 0$ is locally stable if for each $\epsilon > 0$ (small), there is $\delta > 0$ so that:

$$\|\mathbf{x}(0)\| < \delta \rightarrow \|\mathbf{x}(t)\| < \epsilon, \forall t \quad (2.20)$$

Definition 2. $\mathbf{x}_e = 0$ is locally asymptotically stable if there is a δ that satisfies:

$$\|\mathbf{x}(0)\| < \delta \Rightarrow \lim_{t \rightarrow \infty} \mathbf{x}(t) = \mathbf{x}_e = 0 \quad (2.21)$$

The system is globally asymptotically stable if for every $\mathbf{x}(0) \in \mathbb{R}^n$ and trajectory $\mathbf{x}(t)$:

$$\lim_{t \rightarrow \infty} \mathbf{x}(t) = \mathbf{x}_e = 0 \quad (2.22)$$

To determine if a system is locally/globally stable or asymptotically stable at an equilibrium point \mathbf{x}_e , we employ energy-like Lyapunov functions. These functions and their meaning to stability are described in Theorems 1 and 2.

Theorem 1. *Let $\mathbf{x}_e = 0$ be an equilibrium point of the system described by Equations 2.17 and 2.18 in the domain $D \subset \mathbb{R}^n$. Consider a continuously differentiable function $V : D \mapsto \mathbb{R}$ such that:*

$$V(0) = 0 \text{ and } V(\mathbf{x}(t)) > 0 \text{ for all } \mathbf{x}(t) \in D - \{0\} \quad (2.23)$$

$$\dot{V}(\mathbf{x}(t)) \leq 0, \mathbf{x}(t) \in D \quad (2.24)$$

Then, $\mathbf{x}_e = 0$ is locally stable in D .

$\mathbf{x}_e = 0$ is locally asymptotically stable in D if:

$$\dot{V}(\mathbf{x}(t)) < 0 \text{ for all } \mathbf{x}(t) \in D - \{0\} \quad (2.25)$$

Proof. The proof is presented in [16, p. 114-116]. □

Theorem 2. *Let $\mathbf{x}_e = 0$ be an equilibrium point of the system described by Equations 2.17 and 2.18. Consider a continuously differentiable function $V : \mathbb{R}^n \mapsto \mathbb{R}$ such that*

$$V(0) = 0 \text{ and } V(\mathbf{x}(t)) > 0, \forall \mathbf{x}(t) \neq 0 \quad (2.26)$$

$$\|\mathbf{x}\| \rightarrow \infty \Rightarrow V(\mathbf{x}) \rightarrow \infty \quad (2.27)$$

$$\dot{V}(\mathbf{x}(t)) < 0, \forall \mathbf{x}(t) \neq 0 \quad (2.28)$$

Then, $\mathbf{x}_e = 0$ is globally asymptotically stable and is an unique equilibrium point.

Proof. The proof is presented in [16, p. 124]. □

An important outcome from these theorems is that by finding a Lyapunov function V , we are able to prove the local or global stability of a system described by Expressions 2.17 and 2.18. In Chapter 5, we develop computational tools that evaluate the stability of a system by searching for quadratic Lyapunov functions.

2.5 Performance

We employ the notion of system gain from disturbances \mathbf{d} to error \mathbf{e} to quantify how the closed-loop system described by Equations 2.17 and 2.18 performs. One could conclude that a system with a small gain minimizes the effect of \mathbf{d} on \mathbf{e} with more success than a system with a large gain. In this thesis, we use the \mathcal{L}_2 norm of signals \mathbf{e} and \mathbf{d} to quantify their size. This choice is made due to the extensive developments in control theory based on that norm. The \mathcal{L}_2 norm of a signal \mathbf{e} is defined as:

$$\|\mathbf{e}(t)\|_2 = \left(\int_0^\infty \mathbf{e}^T(t)\mathbf{e}(t)dt \right)^{1/2} \quad (2.29)$$

This norm is equal to the square root of the signal energy. The gain from the \mathcal{L}_2 norm of \mathbf{d} to the \mathcal{L}_2 norm of \mathbf{e} , is referred to as the induced \mathcal{L}_2 norm of the system. It is an energy-like gain of the system. The following theorem, based on Lyapunov arguments, is used to compute an analytic upper bound of the induced \mathcal{L}_2 gain.

Theorem 3. *Let $\mathbf{x}_e = 0$ be an equilibrium point of the system described by Equations 2.17 and 2.18 and $\mathbf{x}(0) = 0$. Consider a continuously differentiable function $V : \mathbb{R}^n \mapsto \mathbb{R}$ such that*

$$V(0) = 0 \text{ and } V(\mathbf{x}(t)) \geq 0, \forall \mathbf{x}(t) \neq 0 \quad (2.30)$$

$$\dot{V}(\mathbf{x}(t), \mathbf{d}(t)) \leq \gamma^2 \mathbf{d}^T(t)\mathbf{d}(t) - h(\mathbf{x}(t), \mathbf{d}(t))^T h(\mathbf{x}(t), \mathbf{d}(t)), \forall \mathbf{x}(t), \forall \mathbf{d}(t) \quad (2.31)$$

Then, the induced \mathcal{L}_2 norm of the system is $\frac{\|\mathbf{e}(t)\|_2}{\|\mathbf{d}(t)\|_2} \leq \gamma$.

Proof. By integrating both sides of the above inequality and because $V(0) = 0$, we obtain:

$$\begin{aligned} 0 \leq V(\infty) - V(0) &\leq \gamma^2 \|\mathbf{d}(t)\|_2^2 - \|\mathbf{e}(t)\|_2^2 \\ &\Rightarrow \|\mathbf{e}(t)\|_2^2 \leq \gamma^2 \|\mathbf{d}(t)\|_2^2 \end{aligned}$$

□

The above theorem allows us to develop the control synthesis tools for the supercavitating vehicle in Chapter 5.

Chapter 3

Experimental Methods

The high-speed water tunnel located at the University of Minnesota St. Anthony Falls Laboratory has played a central role in our understanding of supercavitation and supercavitating vehicle control. By taking advantage of this facility, we have developed affordable methods for the modeling and control validation of a supercavitating vehicle prototype.

3.1 Related Work

Experimentation in a high-speed water tunnel is an established approach to characterize the hydrodynamic forces of hydrofoils in supercavitating flows [15, 42]. With tunnel testing, we also develop and validate models of the supercavity and forces applied to a supersaturating vehicle. These experimental methods are presented in Section 3.5.

To our knowledge, methods to validate control technologies in small scale experiments, for the nonlinear dynamics of a supercavitating vehicle, have not been presented in the open literature. In previous work [10], we developed a hybrid simulation infrastructure which is an extension of a hardware-in-the-loop test bed. In this platform, we were able to test embedded controllers for the vehicle non-planing dynamics in realistic flow conditions. However, planing, the most critical phenomenon, was not naturally captured. In this chapter, we present a test bed that enables the validation of control systems subject to planing, oscillatory motion, and instability.

3.2 High-Speed Water Tunnel

The baseline infrastructure for our experimental setup is the SAFL high-speed water tunnel. This tunnel is a recirculating, closed circuit facility capable of regulating absolute pressures and achieving velocities up to 20 m/s. Its test section is 0.19 m (width) by 0.19 m (height) by 1 m (long). A large gas collector dome removes large amounts of air during experiments. The dome enables ventilation experiments to be carried out for long periods of time without recirculation of gas-saturated water [14].

3.3 Scale Test Vehicle

The supercavitating scale vehicle shown in Figure 3.1 is used for both vehicle modeling and controller validation. This vehicle is equipped with a ventilation system that enables the formation of supercavities at speeds above 3 m/s. The test vehicle is a cylinder of 50 mm diameter and 148 mm length with an interchangeable disk cavitator and two interchangeable lateral fins. We have two servo actuators inside the vehicle body to deflect the cavitator and fins. The maximum deflections of the fins and cavitator are ± 20 deg and ± 15 deg respectively. The weight of the vehicle body is approximately 1 Kg.



Figure 3.1: Scale test vehicle

Two cavitators of 40 and 35 mm diameter are interchanged to achieve two different supercavity dimensions. Three fins referred to as small, medium, and large are used to vary fin-force effectiveness. Table 3.1 describes the dimensions of the fins and Figure 3.2 shows a photograph of them.

Description	Chord (mm)	Height (mm)	Half angle (deg)	Sweep angle (deg)
small	20	35	15	35
medium	33	43.5	30	0
large	33	55	30	0

Table 3.1: Characteristics of fins used in experiments

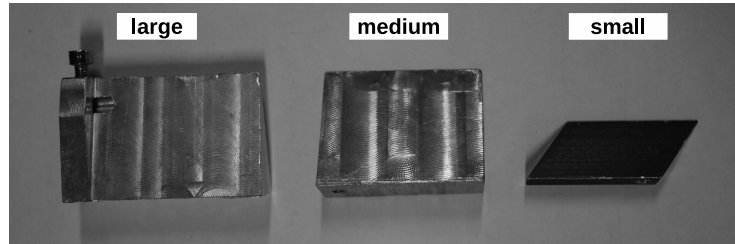


Figure 3.2: Picture of fins used in experiments

3.4 Oscillating Foil

An oscillating foil system is used to understand the effect of flow perturbations on the vehicle and supercavity dynamics. By perturbing the flow we vary the cavitator attack angle and thereby displace the supercavity. When the supercavity displacements are large enough, planing is generated. We take advantage of this manner of inducing planing to create mathematical models of the planing forces. A detailed description of the oscillating foil design is presented in [30].

3.5 Modeling Methods

The objective of the modeling platform is to characterize the supercavity kinematics and the forces applied at the cavitator, fins, and wetted planing regions. A schematic of the modeling platform is presented in Figure 3.3. The back-end of the scale vehicle is linked to a force and torque transducer that in turn is attached to the tunnel through a strut. Consequently, the vehicle motion is constrained in this setup. A real-time data acquisition and control computer (DAQC²) acquires force and torque measurements via an Ethernet interface and a User Datagram Protocol (UDP). The DAQC² also commands the vehicle's cavitator and fins via pulse width modulated (PWM) commands sent by an NI PCI-6902 data acquisition card.

A high-speed camera captures the interaction between the vehicle body and supercavity. The video streams are synchronized with the DAQC² via a light emitter diode (LED)

that turns on when the experiments start.

The software of the DAQC² computer is implemented under MATLAB/Simulink and Real-Time-Windows-Target (RTWT). RTWT enables the real-time execution of tasks in Windows operating systems. The sampling frequency for the execution of Simulink tasks is 100 Hz.

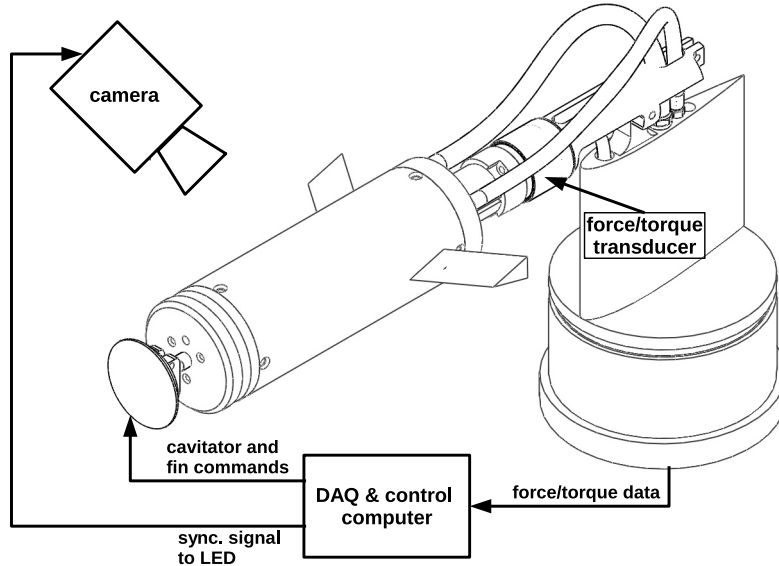


Figure 3.3: Architecture of experimental platform for modeling

3.5.1 Cavitator and Fin Forces

Mathematical models of the forces at the cavitator and fins were validated using experimental data. The cavitator and fins were commanded with sinusoids and the forces and moments were measured in real-time. The resulting force oscillations were then band-pass filtered to remove biases and high frequency vibrations and noise. Sections 4.4.3 and 4.4.4 present the cavitator and fin force models as well as related experimental data.

3.5.2 Planing Forces

Models of planing forces are constructed by using videos of the supercavity motion and planing force measurements. Planing is generated via flow perturbations using the oscillating foil gust generator as described in Section 3.4. The flow perturbations lead to variations of the cavitator attack angle, thereby displacements of the supercavity,

and ultimately planing. The planing immersion is computed via automated image segmentation algorithms.

During the experiments for planing modeling, the fins are removed to eliminate the forces that they generate due to flow perturbations. The only wetted regions of the body are therefore the cavitator and planing regions. The forces at the cavitator produced by flow perturbations, as measured in the body frame, are negligible. Details on this are presented in [10]. Force oscillations generated by flow perturbations are therefore attributed to planing only. We use this fact to measure planing forces directly, without the need of removing the cavitator forces from the data.

Two parameters describe planing immersion: planing height h and angle α_p . See Figure 3.4. During a typical planing experiment the planing immersion varies accordingly with the flow oscillations, but the planing angle remains constant. To vary the planing angle, we change the orientation of the vehicle with respect to the flow.

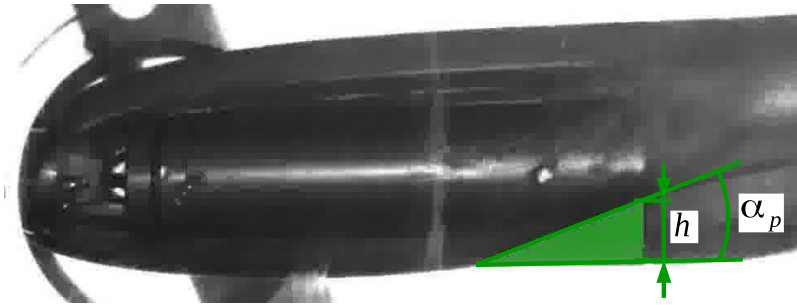


Figure 3.4: Image of the vehicle with parameters to describe the planing forces

The planing immersion and angle are measured using the high-speed camera. We compute the immersion with image segmentation algorithms and the video streams. A detailed discussion on the image segmentation technique is presented in Appendix B. Since images and force data are synchronized, the relation between planing immersion and forces is readily available from the data. These planing force models are discussed in more detail in Section 4.4.5.

3.5.3 Supercavity

An empirical model of the supercavity dynamics is created based upon experimental observations and previous studies at Caltech and in the former Soviet Union [22, 42]. To validate the supercavity model, we carried out experiments in which the supercavity

geometry is actively perturbed by deflecting the cavitator and by activating the gust generator. Both cavitator deflections and gust oscillations result in variations of the cavitator attack angle and the supercavity shape. Video streams of the supercavity motion are recorded to validate the mathematical models. A model of the supercavity dynamics and its experimental validation are presented in Section 4.5.

3.6 Control Validation Methods

A key outcome of this thesis is to show that a high-speed water tunnel can be used to understand the benefits and drawbacks of control approaches for a supercavitating vehicle. We propose that meaningful control experiments can be conducted with a scale-vehicle that rotates in a high-speed water tunnel. A pitching, one-degree of freedom (1-DOF), supercavitating vehicle captures the nonlinear interaction between the supercavity and vehicle body exhibited by undersea vehicles. It exhibits the phenomena we want for validating control technologies: planing, oscillatory motion, and instability.

Figure 3.5 depicts the proposed control validation platform. We employ the same scale vehicle for mathematical modeling. But in the control validation setup, the scale vehicle is attached to a lateral shaft that rotates freely. The angle of rotation, equal to the vehicle attack angle, is measured using a rotary encoder of 1024 pulses per revolution. By translating the rotary shaft along a slit plate, the vehicle center of rotation and dynamics are adjusted.

Between the vehicle and encoder, a force transducer is attached. The force transducer rotates together with the test vehicle. Therefore, forces applied to the vehicle are measured in the body frame. The force and torque measurements are sent to the DAQC² via an Ethernet interface and UDP data packets. The NI PCI-6902 acquisition card reads the encoder data. The same card generates PWM signals that command the positions of the actuators attached to the cavitator and fins. By commanding the cavitator and fins, the algorithms running on the DAQC² control the vehicle motion.

We synchronize the data recorded in the DAQC² and the video streams by using an LED connected to the NI PCI-6902 card. When a control experiment starts, the LED is turned on.

The control algorithms are implemented under MATLAB/Simulink and Real-Time-Windows-Target (RTWT). These software components run in the DAQC². The sampling frequency is 100 Hz. Rapid implementation and online parameterization of exper-

iments are possible with the proposed platform because Simulink parameters can be updated in real-time.

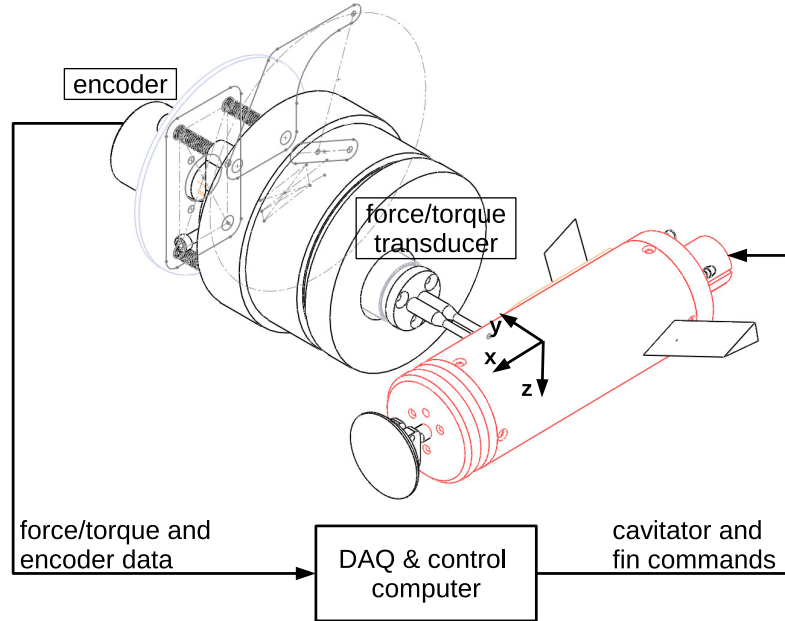


Figure 3.5: Architecture of experimental platform for control assessment

The total delay between the time at which a command is sent to the control surfaces and the time at which the vehicle responds is 3 samples (30 ms). This is the total delay in the open-loop interconnection attributed to the data acquisition card, operating system, Simulink software, and actuators.

Unsteady flows are created due to the presence of the rotary shaft downstream. When the unsteady flow interact with the fin behind the shaft, vibrations emerge. We eliminate these vibrations by removing the fin behind the rotary shaft. Therefore, in a typical experiment we place only a fin in the opposite side of the rotary shaft.

Figure 3.6 shows the scale test vehicle subject to planing and non-planing conditions during a closed-loop control experiment.

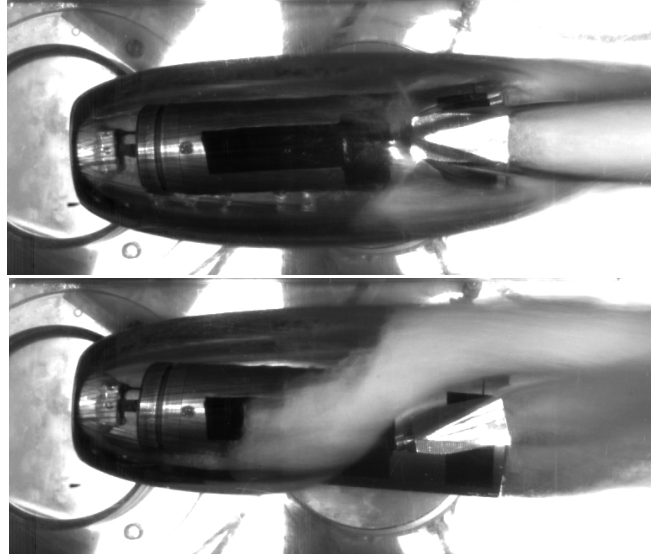


Figure 3.6: Rotatable scale vehicle in the SAFL high speed water tunnel during a closed-loop experiment. The top picture shows the vehicle in a non-planing condition. The bottom picture shows the vehicle in a planing condition at a high angle of attack.

The attributes of the proposed platform are summarized as follows:

- It is an affordable method to test control technologies before undersea testing.
- Enables the validation of mathematical models.
- Captures realistic flow conditions, vehicle-supercavity interactions, and hardware constraints as actuator saturation.

The limitations of the current platform implementation are:

- The rotational shaft pierces the supercavity, leading to lateral planing. Figure 3.7 illustrates the induced planing regions. Lateral planing forces partially attenuate the effect of switching between non-planing and planing conditions. These forces may be non-zero even when the vehicle is apparently inside the supercavity.
- The fins of our experiments have dimensions and aspect ratios that pierce the supercavity significantly and thereby induce lateral planing. Figure 3.8 illustrates the planing regions induced by the fin.



Figure 3.7: Photograph of the test vehicle from the bottom view. Lateral planing induced by the rotary shaft

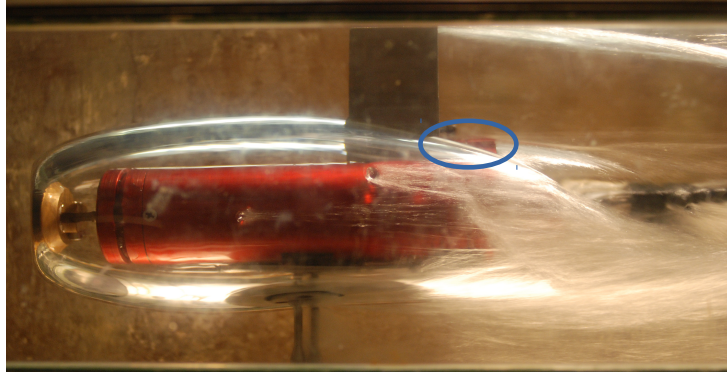


Figure 3.8: Photograph of the test vehicle from the bottom view. Lateral planing induced by the fin

Although lateral planing diminishes the effect of switching between non-planing and planing conditions, the test system still exhibits oscillatory motion and instability. To illustrate this, we carried out an experiment whose results are shown in Figure 3.9. The fin is deflected from -5 to 5 deg to generate a pitching moment that takes the vehicle to planing. During planing, the vehicle attack angle α enters into an oscillatory regime. When designing control systems a primary goal is to minimize these oscillations.

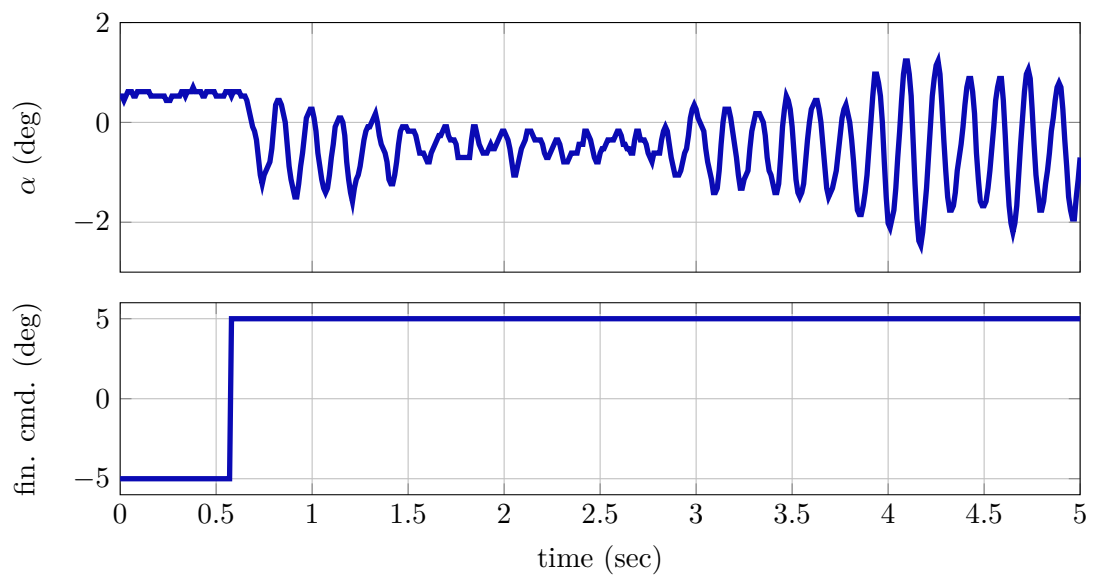


Figure 3.9: Oscillations due to planing during experiment

Chapter 4

Vehicle Modeling

In this chapter, we present medium-fidelity and low-dimensional models of the longitudinal motion of both the free to rotate vehicle operating in the tunnel (1-DOF) and unconstrained vehicle traveling undersea (3-DOF). The medium fidelity models are developed to simulate and understand the nonlinear dynamics of the vehicle motion at any velocity with a full description of the supercavity geometry. Based on the medium-fidelity models, we derive the low-dimensional abstractions, trimmed at a fixed axial speed and constructed with a simplified description of the supercavity. These low-order nonlinear models are extended to quantify modeling uncertainty. The uncertainty models we formulate inspired the control strategies presented in Chapter 5.

4.1 Related Work

According to publicly available reports and articles, investigations on supercavitation were initially carried out in the United States and former Soviet Union during the 50s and 60s. The reports in [15, 42, 43, 44] and citations therein present the research on supercavitation sponsored by the United States Department of the Navy and conducted in the Hydrodynamics Laboratory at Caltech from the early 50s. This research consisted of extensive experiments to characterize the geometry of supercavities and the hydrodynamic forces of hydrofoils subject to cavitating flows. The research in the Soviet Union has been known in the west due to the articles by Logvinovich that were translated from the Russian [22, 23]. Logvinovich studied supercavitation from a theoretical perspective with a strong support from experimental evidence. Both American and Soviet initiatives addressed thoroughly the modeling of hydrodynamic forces of cavitators, fins,

and cylinders under planing as well as the behavior of gas supercavities. Although the physics of the vehicle components were deeply studied, mathematical models from this epoch that describe the full motion of a supercavitating vehicle were never published in the public domain.

It was not until 2001, when two different benchmark models of the longitudinal motion of a supercavitating vehicle were published in [9, 17]. These investigations present low-order mathematical models of a supercavitating vehicle that consists of a cylindrical body, a disk cavitator, two lateral fins at the vehicle aft. Both mathematical models are based on the description of the supercavity and hydrodynamic forces developed by Logvinovich [22, 23]. An extension of this model that includes the dependence of the supercavity on time is presented in [2]. The models in [2, 9] have been the base for most studies on supercavitating vehicle control during the past decade. See for example [18, 26, 40, 41].

The models in [2, 9, 17] are excellent to understand what control approaches are suitable for a supercavitating vehicle. However, there are aspects of the vehicle modeling that have not been addressed and are important to develop control approaches that work in practice. These aspects include:

1. **Effect of cavitator attack angle on the supercavity dynamics.** The variations in the cavitator attack angle and deflection impact the supercavity dynamics significantly. However, such a relevant phenomenon has not been considered in control-oriented models. Knowing how the cavitator attack angle and deflection affect the supercavity geometry would benefit the design of robust and high performance control systems.
2. **Uncertainty modeling.** Imprecision in the mathematical modeling of a supercavitating vehicle requires the attention of control engineers to guarantee robustness of the closed-loop interconnection. This is specially critical due to the complex interaction between the supercavity, vehicle, and fluid at the planing regions that is challenging to capture precisely with a low-order model.

4.2 Problem Formulation

The main challenge we address in this chapter is to construct a low-order model of the uncertain dynamics of a supercavitating vehicle traveling in the longitudinal plane. The uncertainty model we seek has the following characteristics:

1. characterizes both 1-DOF vehicle prototype and 3-DOF undersea vessel
2. describes the effect of cavitator attack angle on the supercavity dynamics
3. considers the supercavity deformation in the planing region
4. includes an uncertainty description of the unmodeled aspects of the vehicle-supercavity dynamics
5. it is suitable for formal system analysis and automated control synthesis
6. provides an analytical form with parameters that can be obtained via small scale experiments

4.3 Coordinate Frames and Angles

Multiple coordinate frames facilitate the modeling of a supercavitating vehicle. These frames are located at the wetted regions, where forces are function of independent attack angles and velocities. We consider moving coordinate frames at the cavitator, fins, and body. A fixed inertial frame is also used as a reference to compute the relative positions between the vehicle and supercavity traces. A schematic with the coordinate frames is shown in Figure 4.1.

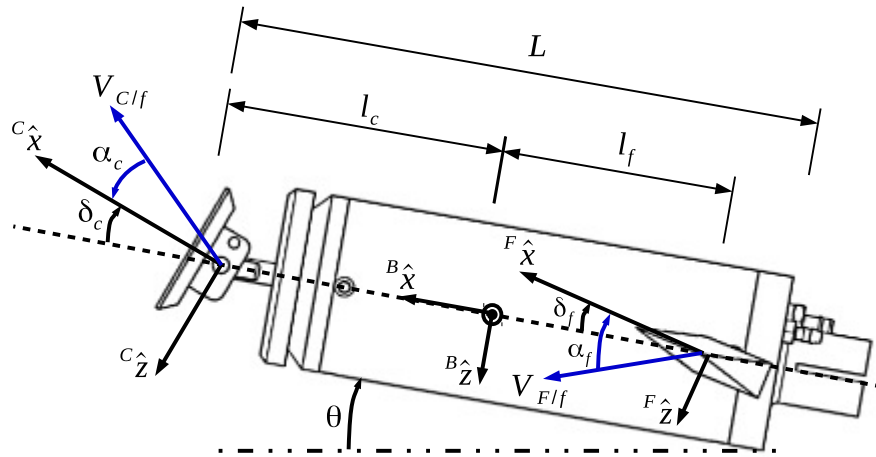


Figure 4.1: Illustration of frames and angles used for vehicle modeling

In the 3-DOF undersea vessel, the body frame $\{B\} := \{B_{\hat{x}}, B_{\hat{y}}, B_{\hat{z}}\}$ is attached to center of gravity (c.g.). This frame is attached to the center of rotation in the 1-DOF test vehicle. In both 1-DOF and 3-DOF, $B_{\hat{x}}$ is tied to the body's centerline. The pitch

angle θ is measured between the horizon and ${}^B\hat{\mathbf{x}}$. The vehicle equations of motion are written with respect to the body frame $\{B\}$. The cavitator frame $\{C\}$ formed with the orthonormal unitary vectors $\{{}^C\hat{\mathbf{x}}, {}^C\hat{\mathbf{y}}, {}^C\hat{\mathbf{z}}\}$ is attached to the cavitator control surface, ${}^C\hat{\mathbf{x}}$ is always normal to the cavitator surface and forms an angle δ_c with ${}^B\hat{\mathbf{x}}$. δ_c is referred to as cavitator deflection. The velocity of the cavitator relative to the fluid $\mathbf{V}_{C/f}$ forms an angle α_c with ${}^C\hat{\mathbf{x}}$. α_c is referred to as cavitator angle of attack. The distance between the cavitator center of pressure and vehicle frame $\{B\}$ is denoted as l_c . The fin frame $\{F\} := \{{}^F\hat{\mathbf{x}}, {}^F\hat{\mathbf{y}}, {}^F\hat{\mathbf{z}}\}$ is attached to the fin, ${}^F\hat{\mathbf{x}}$ forms an angle δ_f with ${}^B\hat{\mathbf{x}}$. δ_f is referred to as fin deflection. The velocity of the fin relative to the fluid $\mathbf{V}_{F/f}$ forms an angle α_f with ${}^F\hat{\mathbf{x}}$. α_f is referred to as fin angle of attack. The distance between the fin center of pressure and vehicle frame $\{B\}$ is denoted as l_f . The length of the vehicle, from the cavitator center of pressure to the back-end, is denoted as L . The distance from the vehicle frame $\{B\}$ to the vehicle back-end is denoted as $l_p = L - l_c$.

4.4 Forces

The dynamics of both unconstrained and experimental vehicles depend upon the forces acting at the wetted regions of the vehicle. Fortunately, the behavior of the forces at the cavitator, fins, and planing regions, in both the 1-DOF vehicle subject to blockage and 3-DOF vehicle traveling undersea is the same. We arrive at this conclusion by comparing data from our experiments, predictions from theory, and experiments in larger water tunnels. All the forces acting on the vehicle including hydrodynamic forces as well as gravitational and thrust are discussed in the proceeding sections.

4.4.1 Thrust

Thrust F_τ accelerates the unconstrained vehicle traveling undersea along its axial axis ${}^B\hat{\mathbf{x}}$. The sum of forces along ${}^B\hat{\mathbf{x}}$ should be equal to F_τ for equilibrium.

4.4.2 Gravitational

The gravitational forces expressed in the body frame are:

$$\begin{aligned} {}^B F_{g_x} &= -mg \sin(\theta) \\ {}^B F_{g_z} &= mg \cos(\theta) \end{aligned}$$

4.4.3 Cavitator

The forces at the cavitator, expressed in the body frame, are given by:

$$\begin{aligned} {}^B F_{x_c} &= -\frac{1}{2}\rho|\mathbf{V}_{\mathbf{C}/\mathbf{f}}|^2 A_c C_{DC} \cos(\alpha_c) \cos(\delta_c) \\ {}^B F_{z_c} &= \frac{1}{2}\rho|\mathbf{V}_{\mathbf{C}/\mathbf{f}}|^2 A_c C_{DC} \cos(\alpha_c) \sin(\delta_c) \end{aligned}$$

These force models apply to our 1-DOF vehicle subject to blockage and the 3-DOF vessel in open waters for which $C_{CD} = 0.815(1 + \sigma)$. ρ is the fluid density, A_c is the cavitator surface area, C_{DC} is the cavitator drag force coefficient. A detailed discussion on the cavitator forces is presented in [10].

4.4.4 Fins

Fins located at the vehicle back-end provide damping and a mechanism for active control. The fin forces are functions of the fin speed $|\mathbf{V}_{\mathbf{F}/\mathbf{f}}|$, attack angle α_f , fin span b_f , and aspect ratio AR . In contrast to conventional underwater vessels, the fin immersion of a supercavitating vehicle varies as a function of the instantaneous geometry and position of the supercavity. Hence, the fin immersion b_f and aspect ratio AR are, in general, varying with time.

Low dimensional formulas based on thin airfoil theory [5] are used to describe the forces acting on a fin that interacts with a ventilated supercavity. We assume that the fins are not fully surrounded by supercavities. The lift and drag force coefficients are:

$$C_{FL}(\alpha_f, AR) = \frac{L_f}{0.5\rho|\mathbf{V}_{\mathbf{F}/\mathbf{f}}|^2 A_f} \approx 2\pi \frac{AR}{AR + 2} \alpha_f = a_{fl} \alpha_f \quad (4.1)$$

$$C_{FD}(\alpha_f, AR) = \frac{D_f}{0.5\rho|\mathbf{V}_{\mathbf{F}/\mathbf{f}}|^2 A_f} \approx C_{FD0} + \frac{1}{\pi AR} C_{FL}^2(\alpha_f, AR) \quad (4.2)$$

$A_f = b_f \cdot c_f$ is the fin area and c_f is the fin chord. The aspect ratio is $AR = 2b_f/c_f$ as defined in [15]. It is important to highlight that b_f is the immersion of the fin into the fluid and is only a fraction of the total fin span or height \bar{b}_f .

Experimental data were acquired using the facilities described in Section 3.5.1 to validate the predictions of Expressions 4.1 and 4.2. Two swept-back wedge-shaped hydrofoils interacting with a ventilated supercavity were employed. We used two cavitators of 35 and 40 mm diameter to achieve two different supercavity sizes and thereby two values of fin immersion. The fin immersions b_f were 18 mm and 14.04 mm respectively; the aspect

ratios AR were 1.8 and 1.4; the fin chord was c_f 20 mm; and the water velocity was 5.66 m/s. Figure 4.2 shows the small fins, described in Section 3.3, during experiments with a fully developed supercavity. The immersion of the fins in the fluid was determined using photographs of the test section from the bottom view.

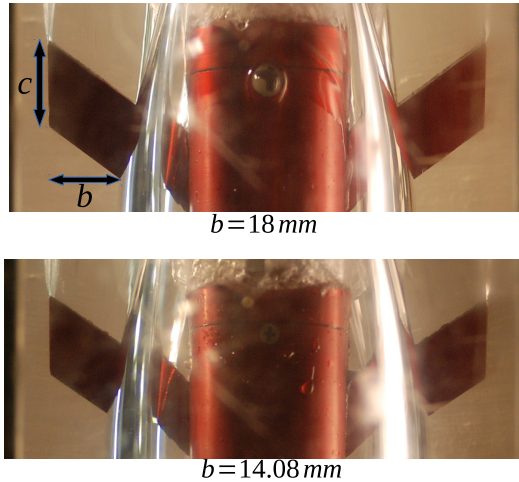


Figure 4.2: Photograph of the fins with different cavitator sizes from the bottom view of the tunnel. Top is the supercavity with a 35 mm cavitator. Bottom is the supercavity with a 40 mm cavitator

The experimental data of drag and lift coefficients together with the approximation from Equations 4.2 and 4.1 are presented in Figures 4.3 and 4.4 respectively. These plots suggest that the analytical expressions are adequate approximations of the experimental data. Discrepancies between the data and mathematical model are attributed to errors in the water speed calibration and interpretation of span, chord, and area for the swept back fin.

Because the fin immersion and aspect ratio depend on the supercavity dimension and position, we compute the fin immersion based on a geometrical model of the supercavity. The supercavity model is presented in Section 4.5 and an approach to compute the fin immersion is presented in Section 4.8.

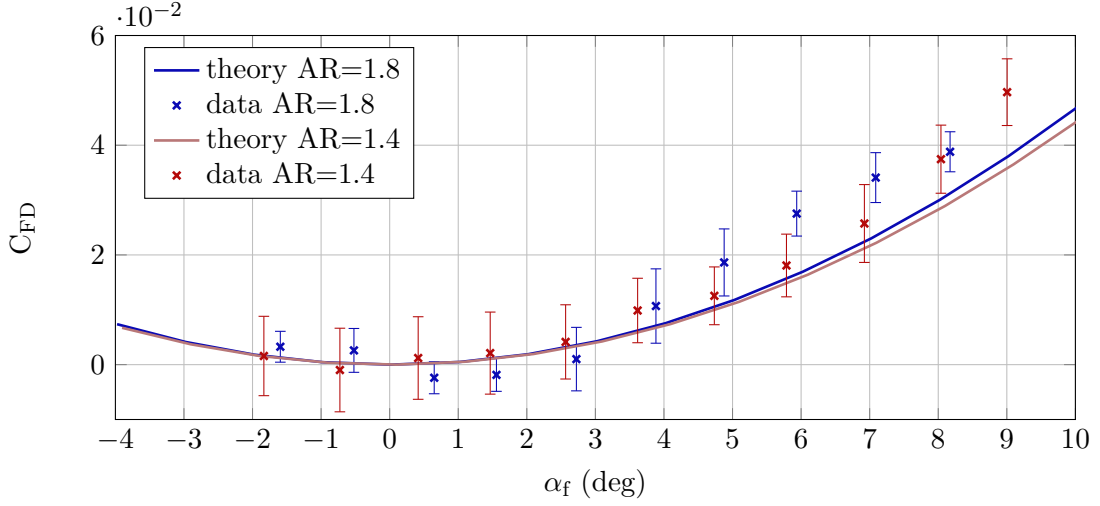


Figure 4.3: Fin drag coefficient and data

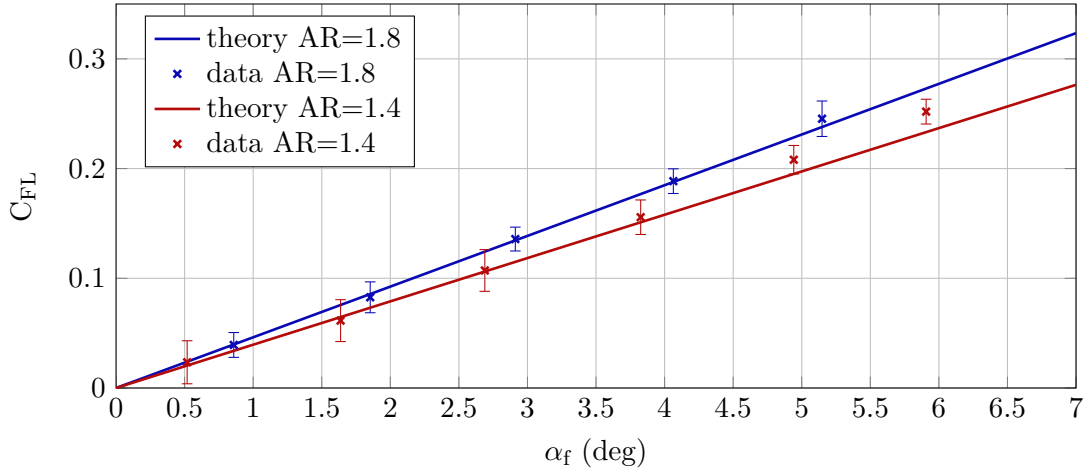


Figure 4.4: Fin lift coefficient and data

The fin forces, expressed in the body frame, where the equations of motion are written, are:

$$B_{F_{x_f}} = \frac{1}{2} \rho |\mathbf{V}_{\mathbf{F}/\mathbf{f}}|^2 A_f (-a_{fd} \alpha_f^2 \cos(\alpha_f - \delta_f) + a_{fl} \alpha_f \sin(\alpha_f - \delta_f))$$

$$B_{F_{z_f}} = \frac{1}{2} \rho |\mathbf{V}_{\mathbf{F}/\mathbf{f}}|^2 A_f (-a_{fd} \alpha_f^2 \sin(\alpha_f - \delta_f) - a_{fl} \alpha_f \cos(\alpha_f - \delta_f))$$

Although natural supercavitation is not reproduced in our experiments, it is important

to highlight that in a cavitating flow ($\sigma < 0.1$), the coefficient of lift force exhibits a decrease in slope at high attack angles. A detailed description of fin forces in cavitating flows is presented in [15]. According to [15], high aspect ratio fins increase the critical attack angles at which the slope of the force coefficient decreases. Thus, high aspect ratios are beneficial to avoid changes of the fin effectiveness at low attack angles.

4.4.5 Planing

Planing forces are generated when the vehicle after-body pierces the supercavity. These forces are the main contribution to oscillatory motion and instability for a supercavitating vessel. The primary objective of this section is to present a practical mathematical model of planing forces suited to the experimental vehicle described in Section 3.3. The problem under consideration is to compute the hydrodynamic forces applied to a cylindrical body that is partially surrounded by a supercavity and partially immersed into the fluid.

We selected the report by Waid from Caltech [44] as a guideline for modeling planing forces. The main reason being that the force models therein are suitable to fit experimental data. According to the report in [44], planing forces applied to a cylinder in a cavitating flow are functions of the planing immersion h , incidence angle α_p , cavitation number σ , and relative size between supercavity and cylinder D_s/D_{cyl} . Since the supercavity under consideration is ventilated, the effect of the cavitation number σ on the planing forces are negligible. Force variations due to D_s/D_{cyl} are significant only for $D_s/D_{cyl} \gg 1$, which is not our case. We consider supercavity and vehicle sections that are comparable in size ($D_s/D_{cyl} \rightarrow 1$). Parameters h and α_p , depicted in Figure 4.5, are initially considered to describe the planing forces.

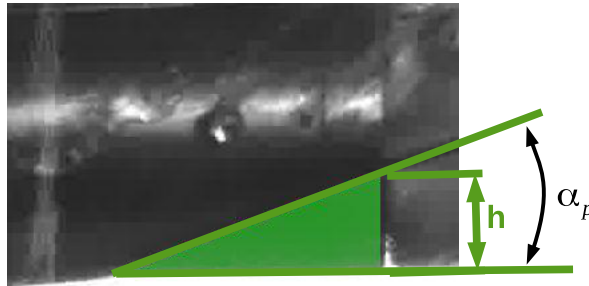


Figure 4.5: Image of vehicle back-end with parameters used to describe the planing forces

The expressions for planing forces, based on [44] and conveniently expressed in the body frame are given in:

$${}^B F_{x_p} = \frac{1}{2} \rho |\mathbf{V}_{\mathbf{p}/\mathbf{f}}|^2 D_{cyl}^2 C_{PX}(h, \alpha_p) \quad (4.3)$$

$${}^B F_{z_p} = \frac{1}{2} \rho |\mathbf{V}_{\mathbf{p}/\mathbf{f}}|^2 D_{cyl}^2 C_{PZ}(h, \alpha_p) \quad (4.4)$$

C_{PX} and C_{PZ} are the coefficients of force along the vehicle axes $\mathbf{B}_{\hat{\mathbf{x}}}$ and $\mathbf{B}_{\hat{\mathbf{z}}}$ respectively; $\mathbf{V}_{\mathbf{p}/\mathbf{f}}$ is the velocity at the planing center of pressure relative to the fluid. We would like to highlight that C_{PX} is not the drag coefficient, it is not expressed in an axis parallel to the velocity vector $\mathbf{V}_{\mathbf{p}/\mathbf{f}}$.

Planing force coefficients derived from the experiments described in Section 3.5.2 are presented in Figures 4.6 and 4.7. The plots show the normalized immersion height $\frac{h}{D_{cyl}}$ versus C_{PX} and C_{PZ} . Curves are presented for $\alpha_p = 15, 21$ and 26 deg. These measurements are fitted to first and third order polynomials respectively. The curves in Figures 4.6 and 4.7 represent the polynomials and the error bars indicate the standard deviations of the data samples at different angles. The polynomials that describe the data are:

$${}^B F_{x_p} = \frac{1}{2} \rho |\mathbf{V}_{\mathbf{p}/\mathbf{f}}|^2 D_{cyl}^2 \left[a_{px1}(\alpha_p) \left[\frac{h}{D_{cyl}} \right] + a_{px2}(\alpha_p) \left[\frac{h}{D_{cyl}} \right]^2 + a_{px3}(\alpha_p) \left[\frac{h}{D_{cyl}} \right]^3 \right] \quad (4.5)$$

$${}^B F_{z_p} = \frac{1}{2} \rho |\mathbf{V}_{\mathbf{p}/\mathbf{f}}|^2 D_{cyl} a_{pz}(\alpha_p) h \quad (4.6)$$

With our experimental setup, we could only obtain the curves of the force coefficients for angles between 15 and 26 deg. This has limited the accuracy of the planing model. However, according to Figure 4.7, the effect of moderate variations of α_p on C_{PZ} is much less significant than the effect of h . Additionally, because ${}^B F_{z_p}$ is the main contributor to the vehicle pitching motion, we assume a constant value of α_p . The imprecision in modeling the effect of α_p by using a constant value of a_{pz} is accounted for in the uncertainty modeling proposed in Section 4.9.

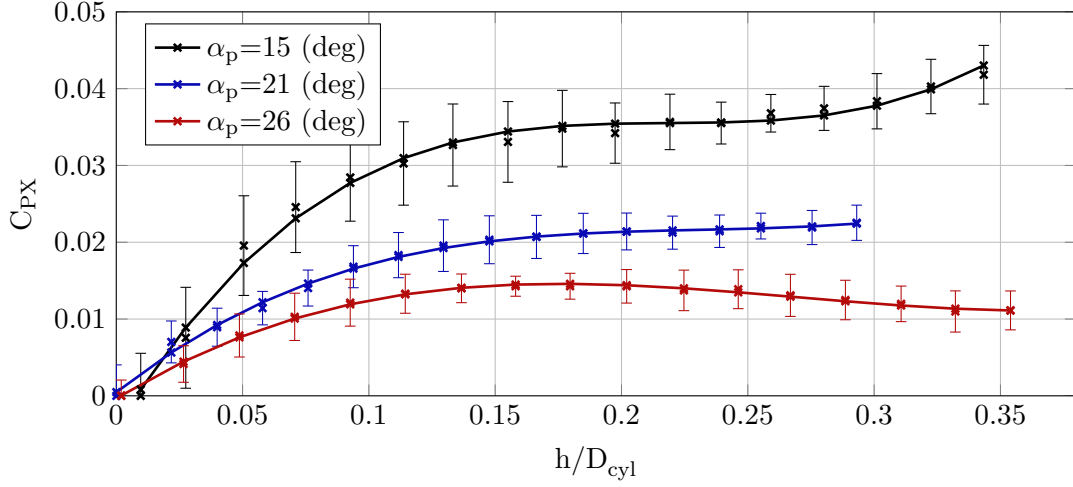


Figure 4.6: Coefficient of planing force along $\mathbf{B}_{\hat{x}}$. The length of the error bars correspond to the standard deviations. The water speed was 5.1 m/s at which no significant vibrations were observed and clean data were obtained.

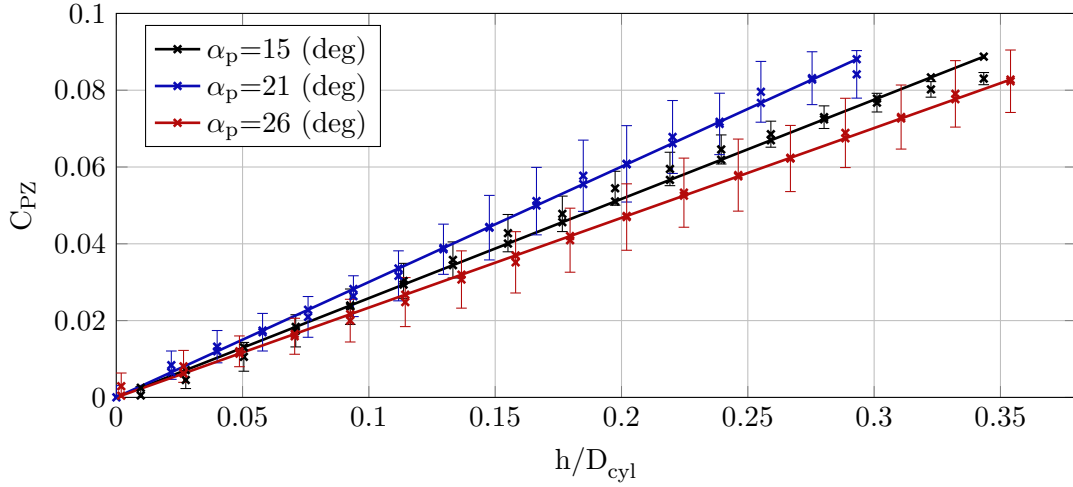


Figure 4.7: Coefficient of planing force along $\mathbf{B}_{\hat{z}}$.

Now the challenge is to compute h . We calculate h by using a dynamic model of the supercavity geometry presented in the proceeding section.

4.5 Supercavity

A low-order mathematical model of the supercavity dynamics is presented in this section. We have combined research outcomes from Caltech and by Logvinovich to construct a supercavity model suitable to characterize the longitudinal dynamics of a supercavitating vehicle. This model describes a supercavity in of both a water tunnel subject to blockage and open waters.

4.5.1 1-DOF Test Vehicle

The approach to describe the supercavity at Caltech [42] is extended herein to characterize the steady geometry of symmetric and asymmetric supercavities. We select the approach from Caltech because the supercavity models can be easily fitted to photographs from experiments.

The report in [42] suggests that the points along the edges of a steady supercavity can be described by a semi-elliptical function. We use two semi-ellipses, given by:

$$z_j = (-1^j)b_j \left(1 - \left(\frac{-x_j - a_j}{a_j} \right)^2 \right)^{1/\eta}, \quad (4.7)$$

to characterize the upper and lower traces of the supercavity independently and therefore capture the asymmetry of the supercavity exhibited by our experimental vehicle. This asymmetry is due to gravity and asymmetric blockage as discussed in Section 2.2. $\mathbf{J}\mathbf{P}_j = \begin{bmatrix} x_j \\ z_j \end{bmatrix}$ represents a point along the trace $j = [1, 2]$ of the supercavity; $j = 1$ corresponds to the upper trace and $j = 2$ to the lower trace. The supercavity points are defined with respect to the supercavity frame $\{J\}$, which is described by the unitary orthonormal vectors $\{\hat{\mathbf{x}}_j, \hat{\mathbf{z}}_j\}$. The origin of this frame coincides with the location of the cavitator edge at which the flow separates. The coordinate $\hat{\mathbf{x}}_j$ is parallel to the velocity of the cavitator relative to the fluid $\mathbf{V}_{\mathbf{C}/\mathbf{f}}$. a_j is the distance along $\hat{\mathbf{x}}_j$ from the cavitator edge to the location of maximum supercavity radius. b_j is the distance along $\hat{\mathbf{z}}_j$ from the cavitator edge to the wall at the section of maximum radius. Figure 4.8 depicts the parameters of the semi-elliptical model of the supercavity.

In a typical experiment to characterize the supercavity of our scale vehicle, we use a cavitator of 0.04 m diameter, a ventilation rate of 60 liters per minute, and a water speed of 4.08 m/s. For these conditions we obtain a clear supercavity and the following parameters: $a_1 \approx 0.23$ m, $b_1 \approx 0.038$ m, $a_2 \approx 0.145$ m, $b_2 \approx 0.028$ m, $\eta = 1.8$. A

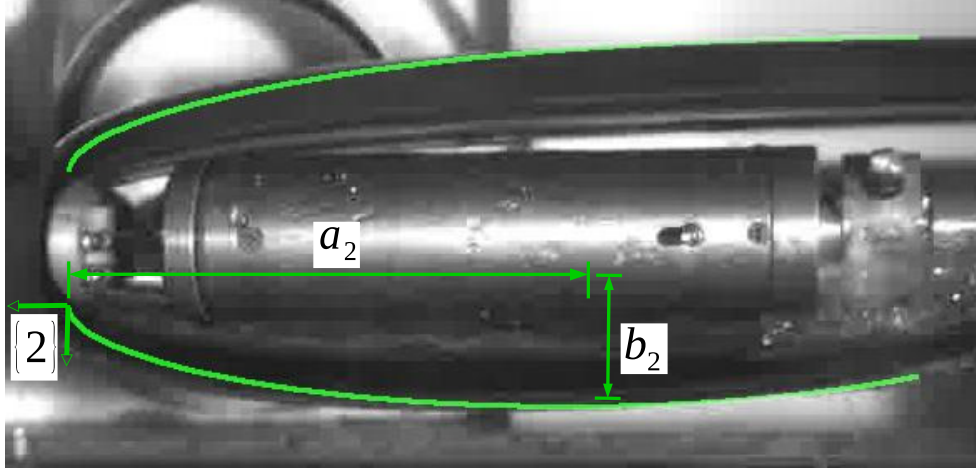


Figure 4.8: Supercavity and parameters for semi-elliptical models

detailed discussion on how blockage affects the supercavity dimensions in variety of flow conditions is presented in [14].

4.5.2 3-DOF Undersea Vehicle

The investigations in [22, 42] describe a *symmetric* supercavity in open waters (no blockage) for which $a_1 = a_2 = a$ and $b_1 = b_2 = b$. The dimensions of the supercavity, derived via experiments with ventilated supercavities in [42], are given by:

$$\frac{a}{D_c} = \frac{0.54}{\sigma^{1.118}} \quad (4.8)$$

$$\frac{b}{D_c} = \frac{0.267}{\sigma^{0.568}} \quad (4.9)$$

The pressure inside the supercavity, used to compute the cavitation number σ for the above expressions, was measured with a transducer located behind the cavitator. Approximations to the dimensions of a natural supercavity (no ventilation) suggested by Logvinovich [22] are given by:

$$\frac{a}{D_c} = \frac{1}{0.96\sigma} - \frac{3}{2} \quad (4.10)$$

$$\frac{b}{D_c} = \frac{1}{2} \left(\sqrt{\frac{0.815(1+\sigma)}{\sigma}} - 1 \right) \quad (4.11)$$

Figure 4.9 shows the values of a and b as functions of σ given by Expressions 4.8-4.9 and 4.10-4.11. Interestingly, the experimental data on ventilated supercavitation from Caltech validate the predictions on natural supercavitation by Logvinovich.

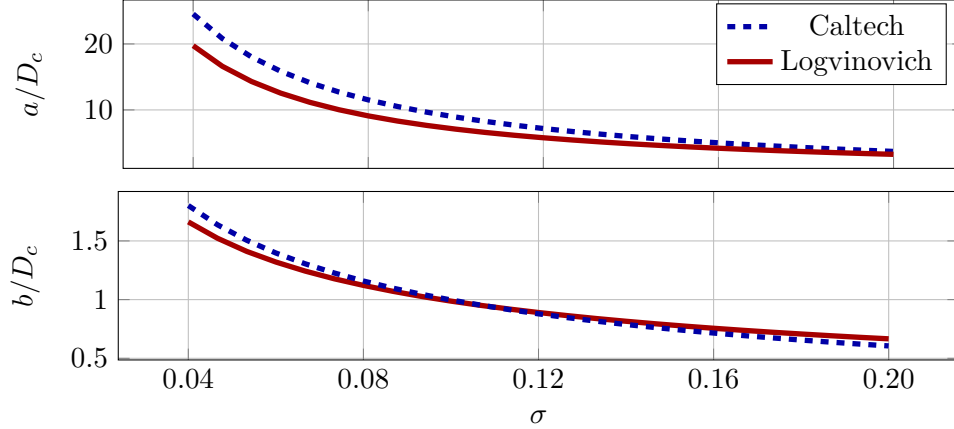


Figure 4.9: Parameters a and b normalized via the cavitator diameter D_c for a symmetric supercavity with no blockage effects

4.5.3 Effect of Cavitator Attack Angle

Available dynamical models of a supercavitating vehicle do not characterize the effect of the cavitator attack angle α_c on the supercavity dynamics. However, this is critical to understand how to control the vehicle dynamics. Fortunately, Waid at Caltech and Logvinovich in the Soviet Union already investigated the effect of α_c on the supercavity geometry. The studies at Caltech [42] present a relation between the elliptical parameters a_j and b_j and the attack angle α_c in the form of empirical curves. This approach complicates the derivation of a low-order model of the vehicle dynamics.

A more convenient method to describe the effect of α_c was that proposed by Logvinovich [22]. He pointed out that a non-zero lift force L_c at the cavitator, perpendicular to the cavitator velocity vector $\mathbf{V}_{C/f}$, results in a displacement of the supercavity along $\hat{\mathbf{z}}_j$. The displacement of the supercavity, adapted from [22], is given by:

$$\Delta_{z_j}(x_j) = -\frac{L_c}{\pi\rho|\mathbf{V}_{C/f}|^2}f_{\Delta z}(x_j)$$

$$f_{\Delta z}(x_j) = \int_0^{x_j} \frac{d\xi}{R_s^2(\xi)} = \int_0^{x_j} \left(R_c + b_j \left(1 - \left(\frac{\xi - a_j}{a_j} \right)^2 \right)^{1/\eta} \right)^{-2} d\xi$$

where $R_c = D_c/2$ is the cavitator radius and $R_s = R_c + z_j$ is the supercavity radius along an axis parallel to $\mathbf{V}_{C/f}$. Given that the cavitator lift force is:

$$L_c \approx \frac{1}{2} \rho |\mathbf{V}_{C/f}|^2 C_{CD} A_c \cos(\alpha_c) \sin(\alpha_c),$$

we can rewrite the supercavity displacement as:

$$\begin{aligned} \Delta_{zj}(x_j) &= -\frac{1}{2\pi} C_{CD} A_c \cos(\alpha_c) \sin(\alpha_c) f_{\Delta_{zj}}(x_j) \\ \Delta_{zj}(x_j) &\approx -\frac{1}{2\pi} C_{CD} A_c \alpha_c f_{\Delta_{zj}}(x_j) \end{aligned}$$

Figure 4.10 presents a numerical solution of $f_{\Delta_z}(x_j)$ for the supercavity shown in Figure 4.8 together with a linear approximation given by:

$$f_{\Delta_{zj}}(x_j) \approx \frac{f_{\Delta_{zj}}(2a_j)}{2a_j} x_j = \kappa_{0j} x_j$$

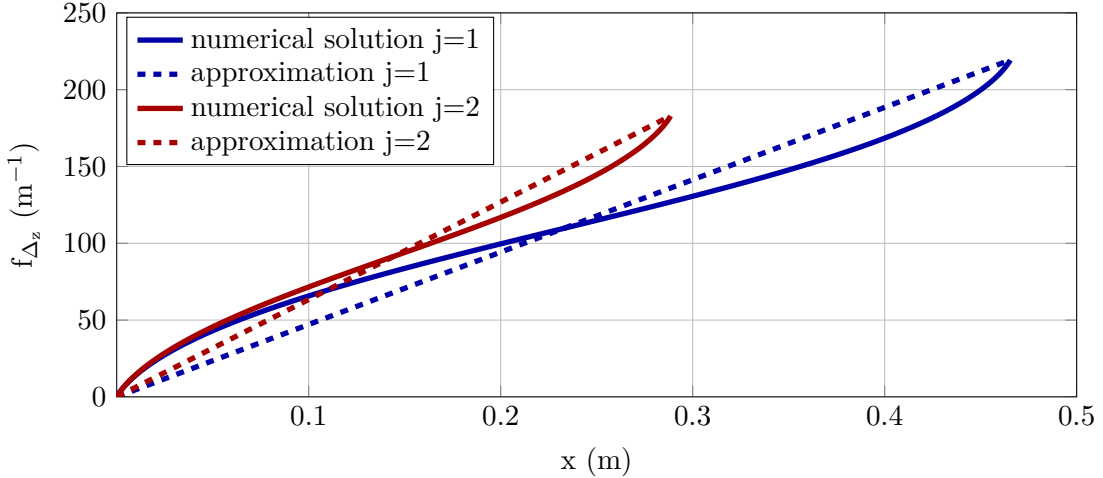


Figure 4.10: Function $f_{\Delta_{zj}}$ for $j = 1, 2$ to characterize the supercavity displacements due to α_c . Curves are for $x_j \in [0, 2a_j]$. The supercavity parameters estimated using photographs are: $a_1 = 0.23$, $b_1 = 0.038$ m, $a_2 = 0.145$ m, $b_2 = 0.028$ m, $R_c = 0.02$ m

κ_{0j} needs to be computed for each flow condition. A low-order description of the displacement of the supercavity is given by:

$$\Delta_{zj}(x_j) \approx -\frac{1}{2\pi} C_{CD} A_c \alpha_c \kappa_{0j} x_j = -\kappa_j \alpha_c x_j$$

and the position of a point along the supercavity edges as a function of α_c , is given by:

$$\mathbf{J}\mathbf{P}_j = \begin{bmatrix} x_j \\ z_j - \kappa_j \alpha_c x_j \end{bmatrix} \quad (4.12)$$

This simple approximation shows excellent match with experimental data as demonstrated in Section 4.5.5.

4.5.4 Time Dependent Model

The mathematical model of the supercavity described by Equations 4.7 and 4.12 assumes that the points along the supercavity traces depend only on the current states of the cavitator. This model is not accurate to characterize a supercavity when the cavitator velocity, attack angle, and position vary with time. For this reason, a dynamic model of the supercavity is constructed herein. The proposed time-dependent model is based upon two statements by Logvinovich [22]. First, the sections of the supercavity can be considered independent of each other to describe their motion. Second, a supercavity section depends on the cavitator states at the time it is created at the cavitator edges.

A model that considers the motion of both the cavitator and fluid with respect to an inertial frame is needed to describe the supercavity of our test vehicle. We propose a model that obeys the following rules:

1. The time evolution of a supercavity trace $j = [1, 2]$ is described by points $\mathbf{I}\mathbf{P}_{ij}(t)$ for $i = 1, 2, \dots, N$.
2. Points $\mathbf{I}\mathbf{P}_{ij}(t) = \begin{bmatrix} x_{ij}(t) \\ z_{ij}(t) \end{bmatrix}$ along the supercavity traces expand and contract with respect to individual coordinate frames $\{IJ\}$. These frames are fixed to the locations where the cavitator creates the supercavity sections ij at time τ_i . Because a supercavity point $\mathbf{I}\mathbf{P}_{ij}(t) = \begin{bmatrix} x_{ij}(t) \\ z_{ij}(t) \end{bmatrix}$ coincides with the cavitator edges at time τ_i , $i = 1, 2, \dots, N$, we have:

$$\begin{bmatrix} x_{ij}(\tau_i) \\ z_{ij}(\tau_i) \end{bmatrix} = \begin{bmatrix} 0 \\ 0 \end{bmatrix}$$

3. The unitary orthonormal vectors $\{\hat{\mathbf{x}}_{ij}, \hat{\mathbf{z}}_{ij}\}$ define the frames $\{IJ\}$. Axis $\hat{\mathbf{x}}_{ij}$ is parallel to $\mathbf{V}_{\mathbf{C}/\mathbf{f}}(\tau_i)$, which is the velocity of the cavitator with respect to the fluid at time τ_i . When the fluid velocity is zero, $\mathbf{V}_{\mathbf{C}/\mathbf{f}}(\tau_i)$ is only due to the cavitator

motion, and point ${}^{\mathbf{I}}\mathbf{P}_{ij}(t)$ expands along the normal axis $\hat{\mathbf{z}}_{ij}$. This means that $x_{ij}(t) = 0$ for all t . When the fluid velocity is nonzero, $\mathbf{V}_{\mathbf{C}/\mathbf{f}}(\tau_i)$ is due to both the vehicle and fluid motion, and point ${}^{\mathbf{I}}\mathbf{P}_{ij}(t)$ expands along both $\hat{\mathbf{x}}_{ij}$ and $\hat{\mathbf{z}}_{ij}$.

4. The evolution of the points that describe the supercavity trace are given in Equation 4.13, where ${}^{\mathbf{I}}\mathbf{V}_{\mathbf{f}}$ is the velocity of the fluid expressed in the frame $\{IJ\}$.

$$\begin{bmatrix} x_{ij}(t) \\ z_{ij}(t) \end{bmatrix} = \begin{bmatrix} -|{}^{\mathbf{I}}\mathbf{V}_{\mathbf{f}}(\tau_i)|(t - \tau_i) \\ (-1^j)b_j \left[1 - \left(\frac{|\mathbf{V}_{\mathbf{C}/\mathbf{f}}(\tau_i)|(t - \tau_i) - a_j}{a_j} \right)^2 \right]^{1/\eta} - \kappa_j \alpha_c x_{ij}(t) \end{bmatrix} \quad (4.13)$$

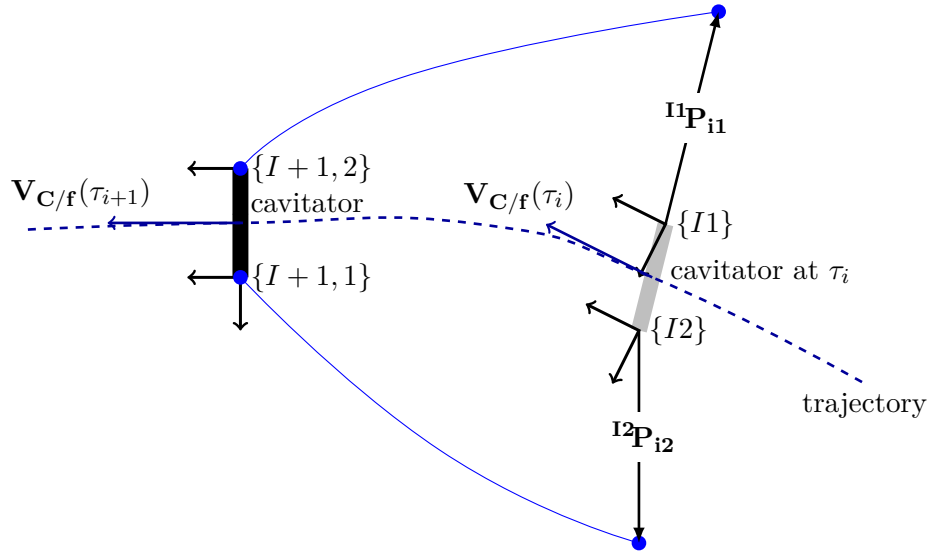


Figure 4.11: Schematic of supercavity dynamic model. Cavitor at current time $t = \tau_{i+1}$ in black; cavitor at previous time τ_i in gray.

So far, we have $2N$ points along the supercavity traces described in $2N$ distinct coordinate frames $\{IJ\}$ for $i = 1, 2, \dots, N$ and $j = 1, 2$. To reconstruct the supercavity geometry, we express the supercavity points with respect to an inertial frame $\{E\}$. A chain of homogeneous transformations, described in Section 2.1, is employed to transform the coordinates of the supercavity points from the $\{IJ\}$ frames to the inertial

frame $\{E\}$. The inertial positions are given by:

$$\begin{aligned}
\mathbf{E}\hat{\mathbf{P}}_{ij}(t) &= \mathbf{}^E_B T \mathbf{}^B_C T \mathbf{}^C_{IJ} T \mathbf{I}\hat{\mathbf{P}}_{ij}(t) \\
\mathbf{I}\hat{\mathbf{P}}_{ij} &= \begin{bmatrix} \mathbf{I}\mathbf{P}_{ij} & 1 \end{bmatrix}^T \\
\mathbf{C}\mathbf{P}_{IJ} &= (-1^j) \begin{bmatrix} 0 & D_c/2 \end{bmatrix}^T \\
\mathbf{B}\mathbf{P}_C &= \begin{bmatrix} l_c & 0 \end{bmatrix}^T \\
\mathbf{E}\mathbf{P}_B(t) &= \mathbf{E}\mathbf{P}_B(0) + \int_0^t \mathbf{}^E_B R(\xi) \mathbf{B}\mathbf{V}_B(\xi) d\xi \\
&= \begin{bmatrix} E_{x_B}(0) \\ E_{z_B}(0) \end{bmatrix} + \int_0^t \left(\begin{bmatrix} \cos(\theta(\xi)) & \sin(\theta(\xi)) \\ -\sin(\theta(\xi)) & \cos(\theta(\xi)) \end{bmatrix} \begin{bmatrix} B_u(\xi) \\ B_w(\xi) \end{bmatrix} \right) d\xi
\end{aligned}$$

where $\mathbf{}^E_B T(-\theta(\tau_i))$, $\mathbf{E}\mathbf{P}_B(\tau_i)$, $\mathbf{}^B_C T(-\delta_c(\tau_i))$, $\mathbf{B}\mathbf{P}_C$, $\mathbf{}^C_{IJ} T(\alpha_c(\tau_i))$, $\mathbf{C}\mathbf{P}_{ij}$ are homogeneous transformations that bring vectors from coordinate frames $\{B\}$, $\{C\}$, and $\{IJ\}$ to frames $\{E\}$, $\{B\}$, and $\{C\}$ respectively. Since the 1-DOF vehicle does not translate with respect to the inertial frame, $\mathbf{E}\mathbf{P}_B(t) = \mathbf{E}\mathbf{P}_B(0)$.

4.5.5 Experimental Validation

An experiment with the methods presented in Section 3.5 was carried out to validate the time-dependent model of the supercavity. We kept the scale experimental vehicle fixed to the tunnel. Flow perturbations were created using the gust generator described in Section 3.5.3. These flow disturbances vary the cavitator attack angle α_c and thereby induce morphological changes in the supercavity. With high frequency oscillations, the dependence on time of the supercavity geometry is noticeable. These changes in the supercavity geometry together with our high-speed video capability enabled us to validate the time-dependent model of the supercavity.

In the experiment, videos were recorded at 1000 frames per second. A water speed of 4.08 m/s allowed us to create a clear supercavity and capture its dynamics with the camera. Oscillations of the gust generator were at $f_g = 10$ Hz and described by $\alpha_g(t) = 6 \sin(2\pi f_g t)$. We assume that these oscillations induced variations to the cavitator attack angle of the form $\alpha_c(t) \approx 6 \sin(2\pi f_g t + \psi)$ for which ψ captures the effect of spatial separation between the oscillating foil and the cavitator. The phase lag ψ is manually computed using the videos and data. Notice that we assume that there is no attenuation nor amplification of the oscillations.

This experiment corresponds to the case in which the cavitator has zero velocity with respect to the inertial frame and the fluid moves toward the cavitator. Therefore, $\mathbf{V}_{C/f}$ is only due to the fluid motion. Since the cavitator does not move relative to the inertial frame $\{E\}$, the frames $\{IJ\}$ for $i = 1, 2, \dots, N$ are always located at the cavitator edges.

Figure 4.12 shows images of the supercavity at different times during the experiment and the mathematical model drawn on top. The model has a remarkable level of accuracy, given its simplicity.

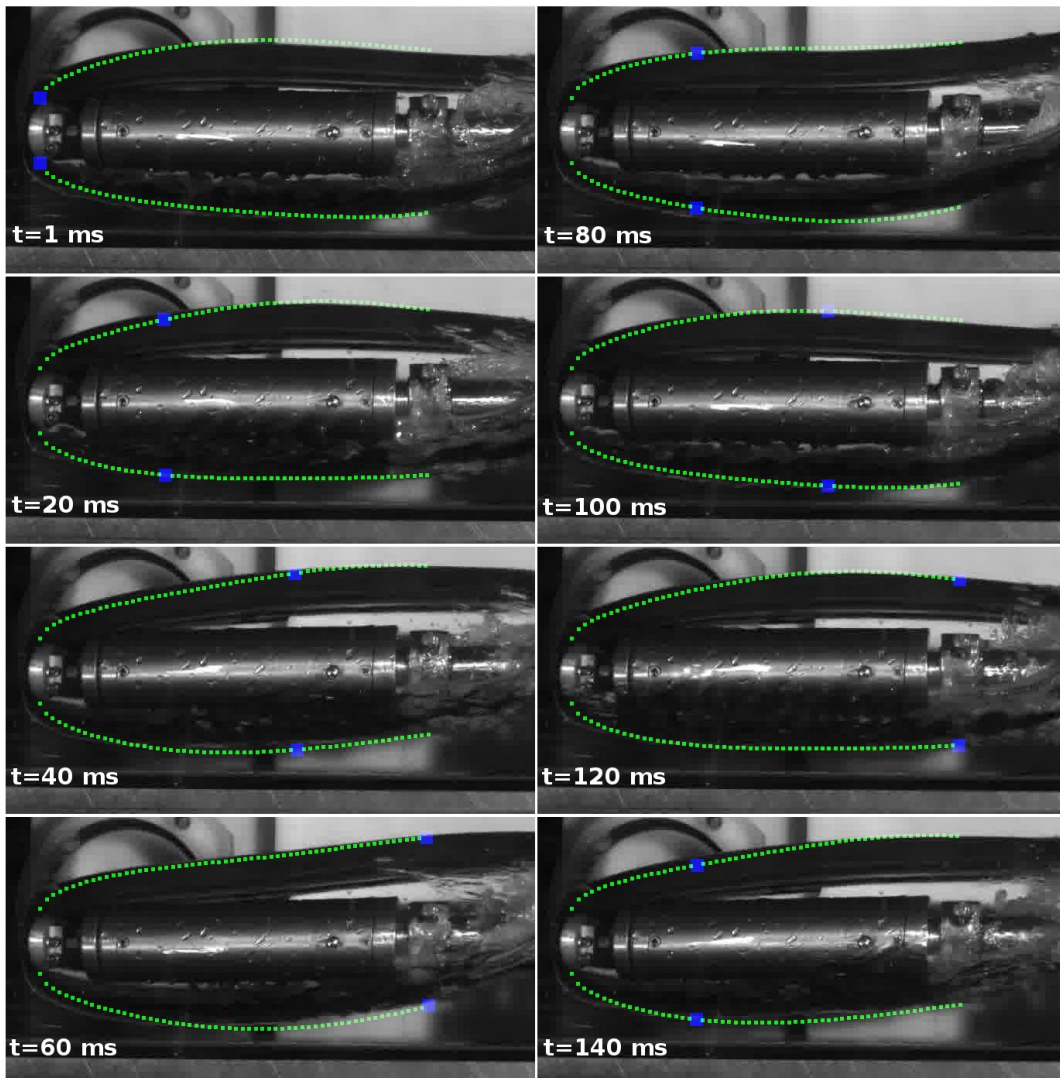


Figure 4.12: Comparison of supercavity dynamic model with photographs during an experiment in which the gust generator is activated at 10 Hz

4.5.6 Vehicle Immersion

Given the mathematical description of the supercavity, we are now ready to compute an approximation of the vehicle immersion into the fluid during planing. Unfortunately, computing the immersion via the relative position between the supercavity and body is inaccurate. This approach neglects how the supercavity is deformed in the planing region as a result of the interaction between the supercavity, fluid, and body. Figure 4.13 shows that the immersion (blue region) computed by neglecting the supercavity deformation is smaller than the actual immersion (blue and green regions).

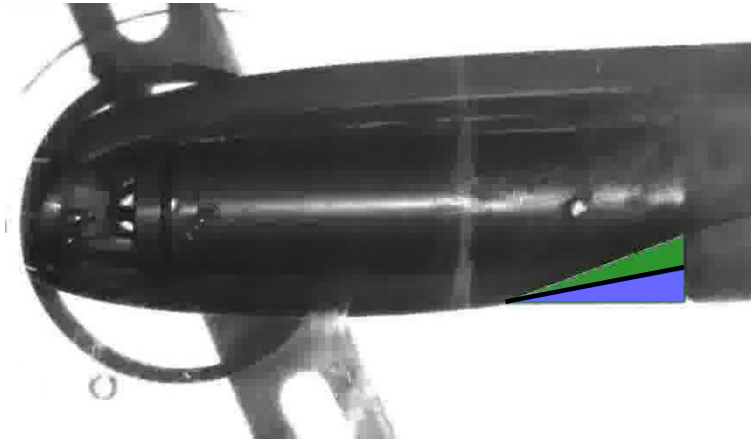


Figure 4.13: Actual and idealized planing immersion

To characterize the deformation of the supercavity when it is pierced by the vehicle afterbody, we compute the immersion as $h(t) = c_h \lambda(t)$, where c_h is a correction factor and $\lambda(t)$ is the immersion computed by using the relative position between the supercavity and vehicle. A value of $c_h = 2$ matches the observations from our experiments. But we anticipate that computing the immersion in this way is inaccurate because c_h may vary according to the water speed, ventilation, and blockage. The inaccuracy in characterizing the planing immersion through c_h is accounted for in the uncertainty modeling of the vehicle dynamics presented in Section 4.9.

4.6 Vehicle Dynamics

The mathematical models of both 3-DOF and 1-DOF vehicles are introduced in this section.

4.6.1 Unconstrained 3-DOF Vehicle

The longitudinal equations of motion for the 3-DOF vessel, are given by:

$$m(\dot{u}(t) + q(t)w(t)) = {}^B F_{x_c}(t) + {}^B F_{x_f}(t) + {}^B F_{x_p}(t) + {}^B F_{x_g}(t) + {}^B F_{x_\tau}(t) \quad (4.14)$$

$$m(\dot{w}(t) - q(t)u(t)) = {}^B F_{z_c}(t) + {}^B F_{z_f}(t) + {}^B F_{z_p}(t) + {}^B F_{z_g}(t) \quad (4.15)$$

$$I_{yy}\dot{q}(t) = {}^B M_{y_c}(t) + {}^B M_{y_f}(t) + {}^B M_{y_p}(t) \quad (4.16)$$

$$\dot{\theta}(t) = q(t) \quad (4.17)$$

$$\frac{d}{dt} \left({}^E \mathbf{P}_B(t) \right) = \begin{bmatrix} {}^E \dot{x}_B(t) \\ {}^E \dot{z}_B(t) \end{bmatrix} = \begin{bmatrix} \cos(\theta(t)) & \sin(\theta(t)) \\ -\sin(\theta(t)) & \cos(\theta(t)) \end{bmatrix} \begin{bmatrix} u(t) \\ w(t) \end{bmatrix} \quad (4.18)$$

The force and moment equations are expressed in the body frame $\{B\}$ whose origin coincides with the center of gravity. q and θ are the pitch rate and angle; \dot{u} , \dot{w} , u and w are the accelerations and velocities of the body expressed in the body axes ${}^B \hat{\mathbf{x}}$ and ${}^B \hat{\mathbf{z}}$; m and I_{yy} are the vehicle mass and moment of inertia about ${}^B \hat{\mathbf{y}}$; ${}^B F_{x_c}$, ${}^B F_{z_c}$, and ${}^B M_{y_c}$ are the forces and moment generated by the cavitator; ${}^B F_{x_f}$, ${}^B F_{z_f}$, and ${}^B M_{y_f}$ are the forces and moment generated by the fins; ${}^B F_{x_p}$, ${}^B F_{z_p}$, and ${}^B M_{y_p}$ are the forces and moment generated by planing; ${}^B F_{x_\tau}$ is the force generated by thrust; ${}^B F_{x_g}$ and ${}^B F_{z_g}$ are the forces generated by the gravitational acceleration. The position of the vehicle body frame $\{B\}$ with respect to the inertial frame $\{E\}$ is ${}^E \mathbf{P}_B$. The moments generated by the cavitator, fins, and planing are:

$${}^B M_{y_c}(t) = -l_c F_{z_c}(t)$$

$${}^B M_{y_f}(t) = l_f F_{z_f}(t)$$

$${}^B M_{y_p}(t) = l_p F_{z_p}(t)$$

where l_c , l_f , and l_p are the distances from the vehicle center of mass to the centers of pressure at the cavitator, fin, and planing. l_p is assumed constant and applied at the vehicle back-end. As well, l_c and l_f are assumed constant and located at the cavitator and fin geometrical centers. Variations in the locations of the centers of pressure are neglected because they are significantly smaller than l_c , l_f , and l_p .

To assemble the nonlinear equations of motion, we use the forces at the cavitator, fins, planing regions, and gravity described in Section 4.4. The velocities and attack angles

at the cavitator and fins, needed to compute the forces, are:

$$\begin{aligned} {}^B\mathbf{V}_C(t) &= \begin{bmatrix} u(t) \\ w(t) - l_c q(t) \end{bmatrix} \\ \alpha_c(t) &= \tan^{-1} \left(\frac{w(t) - l_c q(t)}{u(t)} \right) + \delta_c(t) \\ {}^B\mathbf{V}_F(t) &= \begin{bmatrix} u(t) \\ w + l_f q(t) \end{bmatrix} \\ \alpha_f(t) &= \tan^{-1} \left(\frac{w(t) + l_f q(t)}{u(t)} \right) + \delta_f(t) \end{aligned}$$

The above equations assume that the velocity of the fluid with respect to the inertial frame is zero and therefore ${}^B\mathbf{V}_{C/f} = {}^B\mathbf{V}_C$ and ${}^B\mathbf{V}_{F/f} = {}^B\mathbf{V}_F$. The planing immersion $\lambda(t) = c_h h(t)$, used to calculate the planing forces, is determined by a computer algorithm during simulation. The algorithm computes the point ${}^E\mathbf{P}_{ij}^*$ along the supercavity that is the closest to the line segment connecting the edges of the vehicle body at the back-end denoted as \bar{B} . A line tangent to ${}^E\mathbf{P}_{ij}^*$, denoted as \bar{T} is computed as the line that connects ${}^E\mathbf{P}_{i-1,j}^*$ and ${}^E\mathbf{P}_{i+1,j}^*$. Then the algorithm calculates if \bar{T} intersects the segment \bar{B} . If so, the vehicle immersion is equal to the distance between the intersection point and its closest edge of the vehicle back-end.

4.6.2 Experimental 1-DOF Vehicle

The 1-DOF vehicle dynamics are:

$$I_{yy} \dot{q}(t) = -l_c {}^B F_{z_c}(t) + l_f {}^B F_{z_f}(t) + l_p {}^B F_{z_p}(t) + l_g {}^B F_{z_g}(t) + M_{\Delta}(t) \quad (4.19)$$

$$F_{x_r}(t) = {}^B F_{x_c}(t) + {}^B F_{x_f}(t) + {}^B F_{x_p}(t) + {}^B F_{x_g}(t) + {}^B F_{x_{\Delta}}(t) \quad (4.20)$$

$${}^B F_{z_r}(t) = {}^B F_{z_c}(t) + {}^B F_{z_f}(t) + {}^B F_{z_p}(t) + {}^B F_{z_g}(t) + {}^B F_{z_{\Delta}}(t) \quad (4.21)$$

$$\dot{\alpha}(t) = \dot{\theta}(t) = q(t) \quad (4.22)$$

I_{yy} is the vehicle moment of inertia about the rotary axis ${}^B\hat{\mathbf{y}}$; ${}^B F_{x_r}$ and ${}^B F_{z_r}$ are the reaction forces at the body (rotary) frame along ${}^B\hat{\mathbf{x}}$ and ${}^B\hat{\mathbf{z}}$ respectively; ${}^B F_{x_g}$ and ${}^B F_{z_g}$ are the forces due to the gravity; M_{Δ} , ${}^B F_{x_{\Delta}}$ and ${}^B F_{z_{\Delta}}$ are the moment and forces generated by the friction of the shaft, the induced lateral planing, and the interaction of the ventilation hoses with the fluid. The vehicle attack angle, denoted as α , is the angle between the water velocity vector and ${}^B\hat{\mathbf{x}}$. This angle is approximately equal to the pitch angle θ . Here l_c , l_f , and l_p are the distances from the rotary axis to the centers

of pressure at the cavitator, fins, and planing. l_g is distance from the rotary axis to the vehicle c.g. It is positive when the c.g. is behind the rotary axis, zero when the c.g. coincides with the rotary axis, and negative otherwise.

The location of the rotary axis is adjusted to modify the dynamics of the test system. Adjusting the location of the rotary axis changes l_c , l_f , l_p , and l_g . As l_p and l_f increase, l_c decreases. Moreover, when l_p is at its largest value, planing has the most authority to destabilize the vehicle.

To assemble the nonlinear equations of motion, we use the forces at the cavitator, fins, planing regions, and gravity described in Section 4.4. The velocities and attack angles at the cavitator and fins are given by:

$$\begin{aligned} {}^B\mathbf{V}_{\mathbf{C}/\mathbf{f}}(t) &= \begin{bmatrix} U_0 \cos(\alpha(t)) \\ U_0 \sin(\alpha(t)) - l_c q(t) \end{bmatrix} \\ \alpha_c(t) &= \tan^{-1} \left(\frac{U_0 \sin(\alpha(t)) - l_c q(t)}{U_0 \cos(\alpha(t))} \right) + \delta_c(t) \\ {}^B\mathbf{V}_{\mathbf{F}/\mathbf{f}}(t) &= \begin{bmatrix} U_0 \cos(\alpha(t)) \\ U_0 \sin(\alpha(t)) + l_f q(t) \end{bmatrix} \\ \alpha_f(t) &= \tan^{-1} \left(\frac{U_0 \sin(\alpha(t)) + l_f q(t)}{U_0 \cos(\alpha(t))} \right) + \delta_f(t) \end{aligned}$$

A schematic that summarizes the nonlinear dynamics of both 1-DOF and 3-DOF vehicles is presented in Figure 4.14.

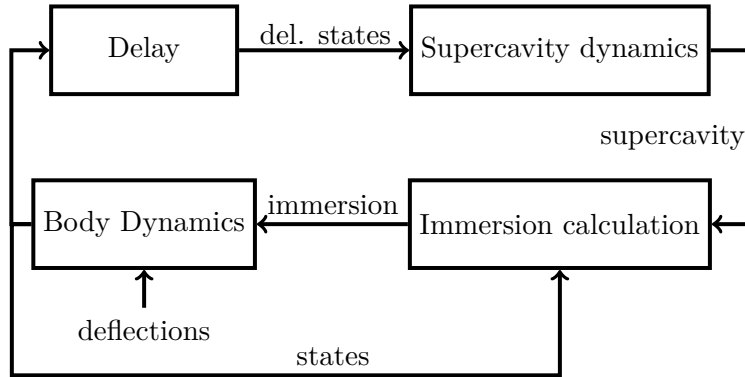


Figure 4.14: Schematic of full nonlinear dynamics

4.7 Flow Disturbances

Flow disturbances generated by waves in the proximity of the ocean surface affect the motion of supercavitating vehicles. The flow disturbances vary the height of the water column above the vehicle and therefore the pressure, cavitation number, and ultimately the supercavity geometry. The effect of flow perturbations on the supercavity geometry are illustrated by the experimental results of Section 4.5.5. Flow perturbations also vary the attack angle observed by the wetted regions of the vehicle body and thereby the hydrodynamic forces. In sum, flow perturbations have a direct effect on the supercavity geometry and hydrodynamic forces. Considering the effect of disturbances is relevant to evaluate the performance and robustness of control systems in face of realistic scenarios. We model flow disturbances by perturbing the vehicle attack angles α_c , α_f , and α_p as well as the supercavity parameters a_j and b_j .

4.8 Simplified Dynamic Model

A low-dimensional model of the vehicle dynamics is derived in this section. The model is a key contribution of this dissertation as it enables the development of robust control strategies using automated computational tools. Both 3-DOF and 1-DOF vehicles are characterized with low-order models of the same structure. The models are extended to describe the uncertainty due to the unmodeled planing dynamics.

4.8.1 Unconstrained 3-DOF Vehicle

Three ideas have inspired the simplified vehicle model. First, the nonlinear body dynamics are significantly simplified by approximating them about an equilibrium axial speed. Specifically, we consider the equilibrium condition at which the axial speed is $u = U_0$, the vehicle normal speed is $w = 0$, the pitch angle is $\theta = \Theta_0$, and the vehicle body is inside the supercavity. It is important to note that there are equilibrium (trim) points in the planing condition too. In such a case, the vehicle afterbody provides lift, but also induces drag. The second idea is that the planing immersion can be estimated by only considering the back-end section of the supercavity. The third idea is that planing behaves like a dead-zone operator. When the vehicle is inside the supercavity, in the dead-zone, the planing forces are zero. These forces become nonzero when the vehicle pierces the supercavity.

The vehicle dynamics are approximated about $u = U_0$. With small variations in axial

speed, the nonlinearity of stronger effect on the system dynamics is the switching between planing and non-planing states. Conditions of equilibrium for a vehicle traveling at $w = 0$, $u = U_0$, and $\theta = \Theta_0$ are:

$$\begin{aligned} {}^B F_{\tau_0} &\approx mg \sin(\theta_0) + \frac{1}{2} \rho U_0^2 A_c C_{CD} \cos^2(\delta_{c0}) + \frac{1}{2} \rho U_0^2 A_f a_{fd} \delta_{f0}^2 \\ \delta_{c0} &\approx -\frac{1}{2} \sin^{-1} \left(\frac{4l_f mg \cos(\theta_0)}{(l_f + l_c) \rho U_0^2 A_c C_{CD}} \right) \\ \delta_{f0} &\approx \frac{2l_c mg \cos(\theta_0)}{(l_f + l_c) \rho U_0^2 A_f a_{fl}} \end{aligned}$$

An approximation of the vehicle dynamics about equilibrium is given by:

$$\begin{aligned} \dot{\mathbf{x}}(t) &= \mathbf{A}\mathbf{x}(t) + \mathbf{B}_\delta \boldsymbol{\delta}(t) + \mathbf{B}_\lambda \lambda(t) \tag{4.23} \\ \mathbf{A} &= \begin{bmatrix} -\frac{1}{m} \rho A_c C_{CD} U_0 & 0 & -g \cos(\theta_0) & 0 & 0 \\ 0 & -\frac{1}{2m} \rho U_0 A_f a_{fl} & -g \sin(\theta_0) & U_0 - \frac{l_f}{2m} \rho U_0 A_f a_{fl} & 0 \\ 0 & 0 & 0 & 1 & 0 \\ 0 & -\frac{l_f}{2I_{yy}} \rho U_0 A_f a_{fl} & 0 & -\frac{l_f^2}{2I_{yy}} \rho U_0 A_f a_{fl} & 0 \\ 0 & 1 & -U_0 & -l_c & 0 \end{bmatrix} \\ [\mathbf{B}_\delta \mid \mathbf{B}_\lambda] &= \begin{bmatrix} 0 & 0 & 0 \\ \frac{1}{2m} \rho U_0^2 A_c C_{CD} & -\frac{1}{2m} \rho U_0^2 A_f a_{fl} & \frac{1}{2m} \rho U_0^2 D_{cyl} a_{pz} c_h \\ 0 & 0 & 0 \\ -\frac{l_c}{2I_{yy}} \rho U_0^2 A_c C_{CD} & -\frac{l_f}{2I_{yy}} \rho U_0^2 A_f a_{fl} & \frac{\bar{l}_p}{2I_{yy}} \rho U_0^2 D_{cyl} a_{pz} c_h \\ 0 & 0 & 0 \end{bmatrix} \end{aligned}$$

where $\mathbf{x} = [u \ w \ \theta \ q \ E_{zC}]$ is the state vector and E_{zC} is the cavitator position expressed in the inertial frame $\{E\}$. The approximation in Equation 4.23 is obtained assuming that the vehicle states are small perturbations about equilibrium.

To simplify the original equations of motion, the supercavity is assumed symmetric and the following approximations are made: $a = \frac{a_1 + a_2}{2}$, $n = \frac{b_1 + b_2}{2}$, and $\kappa = \frac{\kappa_1 + \kappa_2}{2}$. The planing immersion is $h(t) = c_h \lambda(t)$ and $\lambda(t)$ is the supercavity position with respect to the vehicle body at the transom. $\lambda(t)$ is calculated as:

$$\lambda(t) = \phi_0(z(t)) = \begin{cases} z(t) - \epsilon, & \text{if } z(t) > \epsilon \\ z(t) + \epsilon, & \text{if } z(t) < -\epsilon \\ 0 & \text{otherwise} \end{cases} \tag{4.24}$$

$$z(t) = E_{z_s}(t) - E_{z_b}(t) \quad (4.25)$$

$$E_{z_s}(t) = C_s \mathbf{x}(t - \Delta t) + D_s \delta_c(t - \Delta t) \quad (4.26)$$

$$E_{z_b}(t) = C_b \mathbf{x}(t) \quad (4.27)$$

$$\epsilon \approx \left| \frac{D_{cyl}}{2} - \left(\frac{D_c}{2} + b \left[1 - \left(\frac{L-a}{a} \right)^2 \right]^{1/\eta} \right) \right| \quad (4.28)$$

$$C_s = \begin{bmatrix} 0 & -\frac{\kappa L}{U_0} & 0 & \frac{\kappa L L_c}{U_0} & 1 \end{bmatrix}$$

$$C_b = \begin{bmatrix} 0 & 0 & L & 0 & 1 \end{bmatrix}$$

$$D_s = -\kappa L$$

where $z(t)$ is the relative position between the supercavity and body centers at the transom ($E_{z_s}(t)$ and $E_{z_b}(t)$). To obtain $\lambda(t)$, $z(t)$ is passed through the dead-zone operator $\phi_0(\cdot)$. Figure 4.15b illustrates how $z(t)$ and $\lambda(t)$ are computed. It is important to mention that the value of $\lambda(t)$ is bounded by $\bar{\lambda} = D_{cyl}/c_h$ because the immersion cannot be larger than the diameter of the body ($h \leq D_{cyl}$). The deadzone size, denoted as ϵ , is equal to the distance from the vehicle body to the supercavity edge when the supercavity and body centers are aligned. We assume that the cavitation number is kept constant by regulating the supercavity pressure p_c . See Equation 2.8. Consequently, the supercavity size and ϵ are assumed constant. The time delay due to the dependence of the supercavity geometry on previous cavitator states is $\Delta t \approx L/U_0$.

We obtain C_s and D_s by linearizing the position of the supercavity center at the back-end given by:

$$\begin{aligned} \mathbf{E} \hat{\mathbf{P}}_s(t) &= \begin{bmatrix} E_{x_s}(t) \\ E_{z_s}(t) \\ 1 \end{bmatrix} = \frac{1}{2} \left[\mathbf{E} \hat{\mathbf{P}}_{N2}(t) + \mathbf{E} \hat{\mathbf{P}}_{N1}(t) \right] \\ &= \frac{1}{2} \begin{bmatrix} E_T \\ B_T \\ C_T \end{bmatrix} \left[\begin{bmatrix} C_{N1} \\ T \end{bmatrix} \mathbf{N1} \hat{\mathbf{P}}_{N1}(t) + \begin{bmatrix} C_{N2} \\ T \end{bmatrix} \mathbf{N2} \hat{\mathbf{P}}_{N2}(t) \right] \end{aligned} \quad (4.29)$$

$\mathbf{N1} \hat{\mathbf{P}}_{N1}(t)$ and $\mathbf{N2} \hat{\mathbf{P}}_{N2}(t)$ are the locations of the supercavity edges at the back-end as expressed in the local frames $\{N1\}$ and $\{N2\}$, given by:

$$\mathbf{NJ} \hat{\mathbf{P}}_{NJ}(t) = \begin{bmatrix} x_{Nj}(t) \\ z_{Nj}(t) \end{bmatrix} = \begin{bmatrix} 0 \\ (-1)^j b \left[1 - \left(\frac{L-a}{a} \right)^2 \right]^{1/n} - \kappa L \alpha_c(t - \Delta t) \end{bmatrix}$$

After approximating Expression 4.29 by small angles, we obtain:

$$\mathbf{E}\hat{\mathbf{P}}_s = \begin{bmatrix} E_{x_s}(t) \\ E_{z_s}(t) \\ 1 \end{bmatrix} = \begin{bmatrix} E_{x_c}(t - \Delta t) \\ E_{z_c}(t - \Delta t) - \kappa L \alpha_c(t - \Delta t) \\ 1 \end{bmatrix},$$

which is then plugged into the state space Equation 4.26.

The fin immersion in the fluid b_f , needed to compute the fin area $A_f \approx b_f c_f$ is approximated by:

$$b_f \approx \bar{b}_f - \epsilon_f \tag{4.30}$$

$$\epsilon_f \approx \left| \frac{D_{cyl}}{2} - \left(\frac{D_c}{2} + b \left[1 - \left(\frac{l_c + l_f - a}{a} \right)^2 \right]^{1/\eta} \right) \right|$$

with \bar{b}_f being the full fin span.

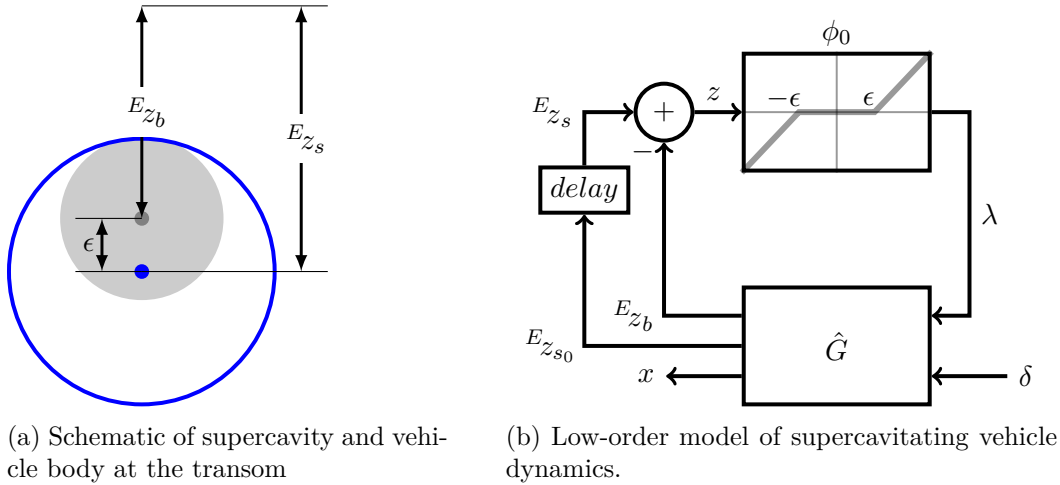


Figure 4.15: Schematics of vehicle dynamics described with a dead-zone

We validate that the simplified model of the 3-DOF vehicle dynamics provides reasonable accuracy with respect to the full nonlinear model. For doing this, the full nonlinear model from Equations 4.14-4.18 and simplified nonlinear model from Equations 4.23-4.28 were simulated with the same input. We simulated a hypothetical vehicle of the size of our test vehicle. The vehicle parameters are presented in Section 3.3. We assume the trim axial speed is $U_0=5$ m/s. A controller designed with linear design methods was used for the simulation. The controller commands the cavitator and fin deflections $\delta = \begin{bmatrix} \delta_c \\ \delta_f \end{bmatrix}$

to track pitch angle commands θ_r . Since we are primarily interested in demonstrating the accuracy of the simplified model with respect to the full nonlinear simulation, we do not provide details on the controller. A simulations in which step commands are applied to the pitch angle command are shown in Figure 4.16. The responses of both pitch angle and immersion for both models show excellent agreement. The simplified model is attractive for system analysis and control synthesis due to its low-order and accurate representation of the original nonlinear dynamics.

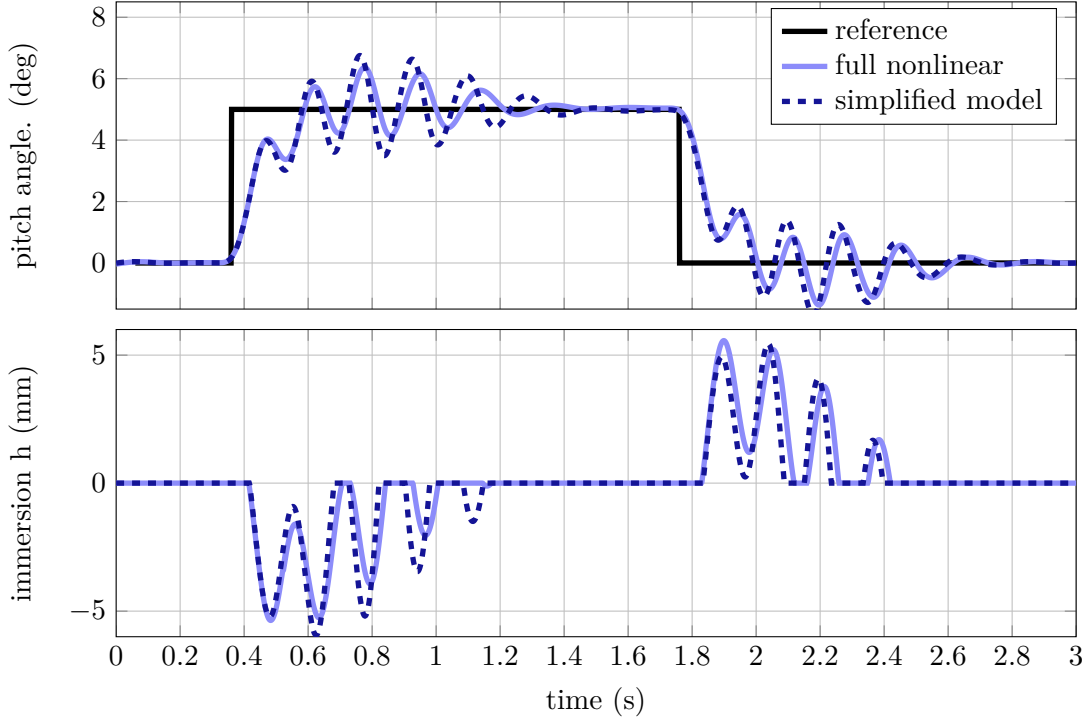


Figure 4.16: Comparison of full and simplified nonlinear models about $u = U_0$

4.8.2 Experimental 1-DOF Vehicle

The simplified equations of motion for the 1-DOF experimental vehicle are considered about the equilibrium point $[\alpha] = [0]$. For this equilibrium point, a trim condition of the fin deflection δ_{f0} , given the cavitator deflection δ_{c0} is:

$$\delta_{f0} \approx \frac{-M_{\Delta} - l_g mg + l_c \rho U_0^2 A_c C_{CD} \delta_{c0}}{0.5 \rho U_0^2 A_f a_{fl}}$$

The equations of motion are:

$$\dot{\mathbf{x}}(t) = A\mathbf{x}(t) + B_\delta\delta(t) + B_\lambda\lambda(t) \quad (4.31)$$

$$\lambda(t) = \phi_0(z(t)) = \begin{cases} z(t) - \epsilon, & \text{if } z(t) > \epsilon \\ z(t) + \epsilon, & \text{if } z(t) < -\epsilon \\ 0 & \text{otherwise} \end{cases} \quad (4.32)$$

$$z(t) = {}^E z_s(t) - {}^E z_b(t) \approx C_s x(t - \Delta t) + D_s \delta_c(t - \Delta t) - C_b x(t) \quad (4.33)$$

$$A = \begin{bmatrix} 0 & 1 \\ -\frac{l_f}{2I_{yy}}\rho U_0^2 A_f a_{fl} + \Delta_\alpha & -\frac{l_f^2}{2I_{yy}}\rho U_0 A_f a_{fl} + \Delta_q \end{bmatrix}$$

$$\left[B_\delta \mid B_\lambda \right] = \left[\begin{array}{cc|c} 0 & 0 & 0 \\ -\frac{l_c}{2I_{yy}}\rho U_0^2 A_c C_{CD} & -\frac{l_f}{2I_{yy}}\rho U_0^2 A_f a_{fl} & \frac{l_p}{2I_{yy}}\rho U_0^2 D_{cyl} a_{pz} c_h \end{array} \right],$$

$$C_s = \begin{bmatrix} -\kappa L - l_c & \frac{\kappa L l_c}{U_0} \end{bmatrix}$$

$$C_b = \begin{bmatrix} l_b & 0 \end{bmatrix}$$

$$D_s = -\kappa L$$

U_0 is the water tunnel speed. Δ_α and Δ_q describe the accelerations induced by lateral planing, friction in the rotary shaft, and interaction between the ventilation hoses with the fluid. These are unknown parameters that represent decelerations due to the moment M_Δ from Equation 4.19. Like in the 3-DOF case, the dead-zone size and fin span b_f (needed to compute A_f) are described by Equations 4.28 and 4.30.

We obtain C_s and D_s by linearizing the position of the supercavity center at the back-end given by

$$\begin{aligned} {}^E \hat{\mathbf{P}}_s(t) &= \begin{bmatrix} {}^E x_s(t) \\ {}^E z_s(t) \\ 1 \end{bmatrix} = \frac{1}{2} \left[{}^E \hat{\mathbf{P}}_{N2}(t) + {}^E \hat{\mathbf{P}}_{N1}(t) \right] \\ &= \frac{1}{2} \begin{bmatrix} E \\ B \end{bmatrix}^T \begin{bmatrix} B \\ C \end{bmatrix}^T \left[\begin{matrix} C \\ N1 \end{matrix} \right]^T {}^{N1} \hat{\mathbf{P}}_{N1}(t) + \begin{bmatrix} C \\ N2 \end{matrix} \right]^T {}^{N2} \hat{\mathbf{P}}_{N2}(t) \end{aligned} \quad (4.34)$$

${}^{N1} \hat{\mathbf{P}}_{N1}(t)$ and ${}^{N2} \hat{\mathbf{P}}_{N2}(t)$ are the locations of the supercavity edges at the back-end as

expressed in the local frames $\{N1\}$ and $\{N2\}$:

$${}^{\text{NJ}}\mathbf{P}_{\text{NJ}}(t) = \begin{bmatrix} x_{Nj}(t) \\ z_{Nj}(t) \end{bmatrix} = \begin{bmatrix} -L \\ (-1^j)b \left[1 - \left(\frac{L-a}{a} \right)^2 \right]^{1/n} - \kappa L \alpha_c(t - \Delta t) \end{bmatrix}$$

After approximating Expression 4.34 by small angles, we obtain:

$${}^{\text{E}}\hat{\mathbf{P}}_{\text{s}}(t) = \begin{bmatrix} E x_s(t) \\ E z_s(t) \\ 1 \end{bmatrix} = \begin{bmatrix} l_b \\ (-l_c - \kappa L)\alpha(t - \Delta t) - \kappa L \delta_c(t - \Delta t) + \frac{l_c \kappa L}{U_0} q(t - \Delta t) \\ 1 \end{bmatrix},$$

which is then plugged into the state space Equation 4.33.

The model presented in Equations 4.31, 4.32, and 4.33 helps us understand the qualitative dynamics of the system. However, Δ_α and Δ_q are difficult to model and may change from one experiment to another. To construct a numerical model of the vehicle in the tunnel, we employ system identification techniques. The experimental-based identification of the test vehicle is presented in Section 4.11.

4.8.3 Supercavity Delay

The delay $\Delta t \approx L/U_0$ is present in both 1+DOF and 3-DOF vehicle models. A first order approximation [25] of this delay is described by:

$$\begin{aligned} \dot{x}_d(t) &= -\frac{2}{\Delta t} x_d(t) + \frac{4}{\Delta t} z_{s_0}(t) \\ &= -\frac{2U_0}{L} x_d(t) + \frac{4U_0}{L} z_{s_0}(t) \\ z_s(t) &= x_d(t) - z_{s_0}(t) \end{aligned}$$

where $x_d(t)$ is the state of the time delay approximation; $z_{s_0}(t)$ and $z_s(t)$ are the input and output of the time delay operator. Using the time delay approximation and knowing that $z_{s_0}(t) = C_s x(t) + D_s \delta_c(t)$, we compute signal $z(t)$ of the 1-DOF and 3-DOF equations of motion as:

$$z(t) = -x_d(t) + C_s x(t) + D_s \delta_c(t) - z_b(t) = (C_s - C_b) x(t) - x_d(t) + D_s \delta_c(t)$$

4.9 Uncertainty

The main source of uncertainty in the dynamic models of both 1-DOF and 3-DOF vehicles is the imprecision in characterizing the complex interaction of the supercavity and vehicle. In particular, within the planing force model, the effects of planing angle α_p are not accounted for. As discussed in Section 4.4.5, the planing forces are assumed functions of immersion $h(t)$ at a constant planing angle α_p . However, not considering variations of α_p is imprecise. Therefore, the coefficient of normal planing force $a_{pz}(t)$ is treated as an uncertain parameter that lies in the range:

$$\underline{a}_{pz} \leq a_{pz}(t) \leq \bar{a}_{pz}$$

\bar{a}_{pz} and \underline{a}_{pz} are upper and lower bounds of a_{pz} . It is important to highlight that $a_{pz}(t)$ varies with time as $\alpha_p(t)$ does.

We also anticipate that our approach to reproduce the geometrical distortion of the supercavity in the planing region is inaccurate. In Section 4.5.6 we use the correction factor c_h to describe how the supercavity deforms due to its interaction with the vehicle afterbody. The immersion is computed as $h(t) = c_h \lambda(t)$. This is an inexact approximation to such a complex phenomenon. Hence, we assume c_h as an uncertain time varying parameter that lies in:

$$\bar{c}_h \leq c_h(t) \leq \underline{c}_h$$

Revisiting the motion equations of the 1-DOF and 3-DOF vehicles in Expressions 4.23-4.28 and 4.31-4.33, we can see that the uncertain terms a_{pz} and c_h are always multiplying each other and that $a_{pz}c_h$ appears only in matrix B_λ . The combined uncertainty due to the unmodeled α_p and c_h turn into the following condition:

$$\underline{a}_{pz}\underline{c}_h \leq a_{pz}(t)c_h(t) \leq \bar{a}_{pz}\bar{c}_h \tag{4.35}$$

Since the output of the dead-zone operator $\lambda(t)$ enters B_λ and multiplies all elements in which $a_{pz}c_h$ appears, we can move the uncertainty out of B_λ and put it into the dead-zone operator. The uncertainty of the vehicle dynamics described by condition

4.35 is equivalent to a time varying dead-zone with variable slope, described by:

$$\lambda(t) = \phi(z(t), t) = \begin{cases} m_z(t) [z(t) - \epsilon], & \text{if } z(t) > \epsilon \\ m_z(t) [z(t) + \epsilon], & \text{if } z(t) < -\epsilon \\ 0 & \text{otherwise} \end{cases} \quad (4.36)$$

$$m_z(t) \in \left[\frac{a_{pz}c_h}{\bar{a}_{pz}\bar{c}_h}, 1 \right] \quad (4.37)$$

$$a_{pz} = \bar{a}_{pz} \quad (4.38)$$

$$c_h = \bar{c}_h \quad (4.39)$$

The set of values that the dead-zone operator can yield when its slope is variable is illustrated in Figure 4.17 as a blue area. Our description of the uncertainty assumes

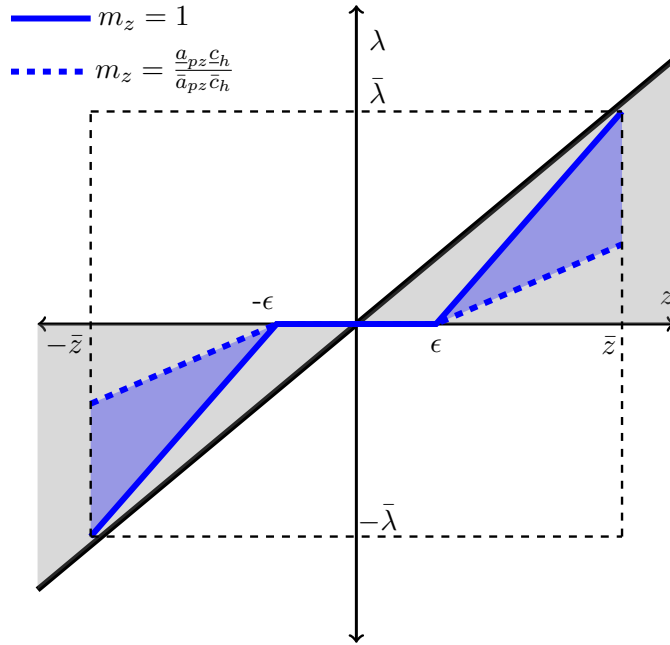


Figure 4.17: Schematic of dead-zone with variable slope

that the structure of the operator $\phi(z(t), t)$ that relates $z(t)$ with $\lambda(t)$ is *time varying* and *nonlinear*. Furthermore, the uncertainty region is bounded by $\lambda(t) \leq \bar{\lambda} = D_{cyl}/c_h$ and $z(t) \leq \bar{z} = \bar{\lambda} + \epsilon$. This is because the immersion must be less or equal than the diameter of the vehicle body D_{cyl} .

The set given by Expressions 4.36-4.39 is not easy to manipulate for stability analysis

and automated control synthesis. For this reason, we employ an outer approximation. The approximation is the region between two line segments with slopes 0 and r , referred to as sector $[0, r]$. This superset of the original uncertainty is depicted in Figure 4.17 as a gray area. The sector bound in gray is described by the graph $\Phi(z(t))$:

$$\lambda(t) \in \Phi(z(t)) = \{\phi : \phi \cdot [\phi - rz(t)] \leq 0\} \quad (4.40)$$

$$r = 1 - \epsilon/\bar{z}$$

This sector constraint is a quadratic inequality that can be easily integrated into automated tools for system analysis and control synthesis. It is worth mentioning that the sector bound allows us to have variations in the supercavity (ϵ) that may occur in practice. Despite its benefits, the sector contains regions that do not belong to the uncertainty set. Those regions introduce conservativeness in the system analysis and control design.

Typically, the Popov and Zames-Falb constraints [16, 31, 48] are used to include information about the time dependence, slope, and monotonicity of a nonlinearity. Both Popov and Zames-Falb constraints require $\phi(z(t), t)$ to be static. Since $\phi(z(t), t)$ is time varying we do not use such constraints with our model formulation. An alternative to possibly decrease conservatism in the uncertainty description, at the expense of complexity, is to consider the time varying uncertainty of $a_{pz}(t)c_h(t)$ and the static dead-zone $\phi_0(z(t))$ separately. In this way, Popov and Zames-Falb constraints could be added to more accurately describe $\phi_0(z(t))$.

The 1-DOF test vehicle is subject to lateral planing induced by the rotary shaft, as described in Section 3.6. Lateral planing damps out the vehicle motion and attenuates the effects of switching that an undersea vessel would otherwise exhibit. The lateral planing can be described via a nonlinear operator $\lambda(t) = \phi_0(z(t), t)$ for which the immersion $h(t) = c_h\lambda(t)$, between $-\epsilon$ and ϵ , is not necessarily zero. We hypothesize that $\phi_0(z(t), t)$ still belongs to the sector $[0, r]$ described by Expression 4.40 and drawn as a gray area in Figure 4.18. This assumption is reasonable since $\lambda(t) \not\leq 0$ whenever $z(t) \geq 0$ and $0 \not\leq \lambda(t)$ whenever $z(t) \leq 0$. Figure 4.18 illustrates a hypothetical case in which the curve of $\lambda(t) = \phi_0(z(t), t)$ between $-\epsilon$ and ϵ is linear. It is of highlight that our sector constraint bounds the uncertainty with or without lateral planing. This is very convenient to develop control design approaches that work for both 1-DOF and 3-DOF vehicles.

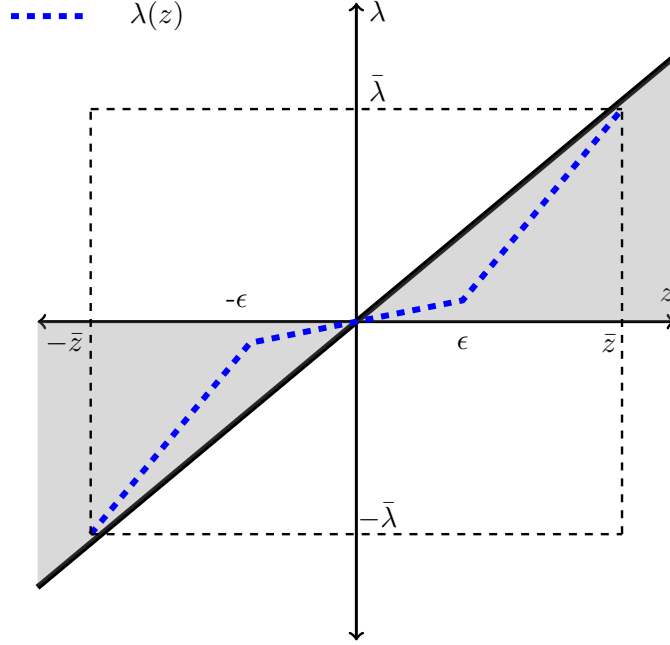


Figure 4.18: Schematic of nonlinear element for 1-DOF test vehicle

4.9.1 3-DOF Uncertain Dynamics

The uncertain dynamics of the 3-DOF vehicle is given by:

$$\dot{\mathbf{x}}(t) = A\mathbf{x}(t) + B_\delta\delta(t) + B_\lambda\lambda(t) \quad (4.41)$$

$$z(t) = C_z\mathbf{x}(t) + D_z\delta(t) \quad (4.42)$$

$$\lambda(t) \in \Phi(z(t)) = \{\phi : \phi \cdot [\phi - rz(t)] \leq 0\} \quad (4.43)$$

$A =$

$$\begin{bmatrix} -\frac{1}{m}\rho A_c C_{CD} U_0 & 0 & -g \cos(\theta_0) & 0 & 0 & 0 \\ 0 & -\frac{1}{2m}\rho U_0 A_f a_{fl} & -g \sin(\theta_0) & U_0 - \frac{l_f}{2m}\rho U_0 A_f a_{fl} & 0 & 0 \\ 0 & 0 & 0 & 1 & 0 & 0 \\ 0 & -\frac{l_f}{2I_{yy}}\rho U_0 A_f a_{fl} & 0 & -\frac{l_f^2}{2I_{yy}}\rho U_0 A_f a_{fl} & 0 & 0 \\ 0 & 1 & -U_0 & -l_c & 0 & 0 \\ 0 & -4\kappa & 0 & 4\kappa l_c & 4 & -\frac{2U_0}{L} \end{bmatrix}$$

$$\begin{aligned}
\left[B_\delta \mid B_h \right] &= \left[\begin{array}{cc|c} 0 & 0 & 0 \\ \frac{1}{2m}\rho U_0^2 A_c C_{CD} & -\frac{1}{2m}\rho U_0^2 A_f a_{fl} & \frac{1}{2m}\rho U_0^2 D_{cyl} a_{pz} c_h \\ 0 & 0 & 0 \\ -\frac{l_c}{2I_{yy}}\rho U_0^2 A_c C_{CD} & -\frac{l_f}{2I_{yy}}\rho U_0^2 A_f a_{fl} & \frac{\bar{l}_p}{2I_{yy}}\rho U_0^2 D_{cyl} a_{pz} c_h \\ 0 & 0 & 0 \\ -4U_0\kappa & 0 & 0 \end{array} \right] \\
C_z &= \left[0 \quad -\frac{\kappa L}{U_0} \quad -L \quad \frac{\kappa L l_c}{U_0} \quad 0 \quad -1 \right] \\
D_z &= \left[-\kappa L \quad 0 \right]
\end{aligned}$$

Note that we include the approximation to the time delay $\Delta t = L/U_0$ into the state space equations. The state vector becomes $x = [u \ w \ q \ \theta \ x_d]^T$ with x_d being the state of the time delay approximation.

4.9.2 1-DOF Uncertain Dynamics

The uncertain dynamics of the 1-DOF vehicle, with state vector $x = [\alpha \ q \ x_d]^T$, is given by:

$$\dot{\mathbf{x}}(t) = A\mathbf{x}(t) + B_\delta\delta(t) + B_\lambda\lambda(t) \quad (4.44)$$

$$z(t) = C_z\mathbf{x}(t) + D_z\delta(t) \quad (4.45)$$

$$\lambda(t) \in \Phi(z(t)) = \{\phi : \phi \cdot [\phi - rz(t)] \leq 0\} \quad (4.46)$$

$$\begin{aligned}
A &= \left[\begin{array}{ccc} 0 & 1 & 0 \\ -\frac{l_f}{2I_{yy}}\rho U_0^2 A_f a_{fl} + \Delta_\alpha & -\frac{l_f^2}{2I_{yy}}\rho U_0 A_f a_{fl} + \Delta_q & 0 \\ -4U_0(\kappa + 1) & 4\kappa l_c & -\frac{2U_0}{L} \end{array} \right] \\
\left[B_\delta \mid B_h \right] &= \left[\begin{array}{cc|c} 0 & 0 & 0 \\ -\frac{l_c}{2I_{yy}}\rho U_0^2 A_c C_{CD} & -\frac{l_f}{2I_{yy}}\rho U_0^2 A_f a_{fl} & \frac{l_p}{2I_{yy}}\rho U_0^2 D_{cyl} \bar{a}_{pz} \bar{c}_h \\ -4U_0\kappa & 0 & 0 \end{array} \right] \\
C_z &= \left[-L(\kappa + 1) \quad \frac{\kappa L l_c}{U_0} \quad -1 \right] \\
D_z &= \left[-\kappa L \quad 0 \right]
\end{aligned}$$

A graphical representation of the vehicle uncertain dynamics, which applies to both 1-DOF and 3-DOF vehicles, is presented in Figure 4.19. This uncertainty abstraction is used to synthesize controllers that are robust to uncertain and nonlinear planing forces.

Chapter 5 presents an approach to supercavitating vehicle control as well as experiments to validate the control scheme.

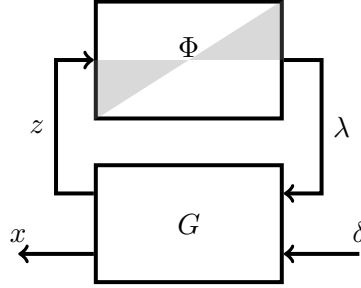


Figure 4.19: Schematic of the 1-DOF and 3-DOF uncertain vehicle dynamics

4.10 Actuator Dynamics

The cavitator and fins are driven by actuators with limited bandwidth. We assume that the actuation dynamics of the cavitator and fins are described by the following ordinary differential equations:

$$\begin{aligned}\dot{\mathbf{x}}_{\mathbf{c}}(t) &= A_c \mathbf{x}_{\mathbf{c}}(t) + B_c \delta_{c_r}(t) \\ \delta_c(t) &= C_c \mathbf{x}_{\mathbf{c}}(t) \\ \dot{\mathbf{x}}_{\mathbf{f}}(t) &= A_f \mathbf{x}_{\mathbf{f}}(t) + B_f \delta_{f_r}(t) \\ \delta_f(t) &= C_f \mathbf{x}_{\mathbf{f}}(t)\end{aligned}$$

δ_c and δ_f are the cavitator and fin deflections; δ_{c_r} and δ_{f_r} are the cavitator and fin reference commands; $\mathbf{x}_{\mathbf{c}}$ and $\mathbf{x}_{\mathbf{f}}$ are the state vectors of the cavitator and fin actuation systems. The actuation dynamics for both cavitator and fins in a compact form are given by:

$$\begin{aligned}\dot{\mathbf{x}}_{\delta}(t) &= A_{\delta} \mathbf{x}_{\delta}(t) + B_{\delta} \mathbf{u}(t) \\ \delta(t) &= \begin{bmatrix} \delta_c(t) \\ \delta_f(t) \end{bmatrix} = C_{\delta} \mathbf{x}_{\delta}(t) \\ \mathbf{x}_{\delta}(t) &= \begin{bmatrix} x_c(t) \\ x_f(t) \end{bmatrix}\end{aligned}$$

$$\mathbf{u}(t) = \begin{bmatrix} \delta_{c_r}(t) \\ \delta_{f_r}(t) \end{bmatrix}$$

$$A_\delta = \begin{bmatrix} A_c & 0 \\ 0 & A_f \end{bmatrix}$$

$$B_\delta = \begin{bmatrix} B_c & 0 \\ 0 & B_f \end{bmatrix}$$

$$C_\delta = \begin{bmatrix} C_c & 0 \\ 0 & C_f \end{bmatrix}$$

4.11 Model Identification 1-DOF

The model of the 1-DOF vehicle dynamics for system identification is described by:

$$\dot{\mathbf{x}}(t) = A\mathbf{x}(t) + B_\delta\delta(t) + B_\lambda\lambda(t) \quad (4.47)$$

$$\lambda(t) \in \Phi(z(t)) = \{\phi : \phi \cdot [\phi - rz(t)] \leq 0\} \quad (4.48)$$

$$z(t) = E_{z_s}(t) - E_{z_b}(t) \approx C_s\mathbf{x}(t - \Delta t) + D_s\delta_c(t - \Delta t) - C_b\mathbf{x}(t) \quad (4.49)$$

$$y(t) = C_y\mathbf{x}(t) \quad (4.50)$$

$$A = \begin{bmatrix} 0 & 1 \\ -\frac{l_f}{2I_{yy}}\rho U_0^2 A_f a_{fl} + \Delta_\alpha & -\frac{l_f^2}{2I_{yy}}\rho U_0 A_f a_{fl} + \Delta_q \end{bmatrix} = \begin{bmatrix} 0 & 1 \\ A_{21} & A_{22} \end{bmatrix}$$

$$B_\delta = \begin{bmatrix} 0 & 0 \\ -\frac{l_c}{2I_{yy}}\rho U_0^2 A_c C_{CD} & -\frac{l_f}{2I_{yy}}\rho U_0^2 A_f a_{fl} \end{bmatrix} = \begin{bmatrix} 0 & 0 \\ B_{\delta 21} & B_{\delta 22} \end{bmatrix}$$

$$B_\lambda = \begin{bmatrix} 0 \\ \frac{l_p}{2I_{yy}}\rho U_0^2 D_{cyl} \bar{a}_{pz} \bar{c}_h \end{bmatrix}$$

$$C_s = \begin{bmatrix} -\kappa L - l_c & \frac{\kappa L l_c}{U_0} \end{bmatrix}$$

$$C_b = \begin{bmatrix} l_b & 0 \end{bmatrix}$$

$$D_s = -\kappa L$$

$$C_y = \begin{bmatrix} 1 & 0 \end{bmatrix}$$

The accelerations induced by the lateral planing, ventilation hoses, and friction of the rotary shaft, represented by Δ_α and Δ_q are difficult to characterize accurately. Consequently, we do not have numerical values of A from an analytical model. To obtain

a full numerical model, we carry out a data-based identification of the system. The identification estimates A , B_{δ_c} , B_{δ_f} from experimental data. These estimations and the known dynamics related to planing given by B_λ , C_s , and D_s are then integrated into the full, nonlinear, uncertain model of the test vehicle.

Figure 4.20 depicts the system interconnection to be characterized. For small perturbations \mathbf{u} that keep z small, $\lambda \approx 0$ and planing forces are not generated. Without planing, the system behavior is approximately linear. Our interest is in identifying the linear system \hat{G} . Specifically, we want to characterize the input-output relationship between the control surface deflections δ and the attack angle measurement $y = \alpha$. A limitation is that the servo-actuators we use do not provide measurements of δ . We know however a model of the servo-actuators Act derived in [10] via system identification. The dynamical model of both the cavitator and fin actuators is given by:

$$\begin{aligned}\dot{x}_{c/f}(t) &= -30x_{c/f}(t) + 30\delta_{c/f_r}(t) \\ \delta_{c/f}(t) &= x_{c/f}(t),\end{aligned}$$

Given $\mathbf{u} = \begin{bmatrix} \delta_{c_r} \\ \delta_{f_r} \end{bmatrix}$, we can estimate the deflection $\delta = \begin{bmatrix} \delta_c \\ \delta_f \end{bmatrix}$ by simulating this model. The dynamic relation from δ to y is then identified using experimental data and system identification tools. We reconstruct \hat{G} by integrating the identified dynamics and the supercavity and planing force models. Then \hat{G} is connected with the uncertain element Φ and the time delay due to the supercavity dynamics (*delay* in Figure 4.20). Specifically,

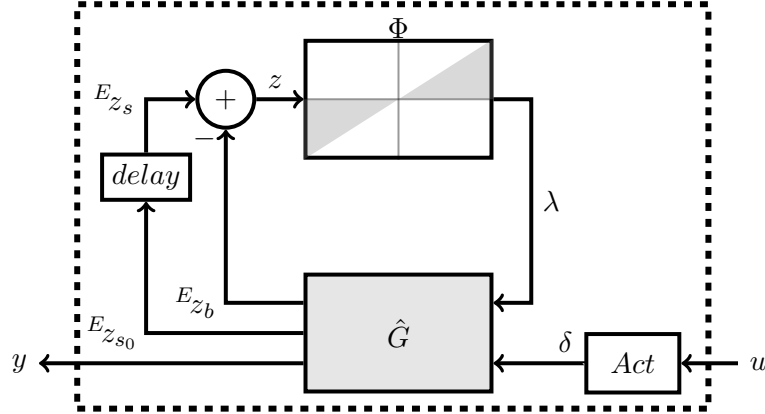


Figure 4.20: Schematic of unknown dynamics for system identification

we construct the uncertain nonlinear dynamics in two steps. First, we obtain matrices A and B_δ via system identification. Next, we construct B_λ , C_s , C_b , and *delay* using the planing force and supercavity models. The parameters of B_λ are obtained from an

estimation of the vehicle inertia I_{yy} and the planing force models described in Section 4.4.5. The dead-zone ϵ is computed via the supercavity model. C_s and D_s are computed using the dimensions of the vehicle and parameter κ related to the supercavity model.

4.11.1 Experiments

We carried out experiments to identify the dynamic relation between the control surface deflections δ and the attack angle measurement y as depicted in Figure 4.20. The conditions for the experiments are:

1. Fluid speed: $U_0 = 5.5$ m/s was selected because at this speed the control surfaces have enough effectiveness and the test system exhibits tolerable vibrations.
2. Ventilation flow rate: 60 liters per minute is selected to achieve a clear supercavity.
3. Position of the rotary axis: It is placed in the front-most side of the slit plate to allow for the largest planing moments. This is indeed the worst case scenario that we consider to challenge the control designs.

We apply stimuli to the system via cavitator and fin deflections in two separated experiments. In both cases, the inputs are square pulses with 50% duty cycle, 4 deg. amplitude, and frequencies between 0.5 and 10 Hz. When the cavitator commands are applied, the system we identify is given by:

$$\begin{aligned}\dot{\mathbf{x}} &= A\mathbf{x} + B_{\delta_c}\delta_c \\ y &= C_y\mathbf{x},\end{aligned}$$

where matrices A and B_{δ_c} are unknown and C_y is known. When the fin commands are applied, the system we identify is given by:

$$\begin{aligned}\dot{\mathbf{x}} &= A\mathbf{x} + B_{\delta_f}\delta_f \\ y &= C_y\mathbf{x},\end{aligned}$$

being matrices A and B_{δ_f} unknown.

The identification of the above systems was conducted using the MATLAB System Identification Toolbox [20] with the instrumental variable method described in [19, p. 311].

4.11.2 Results

The values of A obtained independently through the cavitator and fin perturbations are averaged to compute a final representation of A . The Bode plots of the systems obtained with the cavitator and fin deflections as well as their average are presented in Figure 4.21. Note that the systems are normalized with respect to their zero frequency gain. Matrices B_{δ_c} and B_{δ_f} from the identification routines are used to form $B_\delta = \begin{bmatrix} B_{\delta_c} & B_{\delta_f} \end{bmatrix}$.

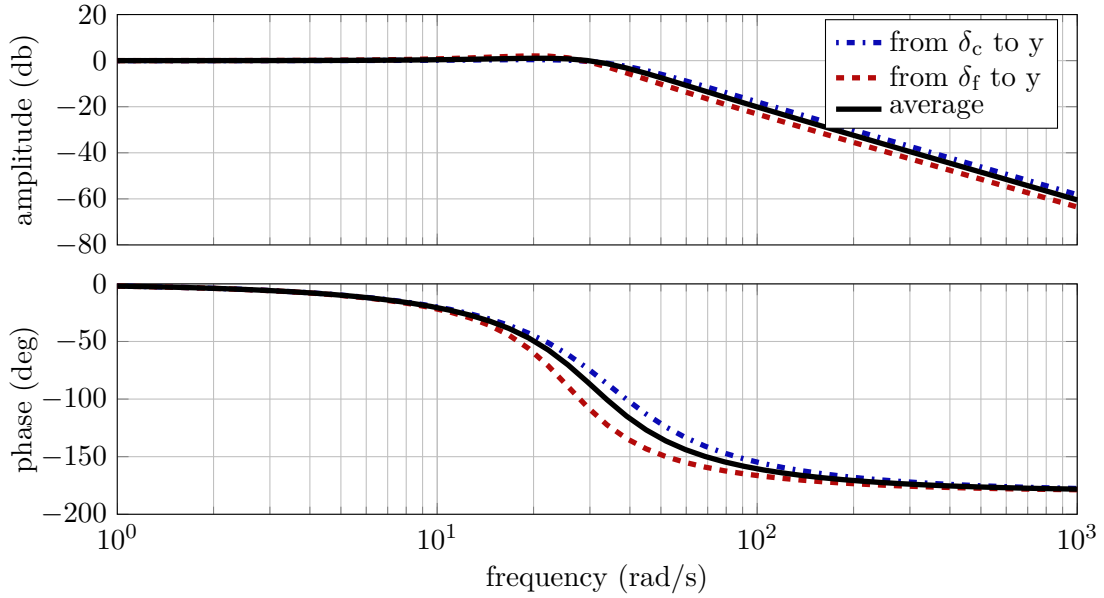


Figure 4.21: Bode plots of systems from identification, normalized with respect to the gain at zero frequency

The numerical values of our identification are as follows:

$$A = \begin{bmatrix} 0 & 1 \\ -949 & -32 \end{bmatrix}$$

$$B_\delta = \begin{bmatrix} B_{\delta_c} & | & B_{\delta_f} \end{bmatrix} = \begin{bmatrix} 0 & | & 0 \\ -220 & | & -174 \end{bmatrix}$$

The other parameters needed to construct the full nonlinear uncertain model are:

$$\bar{a}_{pz} = 0.3$$

$$\bar{c}_h = 2$$

$$D_{cyl} = 0.05 \text{ m}$$

$$\begin{aligned}
\epsilon &= 0.008 \text{ m} \\
\kappa &= 0.15 \\
I_{yy} &= 7.4e-4 \text{ Kg m}^2 \\
L &= 0.17 \text{ m} \\
l_p &= L - l_c = 0.07 \text{ m} \\
U_0 &= 5.5 \text{ m/s} \\
B_\lambda &= \begin{bmatrix} 0 \\ 2.67e4 \end{bmatrix} \\
\bar{z} &= D_{cyl}/\bar{c}_h + \epsilon = 0.047 \\
r &= 1 - \epsilon/\bar{z} = 0.62
\end{aligned}$$

Using r we construct the abstraction of the uncertain vehicle dynamics described by Φ . In Figure 4.22 we illustrate how the identified dynamics behave in closed-loop with simultaneous deflections of the cavitator and fins. In this figure, we compare a simulation of the identified linear dynamics with $\lambda(t) = \Phi(z(t), t) = 0$ and the actual dynamics from an experiment subject to planing and non-planing conditions. From top to bottom we have the vehicle attack angle α , the cavitator command δ_{c_r} , and the fin command δ_{f_r} . The data in Figure 4.22 corresponds to the case in which the vehicle dynamics is interconnected with a controller K_∞ , described in Chapter 5. The simulated linear system accurately represents the actual behavior of the test vehicle in the linear region. However, when the vehicle is subject to planing ($\alpha \rightarrow 4 \text{ deg}$), its behavior diverges from that of the linear simulation. This divergence indicates that $\Phi(z(t), t)$ plays a pivotal role in the vehicle dynamics during planing. Indeed, the open-loop system exhibits oscillations as shown in Section 3.6.

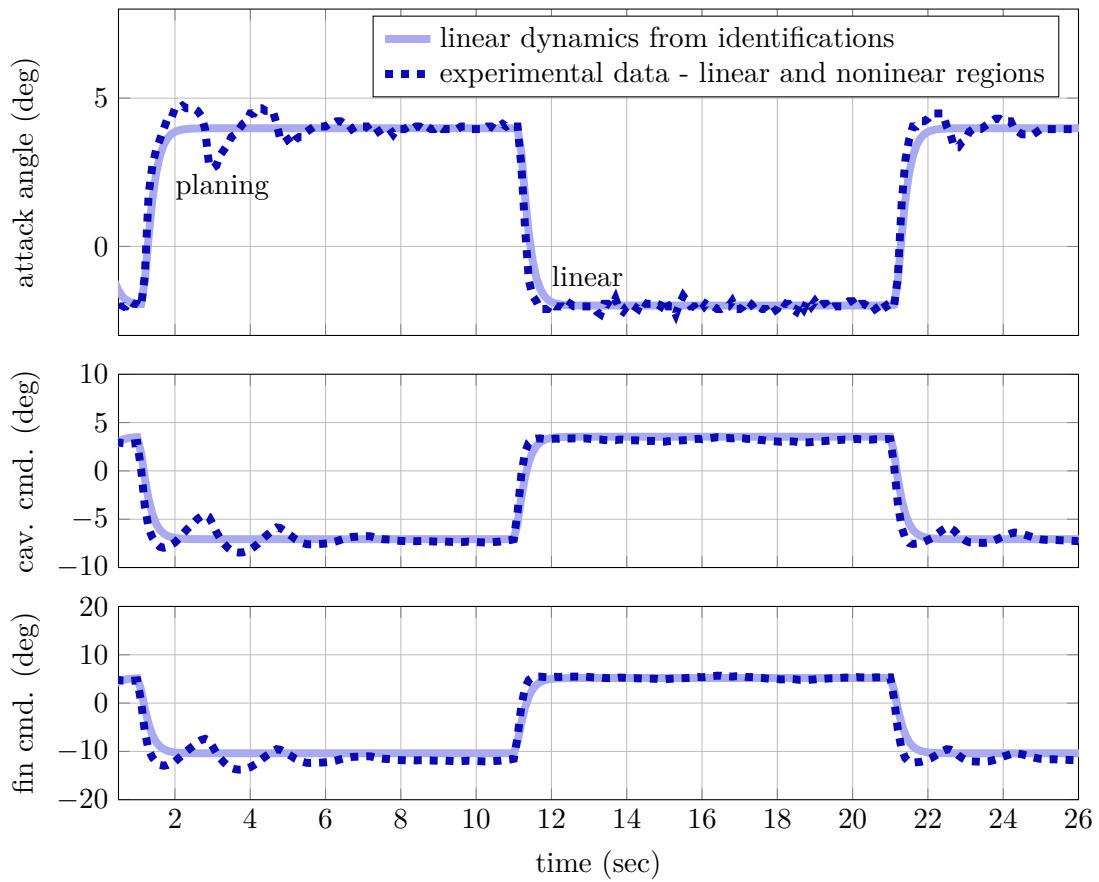


Figure 4.22: Linear dynamics from identification ($\lambda(t) = \Phi(z(t)) = 0, \forall t$) and nonlinear dynamics from experiment ($\lambda(t) \in \Phi(z(t))$)

Chapter 5

Control Synthesis and Validation

In this chapter, we develop and validate robust control strategies of a supercavitating vehicle. The ultimate goal of the controllers is to track commands accurately, minimize actuation, and guarantee performance in the face of nonlinear and uncertain planing forces. We employ the simplified abstraction of the vehicle dynamics presented in Chapter 4 to construct automated tools for robust control synthesis. Using these tools, we design control algorithms for the small scale supercavitating vehicle presented in Chapter 3. The benefit of the proposed control systems is demonstrated via experiments in the SAFL high-speed water tunnel.

5.1 Related Work

Several strategies have been proposed for the control of the benchmark vehicle model in [9]. The investigations in [2, 9, 26, 41] use nonlinear inversion, sliding mode control, and linear parameter varying (LPV) techniques to control the dynamics of a supercavitating vehicle traveling at a fixed axial speed. These strategies heavily rely on idealized models of the supercavity to estimate planing forces and schedule the controllers. Since the models are imprecise and the effect of uncertainty in the planing forces is not rigorously assessed, the controllers may lead to unpredictable performance in practice.

Validating control systems under uncertainty in the supercavitating vehicle dynamics has been typically done via numerical simulations [2, 26]. However, these simulations do not guarantee stability and performance in all the scenarios. Synthesis methods that certify stability and performance of a control system, given an uncertainty model of the

vehicle, are lacking. Such a formal method would provide a guarantee of performance under all the uncertain conditions, given that they are captured within the mathematical model.

On the other hand, there is a lack of affordable methods to validate control systems experimentally. Experiments are critical to evaluate the vehicle models and control schemes under realistic flow conditions, possibly not fully captured within a mathematical framework. In particular, experiments in a laboratory environment help identify pitfalls in the mathematical vehicle models and control schemes before undersea testing.

5.2 Problem Formulation

In this chapter we address two problems:

1. developing control synthesis tools that proof stability and performance for the closed-loop uncertain dynamics of a supercavitating vehicle, and
2. experimentally validating the control schemes subject to realistic flow conditions and nonlinear planing phenomena

5.2.1 Synthesis

Our first problem in its simpler form is to develop automated tools for synthesizing controllers for the uncertain nonlinear dynamics of a supercavitating vehicle. The vehicle model is described in Section 4.9 and depicted in Figure 5.1. The structure of this model is valid for both 3-DOF and 1-DOF vehicles. Here, we assume G includes the vehicle and actuation dynamics.

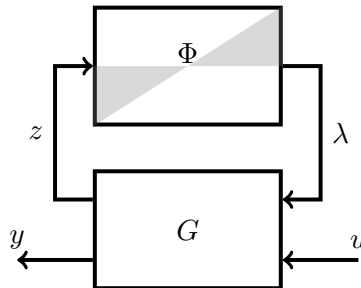


Figure 5.1: Uncertain system abstraction for control

The control synthesis tools we seek have the following characteristics:

1. **Multi-objective:** Suited for tracking, disturbance rejection, and minimization of actuation effort.
2. **Output feedback:** The control systems receive the sensor measurements y . Using measurements instead of full state information bypass the design of state observers.
3. **No measurements of z or λ :** Neither z nor λ are needed by the control system. This is helpful given that measuring these variables with accuracy is challenging and probably not necessary.
4. **Robust:** The controllers are robust to the nonlinear, time varying, uncertainty $\lambda(t) \in \Phi(z(t))$ as described by Equation 4.40. In addition, the synthesis tools deliver a mathematical proof of performance for all the uncertain conditions described by the model.
5. **Multi-input multi-output:** The controller may receive multiple measurements and may use both cavitator and fins for control.
6. **Linear time invariant:** This is the simplest control structure for both analysis and implementation. Hence, these controllers could be a baseline to compare with more sophisticated schemes.

5.2.2 Experimental Validation

The second problem we address in this chapter is to evaluate experimentally if the control strategies we develop provide an actual benefit over traditional control techniques that do not consider the uncertain planing dynamics.

5.3 Model

The stability and performance of the system structure under consideration are studied assuming that an LTI, multi-input, multi-output controller K is connected to the vehicle dynamics as in Figure 5.2. The generalized plant \bar{P} is the interconnection of the vehicle and actuator dynamics G as well as dynamic weights that normalize and quantify the system performance. $u \in \mathbb{R}^{n_u}$ and $y \in \mathbb{R}^{n_y}$ are the input to and output of the plant. The generalized disturbance $d \in \mathbb{R}^{n_d}$ consists of measurement noise, disturbances, and reference commands. $e \in \mathbb{R}^{n_e}$ is the generalized error, used for performance assessment, that consists of the tracking error and actuation effort. The input to and output of the

nonlinear, time varying uncertainty $\Phi(t)$ are $z \in \mathbb{R}^{n_z}$ and $\lambda \in \mathbb{R}^{n_\lambda}$ respectively. We consider only one nonlinear element in the system and therefore $n_z = 1$.

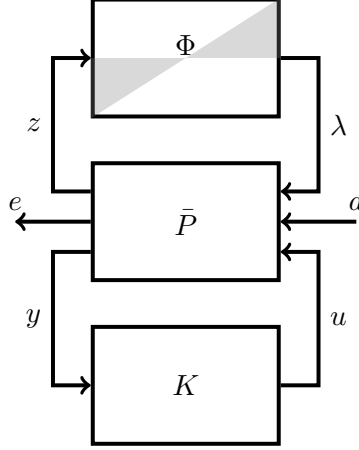


Figure 5.2: Closed-loop generalized plant with nonlinear element Φ

The state space equations of the generalized plant \bar{P} are given by:

$$\begin{bmatrix} \dot{x}(t) \\ z(t) \\ e(t) \\ y(t) \end{bmatrix} = \begin{bmatrix} A & B_\lambda & B_d & B_u \\ C_z & D_{z\lambda} & D_{zd} & D_{zu} \\ C_e & D_{e\lambda} & D_{ed} & D_{eu} \\ C_y & D_{y\lambda} & D_{yd} & D_{yu} \end{bmatrix} \begin{bmatrix} x(t) \\ \lambda(t) \\ d(t) \\ u(t) \end{bmatrix}$$

For well posedness of the interconnection, we assume $D_{z\lambda} = D_{yu} = 0$. We also assume that $D_{zd} = D_{zu} = 0$ for simplicity in deriving stability conditions of the system. The time-varying, variable slope, dead-zone operator that transforms $z(t)$ to $\lambda(t)$ is described by:

$$\lambda(t) \in \Phi(z(t)) = \{\phi : \phi \cdot [\phi - rz(t)] \leq 0\}$$

The controller state equations are given by:

$$\begin{bmatrix} \dot{x}_K(t) \\ u(t) \end{bmatrix} = \begin{bmatrix} A_K & B_K \\ C_K & D_K \end{bmatrix} \begin{bmatrix} x_K(t) \\ y(t) \end{bmatrix}$$

The interconnection of plant \bar{P} , controller K , and nonlinear uncertainty Φ is described

by:

$$\begin{bmatrix} \dot{\bar{x}}(t) \\ z(t) \\ e(t) \end{bmatrix} = \begin{bmatrix} \bar{A} & \bar{B}_\lambda & \bar{B}_d \\ \bar{C}_z & \bar{D}_{z\lambda} & \bar{D}_{zd} \\ \bar{C}_e & \bar{D}_{e\lambda} & \bar{D}_{ed} \end{bmatrix} \begin{bmatrix} \bar{x}(t) \\ \lambda(t) \\ d(t) \end{bmatrix} \quad (5.1)$$

$$\lambda(t) \in \Phi(z(t)) = \{\phi : \phi \cdot [\phi - rz(t)] \leq 0\} \quad (5.2)$$

$$\bar{A} = \begin{bmatrix} A + B_u D_c C_y & B_u C_k \\ B_k C_y & A_k \end{bmatrix}$$

$$\bar{B}_\lambda = \begin{bmatrix} B_\lambda + B_u D_k D_{y\lambda} \\ B_k D_{y\lambda} \end{bmatrix}$$

$$\bar{B}_d = \begin{bmatrix} B_d + B_u D_k D_{yd} \\ B_k D_{yd} \end{bmatrix}$$

$$\bar{C}_z = [C_z \quad 0]$$

$$\bar{D}_{z\lambda} = 0$$

$$\bar{D}_{zd} = 0$$

$$\bar{C}_e = [C_e + D_{eu} D_k C_y \quad D_{eu} C_k]$$

$$\bar{D}_{e\lambda} = D_{e\lambda} + D_{eu} D_k D_{y\lambda}$$

$$\bar{D}_{ed} = D_{ed} + D_{eu} D_k D_{yd}$$

where $\bar{x}(t) = [x(t) \quad x_K(t)]^T$ is the state vector of the interconnection.

The sector condition in Expression 5.2 is equivalent to the following quadratic constraint:

$$\begin{bmatrix} \bar{x}(t) \\ \lambda(t) \end{bmatrix}^T \begin{bmatrix} 0 & -rC_z^T \\ -rC_z & 2 \end{bmatrix} \begin{bmatrix} \bar{x}(t) \\ \lambda(t) \end{bmatrix} \leq 0 \quad (5.3)$$

It is important to recall here that constraints for better describing $\phi(z(t))$, based on Popov and Zames-Falb multipliers, cannot be applied to our system abstraction. This is because $\phi(z(t), t) \in \Phi(z(t))$ is time varying.

The stability and performance of the system abstraction described by Expressions 5.1 and 5.3 are analyzed in the following sections using simple, yet rigorous approaches.

5.4 Stability

Analysis tools based on passivity and absolute stability theory [16] have been adapted herein to establish global stability properties of the system under consideration. The global stability condition for the system described by Equations 5.1 and 5.3 for $\phi(z(t), t) \in \Phi(z(t)) = [0, r]$ is given in the following lemma.

Lemma 4. *Let us consider the system described by Expressions 5.1 and 5.3, with $d = 0$, $\phi(z(t), t) \in \Phi(z(t)) = [0, r]$ and whose transfer function from $\lambda(t)$ to $z(t)$ denoted as $-H(j\omega)$ is stable. The interconnection of $-H$ and Φ is globally asymptotically stable if $1 + rH(j\omega)$ is positive real: $\text{Re}(1 + rH(j\omega)) > 0, \forall \omega$. The proof of this stability criterion, given in [31, p. 240], is constructed using a quadratic Lyapunov function of the form $V(\bar{x}(t)) = \bar{x}(t)^T P \bar{x}(t)$, where $P \in \mathbb{S}_{++}^{n \times n}$*

Lemma 4 has a useful interpretation in the frequency domain. If $-1/r$ is the leftmost point along the real axis in the Nyquist plot of $H(j\omega)$, then the system is globally asymptotically stable for a time varying nonlinearity in sector $[0, r]$. We revisit this graphical interpretation to analyze the stability of controller designs in Section 5.9.

As for the proof of the circle criterion, we also employ quadratic functions to prove the global stability of the system described by Equations 5.1 and 5.3. This system is globally asymptotically stable if the sector constraint 5.3 holds and if there exists a symmetric matrix P that satisfies the following inequalities:

$$V(\bar{x}) = \bar{x}^T P \bar{x} > 0, \forall \bar{x} \neq 0 \quad (5.4)$$

$$\begin{aligned} \dot{V}(\bar{x}) &= \bar{x}^T (\bar{A}^T P + P \bar{A}) \bar{x} + 2\bar{x} P \bar{B}_\lambda \lambda \\ &= \begin{bmatrix} \bar{x} \\ \lambda \end{bmatrix}^T \begin{bmatrix} \bar{A}^T P + P \bar{A} & P \bar{B}_\lambda \\ \bar{B}_\lambda^T P & 0 \end{bmatrix} \begin{bmatrix} \bar{x} \\ \lambda \end{bmatrix} < 0, \forall \begin{bmatrix} \bar{x} \\ \lambda \end{bmatrix} \neq 0 \end{aligned} \quad (5.5)$$

Now on, the time dependence of all variables is dropped to simplify the presentation of formulas. The quadratic inequalities from the sector constraint 5.3 and Lyapunov stability conditions 5.4 and 5.5 are integrated via the S-procedure (Appendix A) by introducing an additional slack variable $0 < \tau \in \mathbb{R}$. Then the system is stable if there

exists P , τ such that the following Linear Matrix Inequalities (LMIs) hold:

$$P \succ 0 \quad (5.6)$$

$$\begin{bmatrix} \bar{A}^T P + P \bar{A} & P \bar{B}_\lambda + \tau r \bar{C}_z^T \\ \bar{B}_\lambda^T P + \tau r \bar{C}_z & -2\tau \end{bmatrix} \prec 0 \quad (5.7)$$

P and τ that satisfy 5.6-5.7 can be found by solving an LMI feasibility problem. See Appendix A for details on LMIs.

5.5 Performance

The performance of the closed-loop system described by Expressions 5.1 and 5.3 is quantified using the \mathcal{L}_2 to \mathcal{L}_2 induced gain from input disturbances to output errors. Recall from Section 2.5 that for a nonlinear system given by Expressions 5.1 and 5.3, there is a function $V(x) > 0$, $\forall \bar{x} \neq 0$ that satisfies:

$$\dot{V}(\bar{x}(t)) \leq \gamma^2 d(t)^T d(t) - e(t)^T e(t)$$

then the induced \mathcal{L}_2 gain of the system is not greater than γ . If we consider a quadratic Lyapunov function $V(x) = \bar{x}^T P \bar{x}$ with $P \succ 0$, the upper bound of the system induced norm γ is given by conditions 5.3 and:

$$\begin{aligned} & \left(\bar{A} \bar{x} + \begin{bmatrix} \bar{B}_\lambda & \bar{B}_d \end{bmatrix} \begin{bmatrix} \lambda \\ d \end{bmatrix} \right)^T P \bar{x} + \bar{x}^T P \left(\bar{A} \bar{x} + \begin{bmatrix} \bar{B}_\lambda & \bar{B}_d \end{bmatrix} \begin{bmatrix} \lambda \\ d \end{bmatrix} \right) \\ & \leq \gamma^2 d^T d - \left(\bar{C}_e \bar{x} + \bar{D}_{e\lambda} \lambda \right)^T \left(\bar{C}_e \bar{x} + \bar{D}_{e\lambda} \lambda \right) \end{aligned} \quad (5.8)$$

Condition 5.8 is equivalent to the following quadratic constraint:

$$\begin{bmatrix} \bar{x} \\ \lambda \\ d \end{bmatrix}^T \begin{bmatrix} \bar{A}^T P + P \bar{A} + \bar{C}_e^T \bar{C}_e & P \bar{B}_\lambda + \bar{C}_e^T \bar{D}_{e\lambda} & P \bar{B}_d + \bar{C}_e^T \bar{D}_{ed} \\ \bar{B}_\lambda^T P + \bar{D}_{e\lambda}^T \bar{C}_e & 0 & 0 \\ \bar{B}_d^T P + \bar{D}_{ed}^T \bar{C}_e & 0 & -\gamma^2 I + \bar{D}_{ed}^T \bar{D}_{ed} \end{bmatrix} \begin{bmatrix} \bar{x} \\ \lambda \\ d \end{bmatrix} \leq 0 \quad (5.9)$$

Putting together the sector condition 5.3 and induce \mathcal{L}_2 gain condition 5.9 via the S-procedure, we obtain:

$$\begin{bmatrix} \bar{x} \\ \lambda \\ d \end{bmatrix}^T \begin{bmatrix} \bar{A}^T P + P\bar{A} + \bar{C}_e^T \bar{C}_e & P\bar{B}_\lambda + \bar{C}_e^T \bar{D}_{e\lambda} + \tau r \bar{C}_z^T & P\bar{B}_d + \bar{C}_e^T \bar{D}_{ed} \\ \bar{B}_\lambda^T P + \bar{D}_{e\lambda}^T \bar{C}_e + \tau r \bar{C}_z & -2\tau & 0 \\ \bar{B}_d^T P + \bar{D}_{e\lambda}^T \bar{C}_e & 0 & -\gamma^2 I + \bar{D}_{ed}^T \bar{D}_{ed} \end{bmatrix} \begin{bmatrix} \bar{x} \\ \lambda \\ d \end{bmatrix} \leq 0$$

Using the Schur complement twice (Appendix A) the following condition is obtained:

$$\begin{bmatrix} \bar{A}^T P + P\bar{A} & P\bar{B}_\lambda + \tau r \bar{C}_z^T & P\bar{B}_d & \bar{C}_e^T \\ \bar{B}_\lambda^T P + \tau r \bar{C}_z & -2\tau & 0 & \bar{D}_{e\lambda}^T \\ \bar{B}_d^T P & 0 & -\gamma I & \bar{D}_{ed}^T \\ \bar{C}_e & \bar{D}_{e\lambda} & \bar{D}_{ed} & -\gamma I \end{bmatrix} \prec 0 \quad (5.10)$$

An upper bound of γ can be found via the following semidefinite program (Appendix A):

$$\begin{aligned} \min \gamma & \quad (5.11) \\ \text{such that } P \succ 0, \tau > 0, \text{ and 5.10} \end{aligned}$$

5.6 Control Synthesis

Our approach to control synthesis is to minimize the upper bound of the induced \mathcal{L}_2 norm from disturbance \mathbf{d} to generalized error \mathbf{e} of the system given by Expressions 5.1 and 5.3 by choosing an LTI output-feedback controller K . An upper bound of γ can be found via the following optimization problem:

$$\begin{aligned} \min_K \gamma & \quad (5.12) \\ \text{such that } P \succ 0, \tau > 0, \text{ and 5.10} \end{aligned}$$

An approach to solve a problem similar to that in 5.12 was presented in [28]. The focus of [28] is on saturation of the controller output and therefore the structure of the interconnection is different to that studied here. With the same philosophy of [28], we extend the approach to control synthesis for LTI plants presented in [11], referred to as H_∞ optimization. Our extended version of the H_∞ synthesis includes the inequality in Expression 5.3 to describe the nonlinear, time-varying uncertainty Φ . We derive the formulas for the output feedback controller that minimize the \mathcal{L}_2 induced norm of a

system described by Equations 5.1 and 5.3. These formulas are derived step by step for the readers interested in customizing the synthesis tools.

5.6.1 Conditions for the Existence of a Controller

Our first step, towards solving problem 5.12, is to separate the controller matrices $\Theta = \begin{bmatrix} A_K & B_K \\ C_K & D_K \end{bmatrix}$ and the rest of the matrices in inequality 5.10. The inequality 5.10 can be rewritten as:

$$U + Z^T \Theta^T Y_P + Y_P^T \Theta Z \prec 0 \quad (5.13)$$

$$Y_P = \begin{bmatrix} \underline{B}^T & 0 & \underline{D}_1^T \end{bmatrix} \begin{bmatrix} P & 0 & 0 \\ 0 & I & 0 \\ 0 & 0 & I \end{bmatrix} = Y \begin{bmatrix} P & 0 & 0 \\ 0 & I & 0 \\ 0 & 0 & I \end{bmatrix}$$

$$Z = \begin{bmatrix} \underline{C} & \underline{D}_2 & 0 \end{bmatrix}$$

$$\underline{B} = \begin{bmatrix} 0_{n \times n} & B_u \\ I_n & 0 \end{bmatrix}$$

$$\underline{C} = \begin{bmatrix} 0_{n \times n} & I_n \\ C_y & 0 \end{bmatrix}$$

$$\underline{D}_1 = \begin{bmatrix} 0_{n_z \times 2n} & D_{eu} \end{bmatrix}$$

$$\underline{D}_2 = \begin{bmatrix} 0_{n \times n_z} & 0_{n \times n_d} \\ D_{y\lambda} & D_{yd} \end{bmatrix}$$

$$U = \begin{bmatrix} \bar{A}_0^T P + P \bar{A}_0 & P \bar{B}_0 & \bar{C}_{e0}^T \\ \bar{B}_0^T P & -M_{\tau\gamma} & \bar{D}_{e0}^T \\ \bar{C}_{e0} & \bar{D}_{e0} & -\gamma I \end{bmatrix}$$

$$A_0 = \begin{bmatrix} A & 0 \\ 0 & 0_{n \times n} \end{bmatrix} \quad B_0 = \begin{bmatrix} B_\lambda + P^{-1} \bar{C}_z^T & B_d \\ 0 & 0 \end{bmatrix}$$

$$C_{e0} = \begin{bmatrix} C_e & 0_{n_e \times n} \end{bmatrix} \quad D_{e0} = \begin{bmatrix} D_{e\lambda} & D_{ed} \end{bmatrix}$$

$$M_{\tau\gamma} = \begin{bmatrix} 2\tau & 0 \\ 0 & \gamma I_{n_d} \end{bmatrix}$$

The structure of 5.13 is convenient to find conditions for solving problem 5.12 and eliminating the controller parameters Θ . The following lemma is key for our results.

Lemma 5. *There exist Θ that satisfies inequality 5.13 if and only if the following*

inequalities hold:

$$N_{Y_P}^T U N_{Y_P} \prec 0 \quad (5.14)$$

$$N_Z^T U N_Z \prec 0 \quad (5.15)$$

N_{Y_P} and N_Z are orthonormal bases of the null spaces of Y_P and Z respectively.

Proof. Presented in [6, p. 32]. □

Note that Y_P and therefore N_{Y_P} depend on P , which is unknown. An important result that helps us separate the unknown matrix P from N_{Y_P} in inequality 5.14 is as follows.

Lemma 6. N_{Y_P} is a basis of the null space of:

$$Y_P = Y \begin{bmatrix} P & 0 & 0 \\ 0 & I & 0 \\ 0 & 0 & I \end{bmatrix}$$

with $Y = \begin{bmatrix} \underline{B}^T & 0 & \underline{D}_1^T \end{bmatrix}$ whenever

$$\begin{bmatrix} P^{-1} & 0 & 0 \\ 0 & I & 0 \\ 0 & 0 & I \end{bmatrix} N_Y$$

is a basis of the null space of N_{Y_P} . N_Y is a basis of the null space of Y .

Proof. Presented in [11]. □

The structures of the null spaces N_Y and N_Z are as follows:

$$N_Y = \begin{bmatrix} N_{B_u^T} & 0_{n \times n_z + n_d} \\ 0 & 0_{n \times n_z + n_d} \\ 0 & I_{n_z + n_d} \\ N_{D_{eu}^T} & 0_{n_e \times n_z + n_d} \end{bmatrix}$$

$$N_Z = \begin{bmatrix} N_{C_y} & 0_{n \times n_e} \\ 0 & 0_{n \times n_e} \\ N_{D_y} & 0_{n_z + n_y \times n_e} \\ 0 & I_{n_e} \end{bmatrix}$$

$N_{B_u^T}$, $N_{D_{eu}}$, N_{C_y} , and N_{D_y} are orthonormal bases of the null spaces of B_u^T , D_{eu}^T , C_y , and $\begin{bmatrix} D_{y\lambda} & D_{yd} \end{bmatrix}$ respectively.

Using Lemma 6, we rewrite condition 5.14 as:

$$N_Y^T V N_Y \prec 0 \tag{5.16}$$

$$V = \begin{bmatrix} P^{-1} & 0 & 0 \\ 0 & I & 0 \\ 0 & 0 & I \end{bmatrix} U \begin{bmatrix} P^{-1} & 0 & 0 \\ 0 & I & 0 \\ 0 & 0 & I \end{bmatrix} =$$

$$\begin{bmatrix} P^{-1} \bar{A}_0^T + \bar{A}_0 P^{-1} & \bar{B}_0 & P^{-1} \bar{C}_{e0}^T \\ \bar{B}_0^T & -M_{r\gamma} & \bar{D}_{e0}^T \\ P^{-1} \bar{C}_{e0} & \bar{D}_{e0} & -\gamma I \end{bmatrix}$$

Conditions 5.15 and 5.16 are linear in variables P and P^{-1} . Yet, these are not linear inequalities with respect to P . The next step in our search for solvability conditions for Θ is to redefine P and P^{-1} as:

$$P = \begin{bmatrix} S & N \\ N^T & \star \end{bmatrix}$$

$$P^{-1} = \begin{bmatrix} R & M \\ M^T & \star \end{bmatrix}$$

where the symbol \star is a place holder for elements not needed in the proceeding computations. Using the definitions of P and P^{-1} , structure of N_Y and N_Z , and algebraic manipulations, conditions 5.15 and 5.16 become:

$$\begin{bmatrix} N_R & 0 \\ 0 & I_{n_z+n_d} \end{bmatrix}^T \begin{bmatrix} AR + RA^T & RC_e & B_\lambda + \tau r RC_z & B_d \\ C_e^T R & -\gamma I_{n_e} & D_{e\lambda} & D_{ed} \\ B_\lambda^T + \tau r C_z^T R & D_{e\lambda}^T & -2\tau & 0_{n_z \times n_d} \\ B_d^T & D_{ed}^T & 0_{n_d \times n_z} & -\gamma I_{n_d} \end{bmatrix} \begin{bmatrix} N_R & 0 \\ 0 & I_{n_z+n_d} \end{bmatrix} \prec 0 \quad (5.17)$$

$$\begin{bmatrix} N_S & 0 \\ 0 & I_{n_e} \end{bmatrix}^T \begin{bmatrix} A^T S + SA & SB_P + \tau C_z^T & SB_d & C_e^T \\ B_\lambda^T S + \tau C_z & -2\tau & 0_{n_z \times n_d} & D_{e\lambda}^T \\ B_d^T S & 0_{n_d \times n_z} & -\gamma I_{n_d} & D_{ed}^T \\ C_e & D_{e\lambda} & D_{ed} & -\gamma I_{n_e} \end{bmatrix} \begin{bmatrix} N_S & 0 \\ 0 & I_{n_e} \end{bmatrix} \prec 0 \quad (5.18)$$

N_R and N_S are orthonormal bases of the null spaces of $\begin{bmatrix} B_u^T & D_{eu}^T \end{bmatrix}$ and $\begin{bmatrix} C_y & D_{y\lambda} & D_{yd} \end{bmatrix}$ respectively. The conditions $P \succ 0$ and $P^{-1} \succ 0$ are equivalent to [11]:

$$\begin{bmatrix} R & I \\ I & S \end{bmatrix} \succeq 0 \quad (5.19)$$

The existence of matrices R and S given conditions 5.17, 5.18 and 5.19 is a sufficient condition for the existence of a controller K that delivers a performance level no greater than γ . The following optimization problem is used to find conditions for the existence of a controller that minimizes γ :

$$\min_{R, S, \tau} \gamma \quad (5.20)$$

such that 5.17, 5.18, and 5.19

Problem 5.20 is non-convex because τ is multiplying R in inequality 5.17. However, since τ is a scalar, we can efficiently search over τ to find an optimal value for γ .

5.6.2 Controller Reconstruction

Given R , S , τ , and γ from the optimization problem 5.20, we can reconstruct Θ , which contains the controller data. To obtain Θ , we follow the controller reconstruction presented in [11]. First, we select full rank matrices $M, N \in R^{n \times n}$ such that $MN^T = I - RS$.

Then we compute P as:

$$P = \begin{bmatrix} I_{n \times n} & S \\ 0_{n \times n} & N^T \end{bmatrix} \begin{bmatrix} R & I_{n \times n} \\ M^T & 0_{n \times n} \end{bmatrix}^{-1}$$

Finally, the controller parameters embedded in Θ can be obtained by solving a feasibility problem with the LMI given in 5.13.

5.7 Local Control Synthesis

The design and analysis tools presented so far in this chapter have considered the global stability and performance of the closed-loop system. When the synthesis tools do not find a feasible solution, one possibility is that there is no quadratic Lyapunov function that proves the existence of an LTI controller and delivers a finite gain γ for all possible states \bar{x} of the closed-loop interconnection.

A way to relax the optimization is to search for a controller in a sector $[0, \underline{r}]$ smaller than the prescribed sector $[0, r]$, with $\underline{r} < r$. The value of \underline{r} for which a controller exists, determines a set of states in which the closed-loop system achieves the performance level γ as computed by a quadratic Lyapunov function. The value of \underline{r} imposes constraints on λ , z , and \bar{x} of the form:

$$\begin{aligned} |z| &\leq \frac{\epsilon}{1 - \underline{r}} = \bar{\bar{z}} \\ |\bar{C}_z \bar{x}| &\leq \bar{\bar{z}} \\ |\lambda| &\leq \bar{\bar{z}} - \epsilon = \bar{\bar{\lambda}} \end{aligned}$$

When we design a controller that guarantees performance locally, the uncertainty of the vehicle dynamics is still a dead-zone with variable slope, but restricted to $z \leq \bar{\bar{z}}$. Figure 5.3 depicts how the original uncertain region (light blue area) is reduced to the region bounded by $z \leq \bar{\bar{z}}$ (black area). It also shows the updated sector constraint that covers the local uncertainty region. This sector $[0, \bar{r}]$ is drawn in gray.

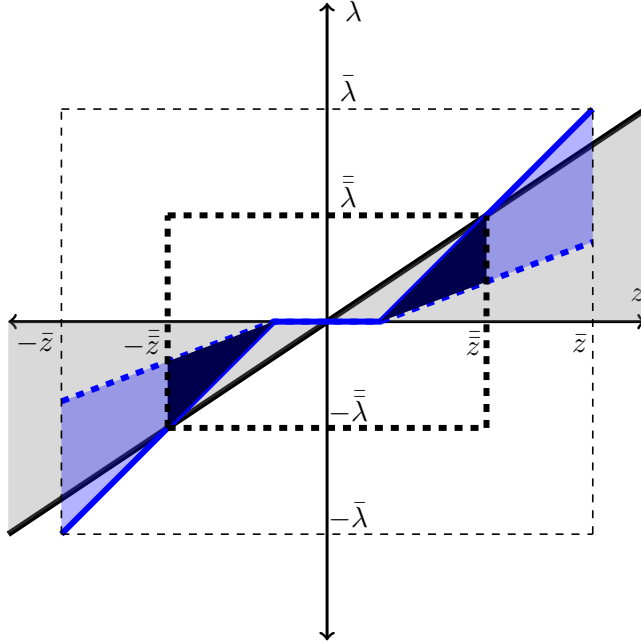


Figure 5.3: Schematic of dead-zone with variable slope and constraint on z

Although, the quadratic Lyapunov function used for local synthesis does not prove the performance of level γ globally, the resulting controller may still deliver a finite gain globally. This could be proven with more sophisticated tools that consider a richer set of Lyapunov functions and a better description of the uncertainty. For example, sum of squares (SOS) optimization could assess the stability of a system by using polynomial Lyapunov functions. See [38] and the references therein.

If there is no way to demonstrate that the controller stabilizes the system globally, we would need to assess the stability locally. Specifically, we would need to investigate the set of inputs and initial conditions for which the system remains stable. Although the local stability assessment is an important piece of information for control development, this topic is out of the scope of this thesis. The reader is encouraged to review ongoing research on local stability in [34, 37, 39] and the references therein.

5.8 Remarks on the Synthesis Tools

Remark 1: Controllers can be designed with the proposed tools by following the methodologies employed in H_∞ synthesis. Therefore, designers familiar with H_∞ optimization would easily transition to these tools.

Remark 2: The controller synthesis tools can be readily extended to Linear Parameter Varying (LPV) systems. This is specially useful for designing a controller that guarantees performance for a supercavitating vehicle subject to variations in the axial speed.

Remark 3: The synthesis tools can be used to study the benefit of measuring the immersion λ in real time. This is possible because $D_{y\lambda}$ is not assumed zero.

Remark 4: The controller synthesis tools presented in Section 5.6 can be extended to have $n_z > 1$ nonlinear elements. In that case, we would need n_z slack variables τ_i for $i = 1, 2, \dots, n_z$. A search over the n_z slack variables would be needed to find an optimal γ . This is a nonlinear optimization problem that can be addressed with local search algorithms, which in general do not converge to global minima, but may provide satisfactory designs.

Remark 5: The controller synthesis tools apply to systems with any nonlinear time-varying uncertainty Φ .

5.9 Control Design for 1-DOF Test Vehicle

We direct our attention to the 1-DOF test vehicle, described in Section 3.3, for control design and experimental validation. The same methodology can be applied to the 3-DOF vehicle that would travel under the sea. The objectives of the controllers for the 1-DOF vehicle include:

1. Tracking attack angle reference commands r
2. Respecting actuation limits including saturation and bandwidth. Recall that the maximum deflections of the cavitator and fins are 20 and 15 deg respectively.
3. Filtering noise arising from high frequency vibrations

A schematic of the interconnection for control synthesis is presented in Figure 5.4. The control design is performed in the continuous time, although the controllers are converted to discrete time for implementation on the real-time system. G is the vehicle body dynamics whose inputs are the immersion λ and surface deflections $\delta = \begin{bmatrix} \delta_c \\ \delta_f \end{bmatrix}$, and whose outputs are the attack angle α and relative position between the vehicle and supercavity z . The numerical representation of the vehicle model G is presented

in Section 4.11.2. Act is the actuation dynamics of the cavitator and fins whose inputs are the commands $u = \begin{bmatrix} \delta_{cr} \\ \delta_{fr} \end{bmatrix}$ and whose outputs are the deflections δ . D is the time delay of the open-loop interconnection caused by the electronics, control computer, and operating system. This delay is represented by a first order Pade approximation whose input is the measured attack angle and output is α_m . Recall from Section 3.6 that our time delay is 30 ms.

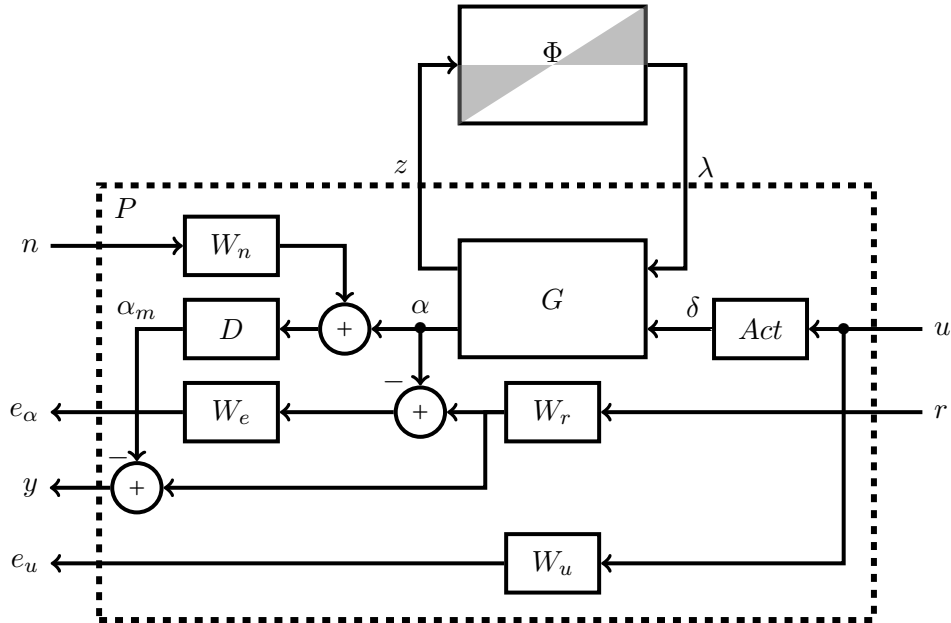


Figure 5.4: Schematic of generalized plant for control synthesis

We employ the LTI transfer functions W_r , W_n , W_u , and W_e to specify the performance of the closed-loop system. These weights shape the steady state response of the inputs and outputs of the system across frequency. W_n accentuates the amplitude of the noise n at high frequency. W_r specifies that the reference r has higher energy at low frequency. The weighted reference r minus α_m is the measured tracking error y fed to the controller. The attack angle α is subtracted from the weighted reference to obtain the actual tracking error. This error is passed through W_e , a low-pass filter specifying the need of tracking at low frequency. The output of W_e is the normalized tracking error e_α . W_u limits the energy of controller commands u at frequencies beyond the actuator bandwidths. The numerical representations of the weights we selected are presented as

follows, with s denoting the Laplace variable.

$$\begin{aligned}
 W_r &= \frac{1.18}{s + 15} & W_n &= \frac{0.55s + 0.12}{s + 23.04} \\
 W_u &= \left(\frac{57.3s + 1297}{s + 906} \right) \begin{bmatrix} 1 & 0 \\ 0 & 1 \end{bmatrix} & W_e &= \frac{0.83s + 17.37}{s + 0.087}
 \end{aligned}$$

The main objective of the controller to be designed is to make the induced \mathcal{L}_2 from $d = \begin{bmatrix} r \\ n \end{bmatrix}$ to $e = \begin{bmatrix} e_\alpha \\ e_u \end{bmatrix}$ as small as possible by using y and u .

The interconnection of Figure 5.4 is used to synthesize two controllers. A baseline controller K_∞ , is designed via H_∞ optimization. In this design, the nonlinear uncertain element Φ and related signals λ and z are neglected. The H_∞ controller is used to evaluate the benefit of considering Φ within the synthesis.

A controller K_{sc} is designed with the approach developed in this chapter. It is important to recall that the sector constrained method is an extension of H_∞ in which a nonlinear, time varying, uncertainty Φ is considered. Therefore, by comparing K_{sc} and K_∞ we fairly evaluate the benefit of having a description of planing (Φ).

5.9.1 H_∞ Controller

A baseline control law K_∞ is designed based on the techniques presented in [11] and tools described in [3]. The design procedure employs the aforementioned weights to minimize the \mathcal{L}_2 induced norm from \mathbf{d} to \mathbf{e} of the interconnection that neglects Φ . It returns a controller for which the gain from d to e of the closed-loop *linear* dynamics is $\gamma_{lin} = 0.99$.

By employing the tools described in Sections 5.4 and 5.5, we cannot conclude that the *nonlinear-uncertain* system is stable or has a finite gain. This means that either the tools cannot find a quadratic Lyapunov function to prove stability and finite gain globally or the closed-loop system is not globally asymptotically stable.

5.9.2 Sector Constrained–SC–Controller

A control law K_{sc} is designed by including the sector constraint as described in Section 5.6. The existence of the controller automatically proves an upper bound of the induced \mathcal{L}_2 norm of the *nonlinear-uncertain* closed-loop dynamics. This bound is $\gamma = 1.15$.

Additionally, the closed-loop nonlinear system is found to be globally asymptotically stable via a quadratic Lyapunov function as described in Section 5.4. Given that the uncertainty model captures the full nonlinear vehicle dynamics, this method provides a formal proof of performance and stability. Such a proof is highly desired for critical systems as the one under consideration.

We would like to revisit the circle criterion for stability assessment presented in Lemma 4. According to this criterion, the input to output map $-H(j\omega)$ from λ to z is stable if the leftmost point of its Nyquist plot does not cross $-1/r$. The Nyquist plot for the systems with both K_∞ and K_{sc} are presented in Figure 5.5. Stability cannot be proven via the circle criterion for the closed-loop system with K_∞ . In contrast, controller K_{sc} moves the Nyquist plot to the right side of $-1/r$ and thereby achieves stability by the circle criterion.

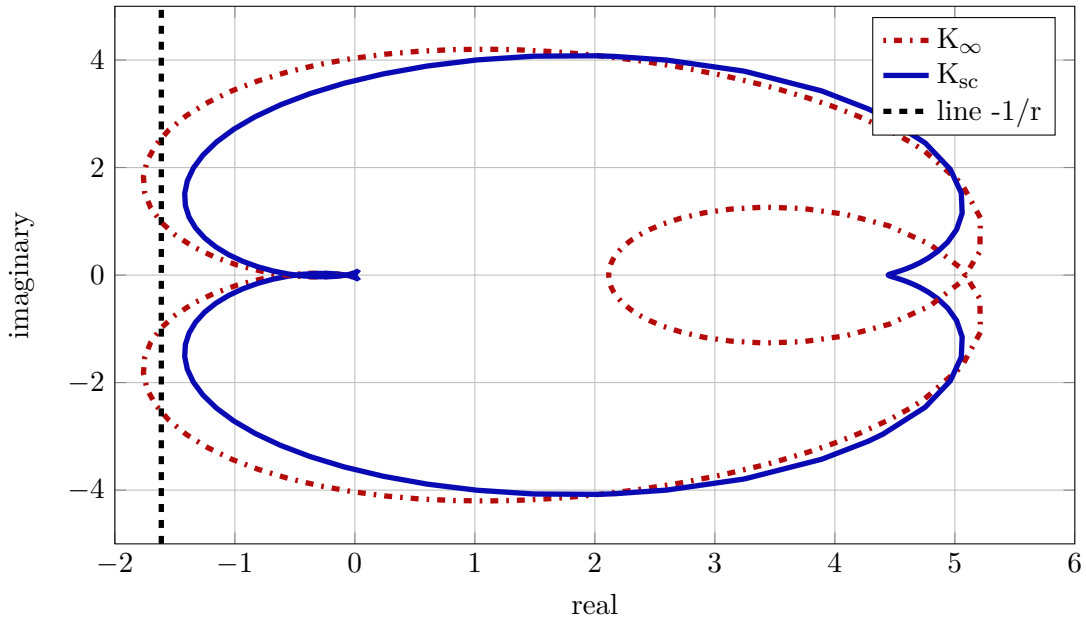


Figure 5.5: Nyquist plot of open-loop and closed-loop systems

The Bode plots of both controllers that illustrate the magnitude and phase between the tracking error y and the cavitator command δ_{c_r} are presented in Figure 5.6. A first difference to highlight is that the magnitude of K_{sc} is higher at frequencies above 0.01 rad/s. The phase of K_{sc} is also higher for frequencies below 130 rad/s, in particular near the crossover frequency. The contribution of K_{sc} to the closed-loop magnitude and phase in the mid frequencies pushes the map from λ to z towards the right side

of the Nyquist plane. In this way, K_{sc} enhances the robustness of the closed-loop interconnection. The specific role of the cavitator channel is key to enhance robustness to Φ because the gain from δ_c to z is greater than the gain from δ_f to z at low and mid frequencies. This means that the cavitator has more authority than the fins to reshape the response of z and therefore the map from λ to z .

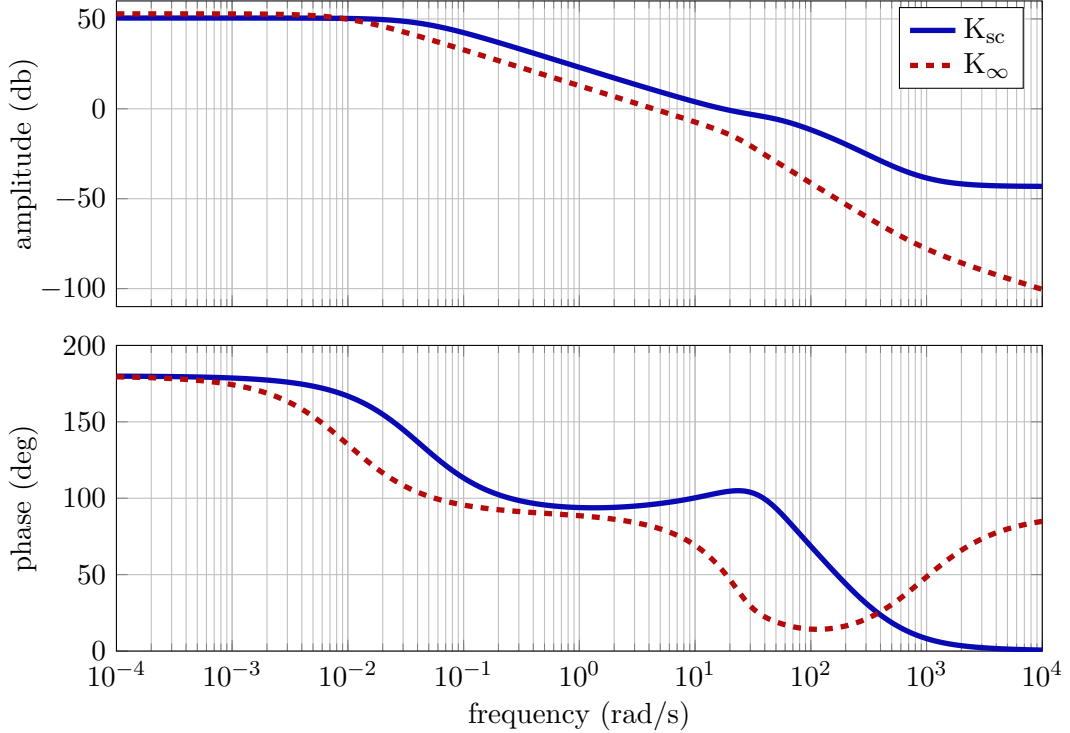


Figure 5.6: Bode plots for K_∞ and K_{sc} from y to δ_{c_r} .

The Bode plots that illustrate the magnitude and phase between the tracking error y and fin command δ_{f_r} are presented in Figure 5.7. Controller K_∞ yields a higher magnitude at frequencies below 20 rad/s. This suggests that K_∞ relies more on the fins to achieve the control objectives. An important observation is that the behavior of the cavitator and fin channels in K_∞ is the same. The only difference being that the Bode magnitude of the response of δ_{f_r} is a scaled version of that of δ_{c_r} . The synthesis of K_{sc} considers the effect of the cavitator and fin deflections on z . Hence, the frequency responses of the cavitator and fin channels are independently shaped to enhance the robustness of the system given Φ .

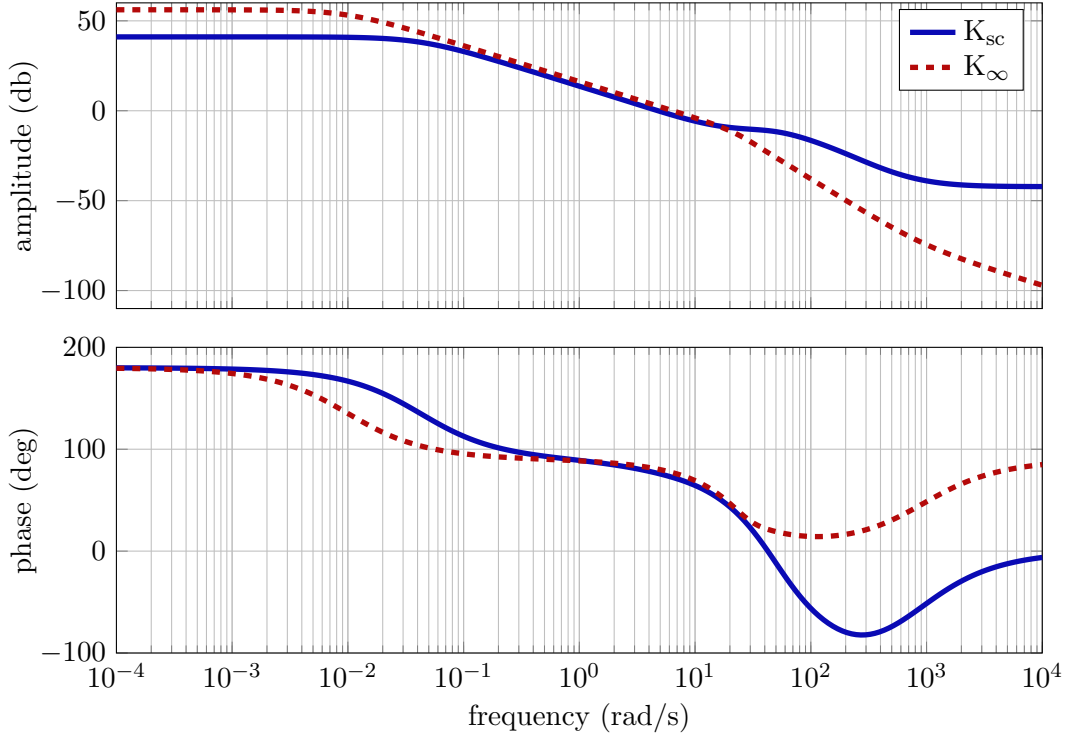


Figure 5.7: Bode plots for K_{∞} and K_{sc} from y to δ_{f_r}

5.10 Experimental Validation

The experimental vehicle described in Section 3.3 is used to evaluate the control laws K_{∞} and K_{sc} under non-linear planing phenomena and realistic flow conditions in the SAFL high speed water tunnel. We conducted an experiment to evaluate K_{∞} and K_{sc} subject to the same flow conditions and attack angle commands r . Step-up and step-down commands between -2 and 4 deg were applied to r . When the vehicle approached 4 deg, planing emerged for both controllers. The responses of the systems are illustrated in Figure 5.8.

The top plot shows the reference r and corresponding attack angle measurements for both controllers. Although in the linear region (inside the supercavity) both controllers perform excellent, K_{sc} outperforms K_{∞} when planing occurs. Oscillations present in the K_{∞} interconnection are minimized by K_{sc} . This suggests that considering planing for control contributes to achieving a better performance in practice.

The middle plot presents the cavitator commands δ_{c_r} . K_{sc} demands large cavitator deflections to move the supercavity and thereby minimize planing immersion. K_{sc}

actively controls the supercavity by using its knowledge of the influence of δ_c on the supercavity dynamics. This active control capability is unique in our formulation. Since K_{sc} mostly uses the cavitator to meet the control objectives, it requires smaller fin deflections than K_∞ .

The bottom plot illustrates the fin deflections. K_∞ tries to meet its control objectives by mostly actuating the fin deflection. This occurs because K_∞ does not know about planing and the ability of the cavitator to displace the supercavity. The steady state

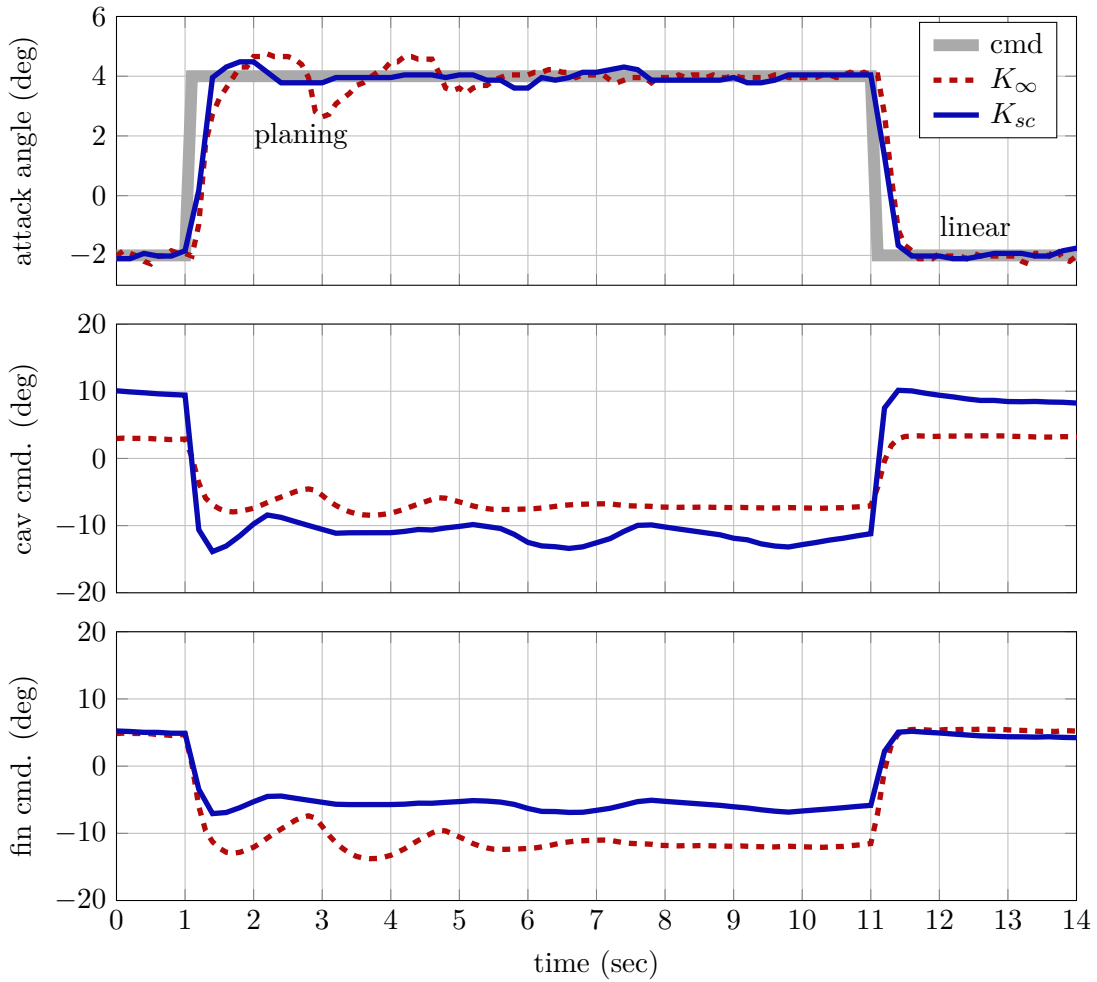


Figure 5.8: Experiment with H_∞ and sector-constrained controllers. cmd. stands for command.

responses of the vehicle with both controllers are shown in the pictures of Figure 5.9.

The superiority of K_{sc} over K_∞ is consistent with multiple experiments. In Figure

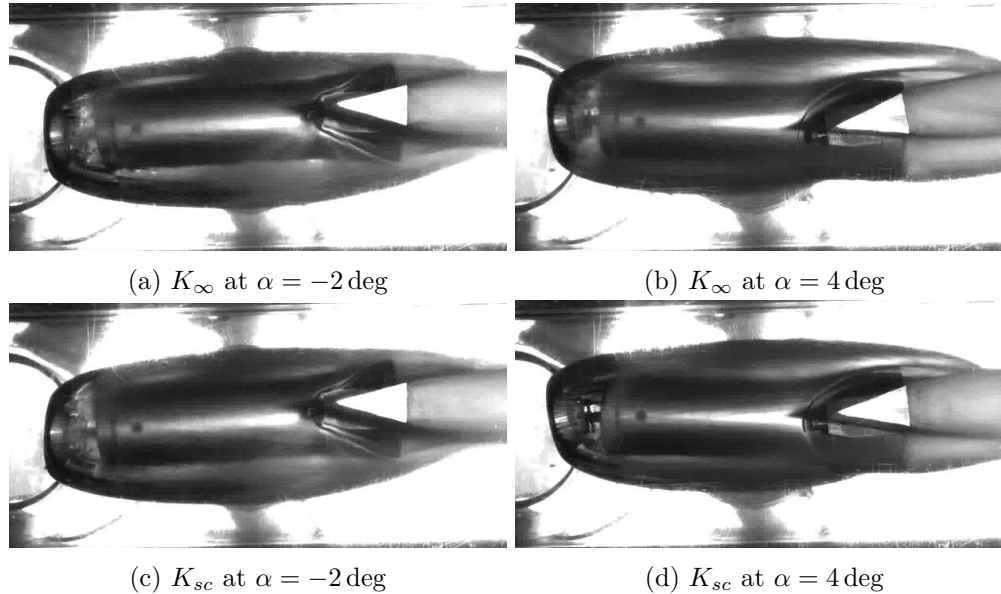


Figure 5.9: Pictures of steady state responses for H_{∞} and sector constrained controllers

5.10, we show four samples of the same experiment with both controllers. Note that the attack angle response of the system with K_{sc} is displaced 4 deg vertically for proper visualization.

A more challenging maneuver for K_{sc} is presented in Figure 5.11. In this maneuver, the closed-loop system maintains an excellent tracking performance during planing ($\alpha \rightarrow 4$ deg) and non-planing ($\alpha \rightarrow -2$ deg.) conditions. The controller does not saturate the control surfaces. It also provides excellent filtering to vibrational effects; therefore, the control surfaces are actuated only at low frequency.

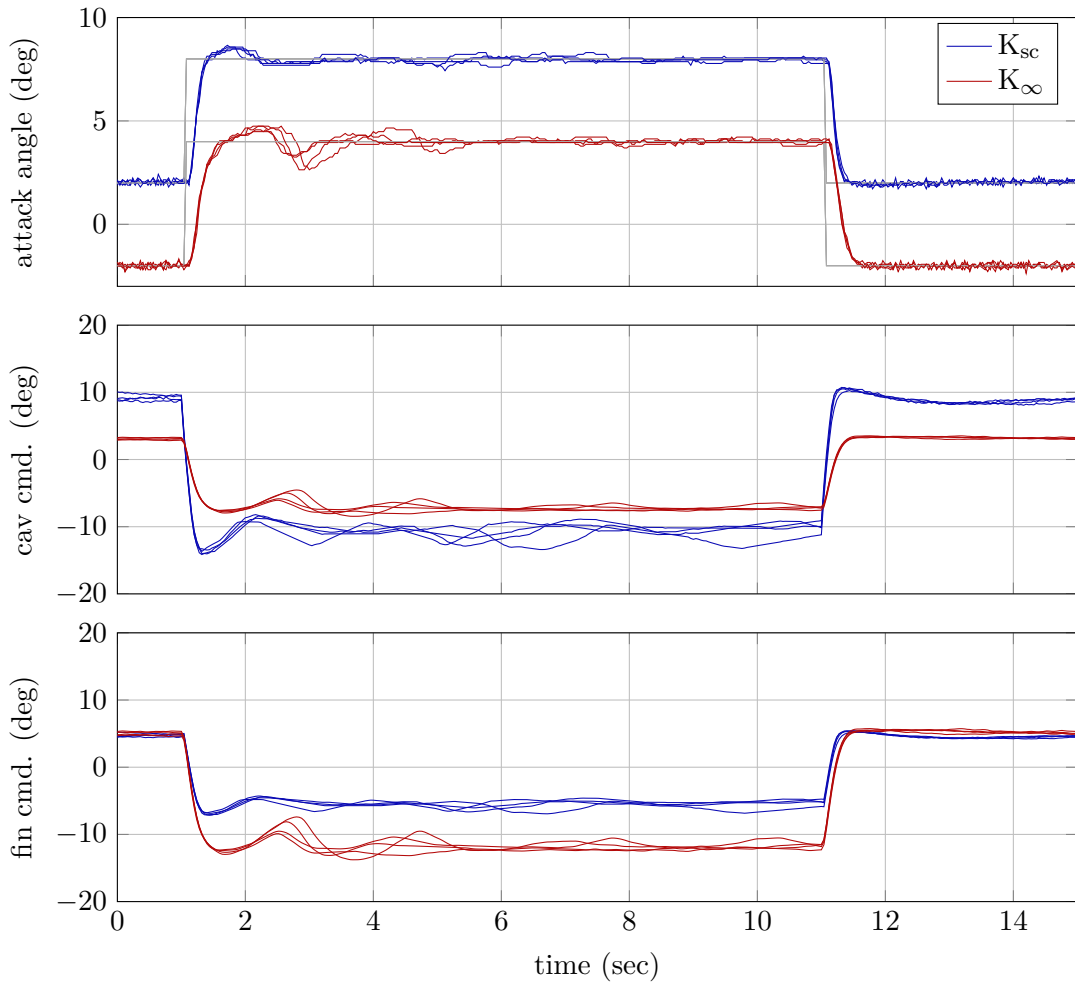


Figure 5.10: Experiments with H_{∞} and sector-constrained controllers. cmd. stands for command.

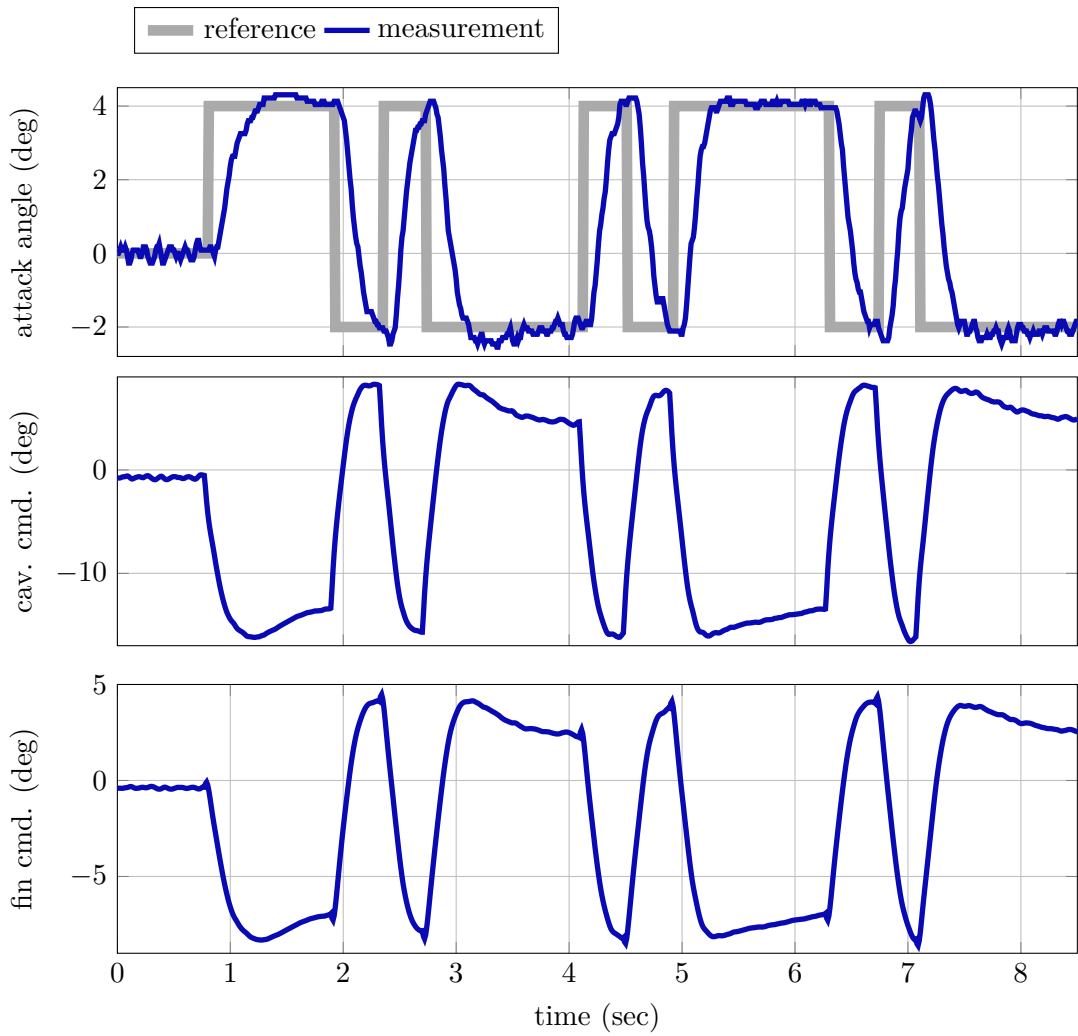


Figure 5.11: Experiment with sector-constrained controller and agile maneuver. cmd. stands for command.

Chapter 6

Conclusions and Future Directions

6.1 Concluding Remarks

In this dissertation, we have presented methods for modeling, robust control, and experimental validation of the nonlinear dynamics of a supercavitating vehicle. Major conclusions in regard to these methods are as follows.

1. **Modeling:** A supercavitating vehicle traveling at trim speed can be represented by an LTI system in feedback with a dead-zone operator. To capture the imprecise modeling of the planing forces and the interaction between the supercavity and vehicle body in the planing region, we employ a sector constraint in which a variable-slope dead-zone lies. By capturing the effect of the cavitator deflection and attack angle on the supercavity dynamics, we actively control the supercavity and thereby improve the closed-loop vehicle performance. Our uncertainty model allows designers to synthesize and formally validate control technologies using efficient computational tools.
2. **Robust Control:** An LTI output-feedback control law is sufficient to drive the motion of a supercavitating vehicle accurately and robustly. We formulate a synthesis method that guarantees performance in the face of nonlinear uncertain planing forces. The control synthesis method enables us to use both cavitator and fins for control as well as available measurements without the need of full state information.

3. **Experimental validation:** Experiments with a test vehicle capable of pitching in a high-speed water tunnel provide deep insight into the advantages and disadvantages of control technologies for a supercavitating vehicle. We experimentally showed that our proposed robust control technique delivers excellent performance under planing and realistic flow conditions.

6.2 Research Directions

There are several aspects in the modeling, control, and validation of a supercavitating vehicle that require further attention:

1. **Modeling:** A control oriented model of the supercavitating vehicle traveling at variable speeds (accelerations and decelerations) is needed. A Linear Parameter Varying (LPV) model [27, 46] would readily extend our vehicle abstraction by considering the axial speed U_0 as the varying parameter. Another key aspect for further consideration is the six-degrees of freedom vehicle motion. We suggest that a dead-zone operator could be used to compute the magnitude of planing forces. The force direction could be then calculated based upon the relative position of the vehicle and supercavity. We hypothesize that such a nonlinear model would be suitable to synthesize robust controllers for the full nonlinear dynamics.
2. **Robust Control:** Robust control approaches for the 6-DOF vehicle traveling at variable speeds are still needed. The synthesis tools we developed can be easily adapted to contemplate acceleration and deceleration maneuvers. Specifically, by using an LPV vehicle model, a controller scheduled with the axial speed U_0 could be designed. The LPV synthesis tools could be constructed based on the control methods presented in Chapter 5 and the available literature on LPV control [1, 46, 47]. Additionally, control approaches for LPV systems subject to uncertainty, based on integral quadratic constraints (IQCs), provide an excellent fit to this problem. See for example [29, 35, 45] and the references therein. This LPV-IQC framework is a flexible approach to include dead-zones, saturations, and parametric uncertainties into the analysis and synthesis.
3. **Experimental Validation:** An affordable testing method for a supercavitating vehicle subject to variations in water speed would provide great insight into controlling the full nonlinear vehicle dynamics. By varying the water tunnel speed during control experiments with the platform presented Chapter 3, we would be

able to evaluate control technologies that adapt to variations of speed. Scheduling controllers would be possible by estimating the water speed via measurements of the force along the axial vehicle axis. Moreover, we believe that a better understanding of the impact of planing on the vehicle dynamics can be reached if the control facility presented in Chapter 3 is enhanced. The main drawback to be addressed is the lateral planing induced by the rotary shaft. Removing the lateral planing will enable researchers to evaluate control technologies subject to more challenging switching dynamics.

Bibliography

- [1] P. Apkarian, P. Gahinet, and G. Becker. Self-scheduled h-infinity control of linear parameter-varying systems: a design example. *Automatica*, 31(9):1251 – 1261, 1995.
- [2] G. Balas, J. Bokor, B. Vanek, and R.E.A. Arndt. Control of high-speed underwater vehicles. In *Control of Uncertain Systems: Modelling, Approximation, and Design*, pages 25–44. Springer, 2006.
- [3] G. Balas, R. Chiang, A. Packard, and M. Safonov. Robust control toolbox 3 user’s guide. Technical report, The MathWorks, 2007.
- [4] H. Baruh. *Analytical Dynamics*. Engineering Mechanics Series. WCB/McGraw-Hill, 1999.
- [5] J.J. Bertin and M.L. Smith. *Aerodynamics for Engineers*. Prentice Hall, 1998.
- [6] S. Boyd, L.E. Ghaoui, E. Feron, and V. Balakrishnan. *Linear Matrix Inequalities in System and Control Theory*. Studies in Applied Mathematics. Society for Industrial and Applied Mathematics, 1994.
- [7] J.J. Craig. *Introduction to Robotics: Mechanics and Control*. Addison-Wesley series in electrical and computer engineering: control engineering. Pearson Education, Incorporated, 2005.
- [8] Inc. CVX Research. CVX: Matlab software for disciplined convex programming, version 2.0. <http://cvxr.com/cvx>, August 2012.
- [9] J. Dzielski and A. Kurdila. A benchmark control problem for super-cavitating vehicles and an initial investigation of solutions. *Journal of Vibration and Control*, 9(7):791–804, 2003.

- [10] D. Escobar, G. Balas, and R.E.A. Arndt. Modeling, control, and experimental validation of a high-speed supercavitating vehicle. *Oceanic Engineering, IEEE Journal of*, PP(99):1–12, 2014.
- [11] P. Gahinet and P. Apkarian. A linear matrix inequality approach to H_∞ control. *International Journal of Robust and Nonlinear Control*, 4(4):421–448, 1994.
- [12] P. Gahinet, A. Nemirovskii, A.J. Laub, and M. Chilali. The lmi control toolbox user’s guide. 1995.
- [13] Juliet Marine Systems Inc. Ghost vessel description.
- [14] E. Kawakami and R.E.A. Arndt. Investigation of the behavior of ventilated supercavities. *Journal of Fluids Engineering*, 133(9):091305, 2011.
- [15] R.W. Kermeen. Experimental investigation of three-dimensional effects on cavitating hydrofoils. Technical Report 47-60, California Institute of Technology, 1960.
- [16] H.K. Khalil. *Nonlinear Systems*. Prentice Hall, 2002.
- [17] I. N. Kirschner, D. C. Kring, A. W. Stokes, N. E. Fine, and J. S. Uhlman. Control Strategies for Supercavitating Vehicles. *Journal of Vibration and Control*, 8, 2002.
- [18] G. Lin, B. Balachandran, and E. Abed. Supercavitating body dynamics, bifurcations and control. In *American Control Conference, 2005. Proceedings of the 2005*, pages 691–696 vol. 1, June 2005.
- [19] L. Ljung. *System identification - Theory for the User*. Prentice-Hall, 1999.
- [20] L. Ljung. System Identification Toolbox User’s Guide R2014b. Technical report, The MathWorks, 2004.
- [21] J. Lofberg. Yalmip : A toolbox for modeling and optimization in MATLAB. In *Proceedings of the CACSD Conference, Taipei, Taiwan, 2004*.
- [22] G. Logvinovich. Hydrodynamics of free-boundary flows. *US Department of Commerce, Washington D.C.*, 1972. translated from the Russian (NASA-TT-F-658).
- [23] G. Logvinovich. Some problems in planing surfaces. *Trudy TsAGI*, (2052), 1980. Translated from: Nekotoryye voprosy glissirovaniya i kavitatsii [Some Problems in Planing and Cavitation].

- [24] A.M. Lyapunov. *General Problem of the Stability Of Motion*. Control Theory and Applications Series. Taylor & Francis, 1992.
- [25] P. M. Makila and J. R. Partington. Laguerre and kautz shift approximations of delay systems. *International Journal of Control*, 72(10):932–946, 1999.
- [26] X. Mao and Q. Wang. Nonlinear Control Design for a Supercavitating Vehicle. *IEEE Transactions on control systems technology*, 17(4), 2009.
- [27] A. Marcos and G. Balas. Development of linear-parameter-varying models for aircraft. *Journal of Guidance, Control, and Dynamics*, 27(2):218–228, 2004.
- [28] T. Pare, H. Hindi, J.P. How, and D. Banjerdpongchai. Local control design for systems with saturating actuators using the popov criteria. In *American Control Conference, 1999. Proceedings of the 1999*, volume 5, pages 3211–3215. IEEE, 1999.
- [29] H. Pfifer and P. Seiler. Robustness analysis of linear parameter varying systems using integral quadratic constraints. *International Journal of Robust and Nonlinear Control*, 2014.
- [30] J. Rice. Investigation of a Two-Dimensional Hydrofoil in Steady and Unsteady Flows. Master’s thesis, Department of Ocean Engineering, MIT, 1992.
- [31] S. Sastry. *Nonlinear Systems: Analysis, Stability, and Control*. Interdisciplinary Applied Mathematics. Springer New York, 2010.
- [32] L.G. Shapiro and G.C. Stockman. *Computer vision*. Prentice Hall, 2001.
- [33] Pierre Soille. *Morphological Image Analysis: Principles and Applications*. Springer-Verlag New York, Inc., Secaucus, NJ, USA, 2 edition, 2003.
- [34] E. Summers, A. Chakraborty, W. Tan, U. Topcu, P. Seiler, G. Balas, and A. Packard. Quantitative local analysis for nonlinear systems. *International Journal of Robust and Nonlinear Control*, 23(10):1115–1135, 2013.
- [35] B. Takarics and P. Seiler. Gain scheduling for nonlinear systems via integral quadratic constraints. In *accepted to the American Control Conference*, 2015.
- [36] K. C. Toh, M.J. Todd, and R.H. Tutuncu. Sdpt3 - a matlab software package for semidefinite programming. *Optimization Methods and Software*, 11:545–581, 1998.
- [37] U. Topcu, A. Packard, and P. Seiler. Local stability analysis using simulations and sum-of-squares programming. *Automatica*, 44(10):2669–2675, 2008.

- [38] U. Topcu, A. Packard, P. Seiler, and G. Balas. Ask the experts: Help on sos. *IEEE Control Systems Magazine*, 30(4):18–23, 2010.
- [39] U. Topcu, A. Packard, P. Seiler, and G. Balas. Robust region-of-attraction estimation. *IEEE Transactions on Automatic Control*, 55(1):137–142, 2010.
- [40] B. Vanek. *Control Methods for High-Speed Supercavitating Vehicles*. PhD thesis, University of Minnesota, 2008.
- [41] B. Vanek, J. Bokor, G. Balas, and R.E.A. Arndt. Longitudinal motion control of a high-speed supercavitation vehicle. *Journal of Vibration and Control*, 13(2):159–184, 2007.
- [42] R.L. Waid. Cavity shapes for circular disks at angles of attack. Technical Report E-73.4, California Institute of Technology, Hydrodynamics Laboratory, 1957.
- [43] R.L. Waid. Water Tunnel Investigation of Two-Dimensional Cavities. Technical Report E-73.6, California Institute of Technology, Hydrodynamics Laboratory, 1957.
- [44] R.L. Waid and R. W. Kermeen. Forces on cylinders. Planing on flat and curved surfaces in cavitating and noncavitating flow. Technical Report E-73.4, California Institute of Technology, Hydrodynamics Laboratory, 1957.
- [45] S. Wang, H. Pfifer, and P. Seiler. Robust synthesis for linear parameter varying systems using integral quadratic constraints. *submitted to Automatica*, 2014.
- [46] F. Wu. *Control of linear parameter varying systems*. PhD thesis, University of California at Berkeley, 1995.
- [47] F. Wu, X. Yang, A. Packard, and G. Becker. Induced l_2 -norm control for lpv system with bounded parameter variation rates. In *American Control Conference, Proceedings of the 1995*, volume 3, pages 2379–2383. IEEE, 1995.
- [48] G. Zames and P. L. Falb. Stability conditions for systems with monotone and slope-restricted nonlinearities. *SIAM Journal on Control*, 6(1):89–108, 1968.

Appendix A

Mathematical Tools

In this appendix, we describe mathematical tools that enable us to develop the control synthesis tools in Chapter 5.

A.1 Linear Matrix Inequalities

A linear matrix inequality (LMI) has the form:

$$F(\mathbf{x}) = F_0 + \sum_{i=1}^m x_i F_i > 0, \quad (\text{A.1})$$

where $\mathbf{x} = [x_0 \ x_1 \ \dots \ x_m]^T \in \mathbb{R}^m$ is the vector of parameters, $F_i = F_i^T \in \mathbb{R}^n$ for $i = 0, 1, \dots, m$ are constant symmetric matrices.

LMIs are convenient to formulate optimization and feasibility problems that arise in systems and control theory. In particular, an LMI is a convex constraint on \mathbf{x} that allows us to formulate convex optimization problems. These convex problems are of interest because global optima can be obtained with tractable computations. Another feature to highlight is that linear and some nonlinear inequalities can be represented as LMIs. Therefore, LMIs are a flexible framework to formulate constrained, convex, tractable optimization problems.

A.2 Semidefinite Programming

Semidefinite programming (SDP) is a type of convex optimization problem of the form:

$$\text{minimize } f_0(\mathbf{x}) = c^T \mathbf{x} \tag{A.2}$$

$$F(\mathbf{x}) > 0, \tag{A.3}$$

which consists of finding the vector variable $\mathbf{x} \in \mathbb{R}^n$ that minimizes a linear objective function ($c^T \mathbf{x}$) given an LMI constraint ($F(\mathbf{x}) > 0$). We are sometimes interested in finding whether or not an LMI is feasible. In such a case, we would have an SDP whose objective function is $f_0(\mathbf{x}) = 0$. If there is solution \mathbf{x} to that SDP, then the LMI is feasible.

An SDP can be solved in polynomial time, meaning that the time to solve the problem is upper bounded by a polynomial, which is function of the input size n . Polynomial time algorithms are considered fast and efficient. To solve an SDP, there are available open source and commercial solvers as CVX, SDPT3, and LMILab [8, 12, 36] as well as integrated environments as Yalmip [21].

In this thesis, SDPs are key for system analysis and control synthesis. The stability of a system as described in Section 5.4 is assessed by solving an LMI feasibility problem. Similarly, the performance quantification and control synthesis of problems 5.5 and 5.12 are solved via SDPs.

A.3 Matrix Variables

Affine inequalities of matrix variables can be represented as LMIs with the form A.1. For example, the Lyapunov inequality:

$$A^T P + P A \prec 0 \tag{A.4}$$

with a matrix variable $P \in \mathbb{S}_{++}^n$ and constant matrix $A \in \mathbb{R}^{n \times n}$, can be represented by an LMI. One first decomposes the variable P as:

$$P = \sum_{i=1}^{n(n+1)/2} x_i P_i, \tag{A.5}$$

where P_i are bases of a symmetric matrix and x_i are scalar variables. The inequality in Expression A.4 becomes:

$$\sum_{i=1}^{n(n+1)/2} x_i (A^T P_i + P_i A) < 0, \quad (\text{A.6})$$

which is an LMI of the form A.1.

In general, by separating matrix variables into their basis functions multiplied by scalar variables, we can represent an affine matrix inequality as a standard LMI.

A.4 Schur Complement

The Schur complement helps us convert a nonlinear inequality constraint of the form:

$$Q(\mathbf{x}) - S(\mathbf{x})R(\mathbf{x})^{-1}S(\mathbf{x})^T \succ 0 \quad (\text{A.7})$$

$$R(\mathbf{x}) \succ 0 \quad (\text{A.8})$$

into an LMI [6]. The idea of the Schur complement is that inequalities (A.7) and (A.8) are equivalent to:

$$\begin{bmatrix} Q(\mathbf{x}) & S(\mathbf{x}) \\ S(\mathbf{x})^T & R(\mathbf{x}) \end{bmatrix} \succ 0 \quad (\text{A.9})$$

A.5 S-Procedure

A particular case of the S-procedure [6] is considered in this thesis to convert two inequalities of quadratic form into an LMI. The following inequalities:

$$\zeta^T T_0(\mathbf{x}) \zeta > 0 \quad (\text{A.10})$$

$$\zeta^T T_i(\mathbf{x}) \zeta > 0, \text{ for } i = 1, 2, \dots, p \quad (\text{A.11})$$

hold if there exists $\tau_i > 0$ for $i = 1, 2, \dots, p$ such that:

$$T_0(\mathbf{x}) - \sum_{i=1}^p \tau_i T_i(\mathbf{x}) \succ 0 \quad (\text{A.12})$$

where $T_0(\mathbf{x}) \in \mathbb{R}^{n \times n}$, $T_i(\mathbf{x}) \in \mathbb{R}^{n \times n}$, $\zeta \in \mathbb{R}^n$, and $\tau_i \in \mathbb{R}$.

The S-procedure is a very useful tool in the derivation of stability and performance conditions for our control synthesis problem 5.12. By employing the S-procedure we are capable of integrating the quadratic constraint that describes Φ into Lyapunov stability conditions. Thereby, we are able to analyze the system stability and synthesize controllers via SDPs.

Appendix B

Image Segmentation

In this appendix, we describe an image segmentation technique to automatically compute the boundary of a supercavity by using images and video streams. The technique allows us to measure the immersion of the vehicle into the fluid and derive models of planing forces in Chapter 4.

B.1 Definitions

A gray scale image $I \in \mathbb{Z}^{n \times m}$ is a matrix whose elements (pixels) are $I(i, j) \in [0, 255]$, for $i = 1, 2, \dots, n$ and $j = 1, 2, \dots, m$. A binary image is that whose elements are either 0 or 1. E denotes an image of dimension n by m with ones in all the entries.

The intersection of two binary images I_1 and I_2 is defined as:

$$I_1 \cap I_2 = I_3 \text{ so that}$$
$$I_3(i, j) = I_1(i, j) \wedge I_2(i, j) \text{ for } i = 1, 2, \dots, n \text{ and } j = 1, 2, \dots, m$$

with \wedge being the AND binary operator.

B.2 Method

Our method for supercavity extraction consists of the following steps:

1. Cutting the region of interest: The area where the bubble lies is extracted from the overall image. The image we obtain is denoted as I_0 . This image has smaller

size than the original image and yields minimal computations.

2. Subtracting background: A picture of the tunnel test section with the vehicle but no supercavity is used to remove static features. The image with the subtracted background is given by:

$$I_1 = (255 \cdot E - I_0) - s_b \cdot (255 \cdot E - I_{back}) \quad (\text{B.1})$$

$$= 255 \cdot (1 - s_b) \cdot E + s_b \cdot I_{back} - I_0 \quad (\text{B.2})$$

where s_b is a scale factor that compensates for the difference between the brightness of the original and background images, I_{back} and I_0 are n by m matrices representing the original and background images, and I_1 is the image after the background subtraction.

3. Averaging image: The pixels of I_1 are averaged with their eight neighbors. This step removes abnormal intensity values from the image.
4. Image thresholding: Based on an intensity histogram of I_1 , we select a threshold τ to zero out pixels that do not belong to the supercavity. The resulting binary image is:

$$I_2(i, j) = \begin{cases} 1, & \text{if } I_1(i, j) > \tau \\ 0 & \text{otherwise} \end{cases} \quad (\text{B.3})$$

for $i = 1, 2, \dots, n$ and $j = 1, 2, \dots, m$. We manually select τ so that the image preserves the supercavity regions, but not the background. After this step the image may contain blobs that do not belong to the supercavity.

5. Filling regions: a vertical segment of ones is added at the rightmost area of I_2 to guarantee a closed region of ones in which the bubble lies. The holes of the different blobs are then filled with ones. See filling algorithm in [33, p. 208]. With this step, the entire region of the bubble is filled with ones to obtain I_3 . Note that I_3 may have blobs that do not belong to the supercavity area.
6. Segmenting regions: By using a raster scan method [32, p. 318], the connected regions of image I_3 are labeled. The region of largest area is the supercavity. All other regions are removed from the image. After this step, we obtain an image I_4 which retains only pixels connected to the supercavity. I_4 may contain pixels that look like tails and do not belong to the supercavity area.

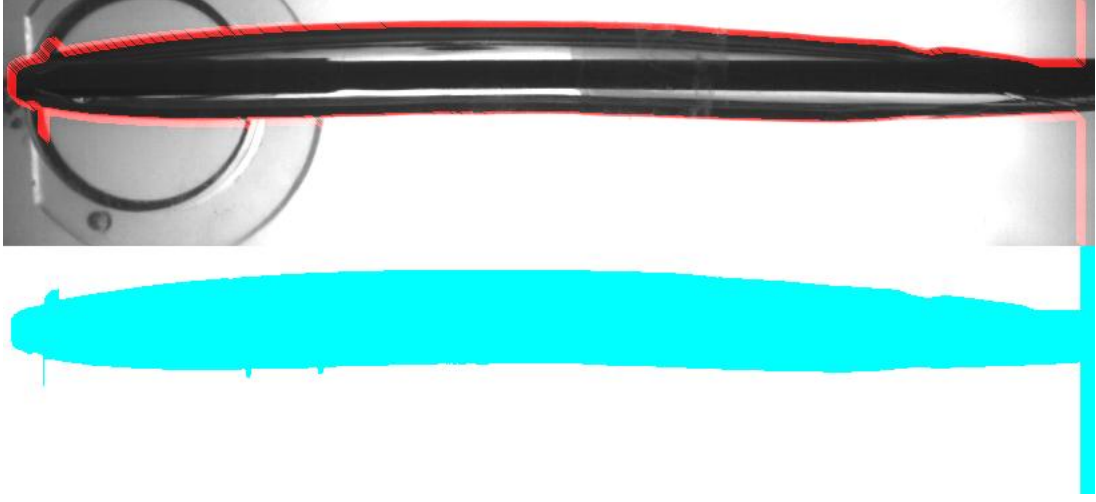


Figure B.1: Outcome of image segmentation algorithm. Experiment with forward facing model at the St. Anthony Falls Laboratory

7. Removing tails: The center of mass (\bar{i}, \bar{j}) of the supercavity region is computed. Then a horizontal line passed through (\bar{i}, \bar{j}) is used to remove tails. For all the columns along \bar{j} , the image is vertically scanned along j from $\bar{j} + 1$ to 1 and from \bar{j} to n . If a pixel is found to be 0, then the rest of the pixels in the vertical scan are labeled with zero as well. In this way, we obtain an image I_5 in which the supercavity region has no tails.

An outcome of the algorithm described above is illustrated in Figure B.1. The image in the figure corresponds to a small scale model for supercavitation research that we have at the St. Anthony Falls Laboratory.

B.3 Planing Computation

Given a binary image I_v with pixels equal to one where the vehicle body is located and the image I_5 in which the supercavity is segmented, an image with the planing region is:

$$I_{plan} = I_v - (I_5 \cap I_v) \quad (\text{B.4})$$

Image I_v is generated by setting ones in a rectangle that matches with the location of the vehicle body.